Journal of Applied Physics

A step-by-step guide to perform x-ray photoelectron spectroscopy

Cite as: J. Appl. Phys. **132**, 011101 (2022); https://doi.org/10.1063/5.0086359
Submitted: 25 January 2022 • Accepted: 08 June 2022 • Published Online: 01 July 2022

Grzegorz Greczynski and Lars Hultman

COLLECTIONS

This paper was selected as Featured

This paper was selected as Scilight

View Online Export Citation CrossMark

ARTICLES YOU MAY BE INTERESTED IN

Practical guide for curve fitting in x-ray photoelectron spectroscopy
Journal of Vacuum Science & Technology A **38**, 061203 (2020); https://doi.org/10.1116/6.0000377

Practical guides for x-ray photoelectron spectroscopy: Quantitative XPS
Journal of Vacuum Science & Technology A **38**, 041201 (2020); https://doi.org/10.1116/1.5141395

XPS guide: Charge neutralization and binding energy referencing for insulating samples
Journal of Vacuum Science & Technology A **38**, 031204 (2020); https://doi.org/10.1116/6.0000057

AIP Publishing

APL Quantum
CALL FOR APPLICANTS
Seeking Editor-in-Chief

© 2022 Author(s).

Journal of
Applied Physics

TUTORIAL

scitation.org/journal/jap

A step-by-step guide to perform x-ray photoelectron spectroscopy

Cite as: J. Appl. Phys. **132**, 011101 (2022); doi: 10.1063/5.0086359
Submitted: 25 January 2022 · Accepted: 8 June 2022 ·
Published Online: 1 July 2022 · Publisher error corrected: 6 June 2022

Grzegorz Greczynski[a)] and Lars Hultman

AFFILIATIONS

Thin Film Physics Division, Department of Physics, Chemistry, and Biology (IFM), Linköping University, SE-581 83 Linköping, Sweden

[a)] **Author to whom correspondence should be addressed:** grzegorz.greczynski@liu.se

ABSTRACT

There is a growing concern within the surface science community that the massive increase in the number of XPS articles over the last few decades is accompanied by a decrease in work quality including in many cases meaningless chemical bond assignment. Should this trend continue, it would have disastrous consequences for scientific research. While there are many factors responsible for this situation, the lack of insight of physical principles combined with seeming ease of XPS operation and insufficient training are certainly the major ones. To counter that, we offer a comprehensive tutorial written in the form of a step-by-step guide starting from experimental planning, through sample selection and handling, instrument setup, data acquisition, spectra analysis, and results presentation. Six application examples highlight the broad range of research questions that can be answered by XPS. The topic selection and the discussion level are intended to be accessible for novices yet challenging possible preconceptions of experienced practitioners. The analyses of thin film samples are chosen for model cases as this is from where the bulk of XPS reports presently emanate and also where the author's key expertise lies. At the same time, the majority of discussed topics is applicable to surface science in general and is, thus, of relevance for the analyses of any type of sample and material class. The tutorial contains ca. 160 original spectra and over 290 references for further reading. Particular attention is paid to the correct workflow, development of good research practices, and solid knowledge of factors that impact the quality and reliability of the obtained information. What matters in the end is that the conclusions from the analysis can be trusted. Our aspiration is that after reading this tutorial each practitioner will be able to perform error-free data analysis and draw meaningful insights from the rich well of XPS.

© 2022 Author(s). All article content, except where otherwise noted, is licensed under a Creative Commons Attribution (CC BY) license (http://creativecommons.org/licenses/by/4.0/). https://doi.org/10.1063/5.0086359

I. INTRODUCTION

It cannot go unnoticed for a reader of modern material science literature that x-ray photoelectron spectroscopy (XPS) has become the most common method for characterization of surface chemistry leaving far behind alternative techniques such as Auger electron spectroscopy (AES) or secondary-ion mass spectrometry (SIMS).[1] This is thanks to significant developments that took place in the last three decades of the twentieth century.[2] The number of papers in peer-reviewed journals where XPS was employed increased by a factor of 40 during last 40 years,[3] i.e., since the time when Kai Siegbahn was awarded the Noble Prize in Physics for his contributions to the development of the concerned analytical technique. This increase, enabled by tremendous developments on the instrumental side, is driven by an increasing importance of surface characterization in essentially all application areas. Dignitary applications of XPS are to determine chemical bonding and composition in the topmost few atomic layers of a material's surface and beneath by ion-etch depth profiling, thus resolving chemical shifts in complex compounds in their environment.

Unfortunately, this unprecedented increase in popularity of a technique is accompanied by a severe decay in the quality of XPS studies.[4,5] A recent literature survey revealed that about 30% of papers had major faults to the point that conclusions could be seriously questioned, while another 30% contained significant errors that could compromise the message of the paper.[5] This situation worsens the reproducibility crisis in science.[6] Moreover, due to the extreme popularity of XPS, its malpractice makes particularly severe damage to the research for the large risk of error propagation between studies. There are many factors that can be pointed out to be responsible for this *malum in se status quo*, a prime one being a massive growth in the number of XPS practitioners not followed by the corresponding increase in the quality training. Another is the apparent ease of operation generating plentiful of spectra, which can be published uncritically under the false premise that data are data.

Accompanying the proliferation of XPS applications is, however, a welcomed series of XPS guideline articles[7] from recent years written by experts who review essential aspects of XPS such as experiment planning,[8] sample handling,[9] instrument calibration,[10] charge referencing,[11] probing depth,[12,13] lateral resolution,[14] peak fitting,[15] quantitative analysis,[16,17] analysis of nanoparticles,[18] epitaxial films,[19] catalytic materials,[20] and polymers.[21] Whether these actions will result in a trend change for better practice in the field remains to be seen.

While it is understandable that not every scientist has the ambition or time to become an XPS expert, it is important to realize that it is not necessary to be one in order to perform error-free data analysis. With that approach in mind, we offer here a comprehensive tutorial written in a form of a step-by-step guide. The topic selection and the discussion depth are consciously adjusted for the entry-level XPS user; hence, some sections may appear oversimplified for experts. At the same time, we offer original spectra and XPS applications to titillate also the more fastidious colleague. Focus is put on the correct workflow, development of good practices, and solid knowledge of major factors that impact the quality and reliability of the obtained information. What matters in the end is that the conclusions can be trusted. For readers interested in more in-depth studies, we provide references to textbooks, review articles, and various guidelines.

This tutorial builds on the analysis of thin film samples deposited by PVD methods because this is where ample contemporary examples are found and where the authors have most experience. Hence, some aspects are specific to certain classes of materials. The fact that much film sample synthesis takes place under vacuum has important implications for the workflow as the air exposure time (between film growth and insertion into XPS spectrometer) becomes a decisive, yet often uncared for, factor in the final result. However, a majority of issues discussed here are of general nature and can be considered in the XPS analyses of most sample types.

Due to space limitations, many aspects of the XPS technique are not covered if they are not critical for the error-free analysis. The core part of this tutorial is divided into six sections. After covering the essential aspects of the technique (Sec. II), the presentation reflects the recommended workflow, that is, experiment planning (Sec. III), samples (Sec. IV), data acquisition (Sec. V), spectra analysis (Sec. VI), and result presentation (Sec. VII). Several application examples, selected with the aim to demonstrate versatility of the technique, are discussed in Sec. VIII. The tutorial ends with key pieces of advice (Sec. IX). Appended are an example XPS experimental protocol, an overview of common mistakes (Table I), a schematic representation of XPS workflow (Table II), and a glossary of basic XPS terms (Table III).

II. ESSENTIAL ASPECTS OF THE TECHNIQUE

The proper evaluation of XPS data requires at least a basic knowledge of the technique from underlying physics to technical realization. This statement has particular relevance in a market of fully automated spectrometers that limit human activity to sample loading, pressing the start button, and collecting spectra (sometimes machine-analyzed as they come out). However, the better the knowledge of the technique, the higher the chances of discovering potential problems, not to mention the fact that more advanced analysis plainly cannot be automated. Therefore, the essential aspects of XPS and related concepts are discussed in this section. As XPS users become more experienced, we should start considering prospects and challenges for future-day machine-learning and artificial intelligence; How to avoid rubbish XPS data corrupting the pristine?

Next, the XPS technique is presented, with key concepts highlighted in italics at first mentioning (see also Table III for glossary of basic XPS terms).

A. From photoemission to detection

XPS relies on the *photoelectric effect*, i.e., emission of electrons (sometimes called *photoelectrons*) from surfaces exposed to light of sufficiently high energy $h\nu$.[22] By measuring kinetic energy E_{kin} of electrons that leave the surface without inelastic collisions, one can obtain a precise estimate of their *binding energy* E_B (BE) through the use of the Einstein relation,[23]

$$E_B = h\nu - E_{\mathrm{kin}}. \tag{1}$$

The output from the experiment is an XPS *spectrum* (plural *spectra*), see examples in Fig. 6, i.e., the plot of collected electron flux as a function of the binding energy. Spectra typically feature one or more peaks that are due to the emission of electrons from atomic core levels (*core-level electrons*) and are, therefore, referred to as *core levels* (see Sec. II E). The probability that the interaction of an incoming photon results in photoelectron emission is described by the *photoionization cross section*.[24]

During experiments, samples are irradiated by x rays of known energy. The most common x-ray sources are Kα lines from Mg- and Al-coated electrodes (referred to as *anodes*, since they are at positive potential in the kV range to attract electrons) characterized by a photon energy of 1253.6 and 1486.6 eV, respectively. The selection of excitation source is crucial for several reasons. First, it directly sets the upper limit for the binding energy of electrons that can be detected. For example, with Al Kα anodes the practically useful binding energy range extends to ~1350 eV (limited by the presence of inelastically scattered electrons that give rise to background that increases sharply once E_B approaches $h\nu$). If that range is not sufficient, one can consider more exotic x-ray sources such as Ag Lα ($h\nu = 2984.3$ eV), Cr Kα ($h\nu = 5414.7$ eV), or even Ga Kα ($h\nu = 9251.7$ eV). Second, the natural x-ray spectrum produced when high-energy electrons interact with the anode material is not *monochromatic*, but rather consists of a number of sharp peaks (so-called *characteristic lines* associated with the electronic structure of atoms in the anode material) superimposed onto a continuous background (*Bremsstrahlung* radiation created as electrons are decelerated in the anode). Furthermore, the characteristic lines often have complex structure. For example, the Kα lines of an Al anode are in fact Kα$_1$–Kα$_2$ doublets with the 2:1 intensity ratio that

© Author(s) 2022

appear at 1486.70 and 1486.27 eV, respectively. While the natural line width of each component is 0.5 eV, the resulting composite line width is approximately 0.85 eV, which has a detrimental effect on the *energy resolution*. In addition to $K\alpha_1$–$K\alpha_2$ doublet, weaker lines ($K\alpha_3$ through $K\alpha_6$, as well as Kβ) are also present at 8–70 eV higher energy.[25,26] Thus, working with unfiltered Kα radiation implies several disadvantages such as poor energy resolution, the presence of *satellite peaks* (due to photoelectrons excited with $K\alpha_3$–$K\alpha_6$ and Kβ lines), and lowered *signal-to-noise* ratio (due to high background level caused by electrons excited by Bremsstrahlung radiation). For these reasons, one should prioritize the use of *monochromatic sources* that were developed in 1970s[27] and nowadays offer an energy spread of the incident radiation as low as 0.26 eV. Finally, the source selection determines the *probing depth* (see Sec. II F). In the relevant energy range, the inelastic electron mean free path increases with increasing electron energy, hence higher energy sources enable even those electrons that are excited at larger depths to reach the surface without collisions. Larger probing depth can be beneficial to minimize the relative contribution from surface oxides/contaminants, especially for those samples that are sensitive to *sputter damage*, which excludes the use of (otherwise common) Ar^+ etching before analyses (cf. Sec. III C). Such benefits come, however, at the price of worse energy resolution due to broader line widths of Ag Lα and Cr Kα sources.

Dual anodes are sometimes used to extend the instrument flexibility, in which case the anode face is coated with two different materials (e.g., Al and Mg, or Al and Ag) and source design allows to easily switch between x rays of different excitation energy.[28,29] In specific cases such as Al/Ag anodes, the additional benefit is that the energy of the Ag Lα photons is twice that of Al Kα photons, hence both sources can be monochromatized with a dual anode monochromator.

Two design concepts are used in modern instruments for the sample irradiation by x rays. The first one relies on the x-ray beam focused into a small spot (a few μm in diameter) which is rastered over the sample area to be analyzed (or alternatively allows for spatially resolved analyses). However, the necessity of focusing x rays has a negative impact on their dispersion and, hence, the energy resolution is compromised. The second design employs a relatively broad beam of 1–2 mm (at the sample plane) such that the sample is essentially flooded with x rays and the area to be analyzed is often defined by the entrance slit in the aperture of the *electron energy analyzer*.

In the above cases, emitted electrons that leave the surface into the vacuum enter the analyzer slit of the spectrometer. The parameter important for common types of analyses (for example, angle-resolved XPS) is the *acceptance angle* γ, which describes the angular spread of photoelectrons that are allowed to enter the analyzer.[29] Typically, the lower the acceptance angle, the better the angle-resolving power of the instrument. However, in some designs, angle-resolved XPS is possible even with acceptance angles as large as 85° (e.g., Theta probe instrument from Thermo Fisher Scientific), in which case the position-sensitive detector is used to count electrons emitted at different emission angles. The key element of the instrument is the energy analyzer. Nowadays, the most commonly used analyzer type is the electrostatic hemispherical analyzer consisting of two concentric hemispheres (see Fig. 1).

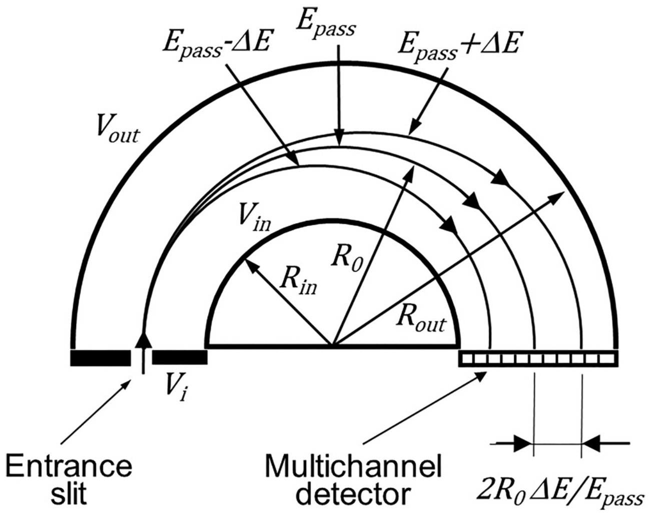

FIG. 1. Schematic cross-sectional view of a hemispherical electron energy analyzer.

Electrons are typically retarded in the lens column before entering the hemispherical analyzer so that the electron initial energy E_0 is reduced to E_{pass}. The latter is commonly called the pass energy as it refers to the energy of the electron traveling through the analyzer along the equipotential plane defined by $R_0 = (R_{\text{in}} + R_{\text{out}})/2$, in which R_{in} and R_{out} denote the inner and the outer hemisphere radii, respectively. The voltages on the outer and inner hemispheres, V_{out} and V_{in}, are then linked to R_{in}, R_{out}, and E_{pass} through the relationship[30]

$$e(V_{\text{out}} - V_{\text{in}}) = E_{\text{pass}}\left(\frac{R_{\text{out}}}{R_{\text{in}}} - \frac{R_{\text{in}}}{R_{\text{out}}}\right). \tag{2}$$

Electrons entering with energies higher (lower) than E_{pass}, $E_{\text{pass}} + \Delta E$, and $E_{\text{pass}} - \Delta E$, respectively, hit the detector plane closer to the outer (inner) hemisphere, where they are collected at different sections of the *multichannel* detector, which allows for the reconstruction of the intensity vs energy profile. To record a spectrum over the energy range specified by the user, retarding lens voltages, V_{in}, and V_{out} are scanned[29] so that Eq. (2) is satisfied at all times, while E_{pass} is kept constant to ensure that the energy resolution is the same across the entire energy spectrum.

The pass energy, which determines the absolute energy resolution, is selected by the user, noting that the lower the E_{pass}, the better the energy resolution. That is because the term $\Delta E/E_{\text{pass}}$ is constant (for a given analyzer geometry), hence $2\Delta E$, i.e., the energy difference between the fastest and the slowest electrons that can be simultaneously detected at a multichannel detector, is directly proportional to the pass energy. Thus, lowering E_{pass} results in lower $2\Delta E$ and the minimum energy difference between two electrons that are detected in two separate detector channels (i.e., resolved by the instrument) decreases.

© Author(s) 2022

One should bear in mind, though, that lower pass energy means lower current through the analyzer, hence, in practice the E_{pass} selection is a compromise between acceptable energy resolution and the available measurement time. This is illustrated in Fig. 2 for the case of Ag $3d_{5/2}$ peak recorded with different pass energies from the sputter etched Ag foil. It is seen that the gain in the energy resolution decreases as E_{pass} is getting smaller and eventually further decrease in pass energy results in marginal improvement that comes on the expense of a severe loss of the signal-to-noise ratio (cf. Sec. V H).

B. The concept of binding energy

The term *binding energy* is frequently used in XPS analyses and, therefore, it is very important to elaborate on its connotations. First, it is emphasized that in the ground state of an atom, electrons do not possess any distinct energies that could be exclusively assigned to them to be considered their binding energy.[31] Instead, the total energy of the system is simultaneously shared between all its components. Consequently, it is not correct to view the specific peak positions obtained from XPS analyses as a direct measure of individual energy (binding energy) associated with electrons occupying a given core level. One should rather treat the measured energy values E_B (estimated from peak positions) as the difference between the total energy of a positive ion E_+^* after the photoionization event has taken place (by emitting an electron from the core level under consideration) and the total energy of an atom in the ground state E_0, i.e.,

$$E_B = E_+^* - E_0. \tag{3}$$

The law of energy conservation requires that the total energy before and after the photoionization is conserved,

$$h\nu + E_0 = E_+^* + E_{\text{kin}}. \tag{4}$$

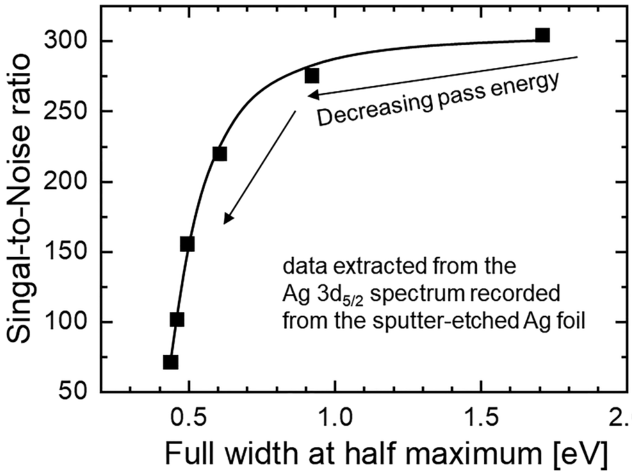

FIG. 2. Signal-to-noise ratio plotted as a function of peaks' full-width-at-half-maximum for the case of Ag $3d_{5/2}$ peak from the sputter etched Ag foil recorded with different pass energy values.

Combining Eqs. (3) and (4) results in Eq. (1). Thus, the XPS spectrum of an atom featuring several core-level peaks is properly viewed as a map of the *final states*, i.e., energy differences between one ground state (characterized by E_0) and the numerous final states (described by several E_+^* values, one for each core-level state).

C. Chemical shifts

The essential strength of XPS in modern materials science is its ability to provide information about the chemical bonding. In the early days of the technique, XPS was sometimes—and in some communities still is—referred to as electron spectroscopy for chemical analysis (ESCA).[32] It has been realized already back in the 1950s that the changes in the valence electron configuration resulting from the formation of chemical bonds have a direct and measurable effect on the position of core-level peaks assigned to the concerned atoms.[33–35] The higher the negative charge density on an atom, the higher the kinetic energy of photoelectrons that originate from its core levels and the lower the binding energy of corresponding peaks in the spectrum. The phenomenon of peak shift caused by the change in chemical environment is referred to as *chemical shift*.[32,36]

The complete understanding of the origin of chemical shift is crucial. Perhaps the best illustration of the phenomenon is the case of the "ESCA molecule,"[37] i.e., ethyl trifluoroacetate, shown in Fig. 3(a). The ESCA molecule consists of four carbon atoms in distinctly different bonding configurations, with the valence charge density on C atom being the highest for the CH_3 unit and gradually decreasing over the C—O, O—C═O, and the C—F_3 units. The corresponding C 1s spectrum[38] features four well-resolved and equally intense peaks, which leads to the essential question—how come the core-level electrons that are not involved in bond formation are affected? A rather common misinterpretation is that differences in the valence-charge density have a direct effect on the binding energy of core-level electrons. However, as discussed in Sec. II B, strictly speaking electrons bound in an atom do not have distinct energies, but rather share simultaneously the total energy of the whole system. Therefore, the chemical shifts should rather be discussed in terms of the total energy before and after the photoionization event. Referring to the case shown in Fig. 3(a), one may say that it costs more energy to create a *core hole* localized on the C atom in CF_3 than on that in the CH_3 unit. The physical reason for that is the negative valence charge density is relatively low on C atoms in the former configuration due to the high ability of F atoms to attract shared electrons while forming chemical bonds (the property referred to as *electronegativity*),[39] which results in poorer *screening* of the core hole left after photoionization.[40] As a consequence, a photoelectron leaving this site experiences stronger Coulomb attraction and arrives at the detector with lower kinetic energy than corresponding electrons originating from a C atom in the CH_3 unit. This phenomenon gives rise to the apparent split of more than 8 eV between C 1s signal from the two sites. The same mechanism leads to that the carbon atom bonded to two oxygen atoms [cf. O—C═O unit in Fig. 3(a)] gives rise to peak shift of ca. 4.8 eV from the CH_3 position. Here, the shift is smaller than for the case of C in CF_3 (indicative of a higher valence charge density on carbon atoms in O—C═O) as (1) O electronegativity is lower than that of F (in the Pauling scale: 3.44 vs 3.98, respectively),[41]

© Author(s) 2022

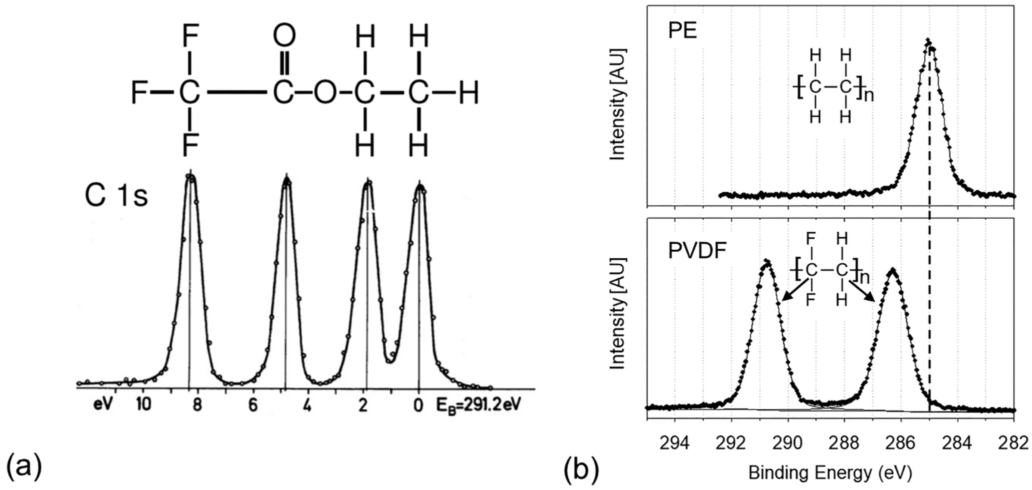

FIG. 3. (a) (Top) Chemical structure of ethyl trifluoroacetate molecule and (bottom) corresponding C 1s core-level spectrum. [Reproduced with permission from Gelius *et al.*, J. Electron Spectrosc. Relat. Phenom. **2**, 405 (1973). Copyright 1973 Elsevier.] The energy scale is referenced to the C 1s peak of C—C/C—H carbons (detected at 291.2 eV with respect to the vacuum level). [Reproduced with permission from Greczynski and Hultman, Prog. Mater. Sci. **107**, 100591 (2020). Copyright 2020 Elsevier.] (b) C 1s spectra of (top) polyethylene and (bottom) polyvinylidene fluoride.

and (2) there are only two electronegative elements bonding to C (as compared to three for CF_3 carbon). The valence charge density further increases on the C atom that makes only one single bond to oxygen, which results in that the peak shift in this case is only 2 eV.

Elements with high electronegativity such as O or F can give rise to nearest-neighbor effects (*secondary chemical shifts*), where binding energy shifts appear even for atoms that do not make direct bonds to O or F, but are bonded to atoms that do. One illustration of this phenomenon is shown in Fig. 3(b). The top panel shows the C 1s spectrum recorded from polyethylene (PE), which consists of chains of chemically identical sp^3-bonded C atoms giving rise to the single C 1s peak centered at 285.0 eV. In the bottom panel, the C 1s spectrum of polyvinylidene fluoride (PVDF) is displayed. In this case, every second C bonds to two F atoms (CF_2) and the corresponding peak appears at 290.8 eV, i.e., shifted by 5.8 eV with respect to the PE carbon peak. While the latter effect is fully understandable from the discussion around Fig. 3(a), it may come as a surprise that even the second peak in the PVDF C 1s spectrum due to C atoms that are bonded to hydrogens (CH_2) is shifted with respect to the C 1s signal from PE by 1.3 eV. Clearly, significantly lowered valence charge density on C atoms in CF_2 units of PVDF results in that even the valence charge density on neighboring C atoms from CH_2 units is affected. The latter shift is called secondary chemical shift. As illustrated in Fig. 3(b), such shifts are typically smaller in magnitude than the primary shifts (here, 5.8 vs 1.3 eV), so should not be neglected.[42]

D. Energy reference levels

The basic equation of XPS [Eq. (1)] can be directly applied only for analyses performed in the gas phase. In that case, the photoelectron kinetic energy does not change on the way to the detector, hence *vacuum level* (VL), corresponding to the energy of a free electron at rest and semi-infinitely distant from the considered system, serves as a natural reference level ("0 eV" on the binding energy scale).[43,44] The situation is distinctly different for solid-phase samples due to the fact that the emitted photoelectrons have to overcome the potential barrier at the surface, the so-called *work function* ϕ_{SA}, which corresponds to the energy difference between the *Fermi level* (FL) and the VL. In such cases, the FL, which according to the Fermi–Dirac equation denotes the energy at which above absolute zero, the probability of finding an electron is ½, provides a more rational and convenient reference level. The electron binding energy is then denoted as E_B^F (with $E_B^F = 0$ eV corresponding to electrons originating from the FL). To explain why this is the case, we refer to the energy level diagram shown in Fig. 4. It is assumed here that the sample and spectrometer are in good electrical contact, which means that (i) there are enough free charge carriers available on both sides of the contact and (ii) the charges can freely move across the interface to establish a common FL (see also Secs. V A and V B). The direction of the negative charge transfer depends on the relation between the sample and the spectrometer work functions, ϕ_{SA} and ϕ_{SP}, respectively. Charge flows from sample to spectrometer if $\phi_{SP} > \phi_{SA}$, or from spectrometer to sample in the case of $\phi_{SA} > \phi_{SP}$. Hence, the resulting contact potential difference V_C has to be accounted for while considering an electron traveling toward the entrance slit of the energy analyzer, with the kinetic energy E_{kin}^{SA} being either reduced ($\phi_{SP} > \phi_{SA}$) or increased ($\phi_{SA} > \phi_{SP}$), to E_{kin}^{SP} which is measured at the detector side.

It follows from the energy level diagram in Fig. 4 that the kinetic energy of a photoelectron after leaving the sample E_{kin}^{SA} is

$$E_{\text{kin}}^{SA} = h\nu - E_B^F - \phi_{SA}. \tag{5}$$

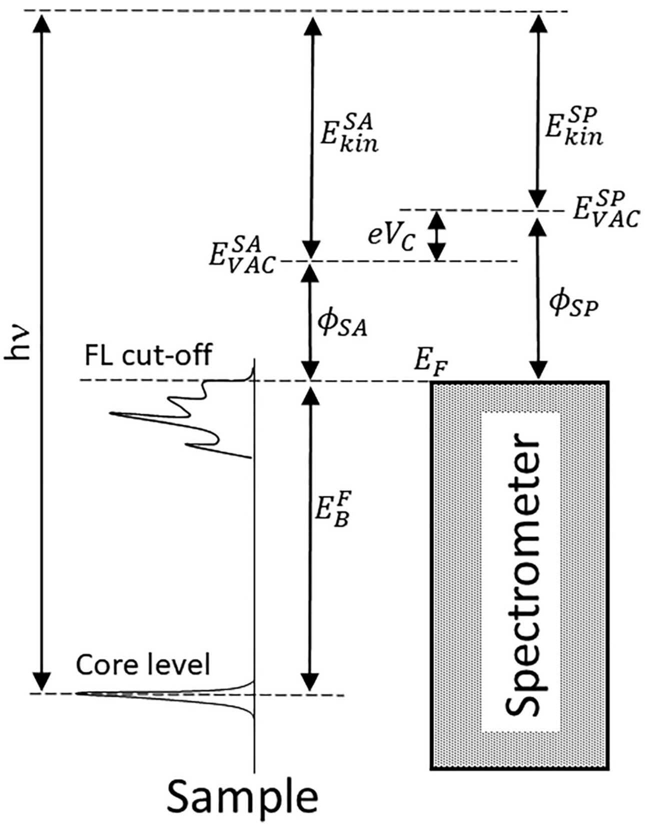

FIG. 4. Energy level diagram for a sample in good electrical contact to the spectrometer. [Reproduced with permission from Greczynski and Hultman, Prog. Mater. Sci. **107**, 100591 (2020). Copyright 2020 Elsevier.]

Since

$$E_{\mathrm{kin}}^{SA} + \phi_{SA} = E_{\mathrm{kin}}^{SP} + \phi_{SP}, \tag{6}$$

we can rewrite Eq. (5) as

$$E_B^F = h\nu - E_{\mathrm{kin}}^{SP} - \phi_{SP}, \tag{7}$$

which is independent of the sample work function. Since the spectrometer work function is constant (typically established during the calibration procedure), photoelectrons originating from a given core level always appear at the detector with the same kinetic energy, irrespective of what the sample work function is. It is important to realize that while any change in ϕ_{SA} does not affect the position of core-level XPS peaks with respect to the Fermi level E_B^F, their positions are shifted with respect to the VL.

E. Types of peaks

The change in the number of electrons arriving at the detector as a function of their kinetic energy carries essential information about the sample. Conventionally plotted as a function of binding energy, XPS spectra typically consist of numerous, often overlapping, peaks varying in shape and intensity, that if not fully resolved, are described as *shoulders*, *humps*, or *satellites*.[40] The reason for this plethora of spectral features is that numerous physical phenomena take place in the analyzed sample either before or after the photoionization. Often in the XPS literature, one speaks about *initial* and *final state effects*, respectively.

The vast majority of XPS peaks is due to electrons that originate from specific core levels and did not suffer energy losses on the way to the surface. They are described using a *spectroscopic notation* of the form "X nl_j," where X stands for the element, n is the principal quantum number ($n = 1, 2, 3, \ldots$), while l accounts for the orbital angular momentum quantum number denoted as s, p, d, f corresponding to $l = 0, 1, 2, \ldots, n - 1$. j in "X nl_j" is the total angular momentum quantum number and is equal to the sum of the orbital angular momentum and the spin projection ($s = \pm 1/2$) quantum numbers $j = l + s$. For example, Ti $2p_{3/2}$ corresponds to electrons from Ti atoms with $n = 2$, $l = 1$, and $s = 1/2$. For the correct XPS data analysis, it is essential to understand that core-level signals with $l \geq 1$ occur as spin–split doublets: $p_{3/2}$–$p_{1/2}$, $d_{5/2}$–$d_{3/2}$, and $f_{7/2}$–$f_{5/2}$. Neglecting this point is one of the most frequent mistakes in what becomes erroneous XPS analyses.[5] The reason for the splitting is *spin–orbit* or *j–j* coupling, where the kinetic energy of detected photoelectron depends on whether the unpaired electron left after photoionization has its spin vector parallel ($j = l + 1/2$) or anti-parallel ($j = l - 1/2$) to the orbital angular momentum vector. The BE splitting between spin–split components varies from tenths of eV to several eV. In general, the splitting increases with atomic number for a given subshell (constant n, l) and decreases as l increases for a given shell (n constant). The area ratios between spin–split peaks are determined by the degeneracy of each electronic level $(2j + 1)$ and, hence, are equal to 2:1 for $p_{3/2}$ and $p_{1/2}$ levels, 3:2 for $d_{5/2}$ and $d_{3/2}$ levels, and 4:3 for $f_{7/2}$ and $f_{5/2}$ levels. Importantly, both the area ratio and the energy splitting are not constant for a given element and show some variation with, e.g., chemical environment [cf. Ta 4f peaks in Fig. 6(b) and Zr 3d peaks in Fig. 13]. In some cases, the spin-splitting can be of the order of instrument resolution (e.g., 0.4 eV for Al $2p_{3/2}$ and Al $2p_{1/2}$), which may result in that the corresponding signal appears as one peak with a shoulder to the higher BE side. To the other extreme, spin-splitting can be so large that the detailed analysis tends to focus only on the stronger of the two components (e.g., Cu $2p_{3/2}$, which appears 19.8 eV away from the Cu $2p_{1/2}$ peak).

For a given type of core-level signal, the associated binding energy increases with increasing atomic number Z as illustrated in Fig. 5. This is because the increasing number of protons in the nuclei implies tighter binding of core-level electrons. For example, in the case of 1s levels, the peak position varies from 189.4 eV for B (Z = 5) to 284.5, 398.1, 531.0, 684.9, 863.1, 1071.8, and 1303 eV for C, N, O, F, Ne, Na, and Mg (Z = 12). The next in line Al 1s signal is at 1559.6 eV, which is too high binding energy to be accessed with the most common x-ray sources such as Al Kα or Mg Kα [cf. Eq. (1)]. Because of that, the primary core-level signal for Al is the 2p level (at 72.9 eV), which also marks the start of the 2p series that ends with the As $2p_{3/2}$ peak at 1324.0 eV (Z = 33).

© Author(s) 2022

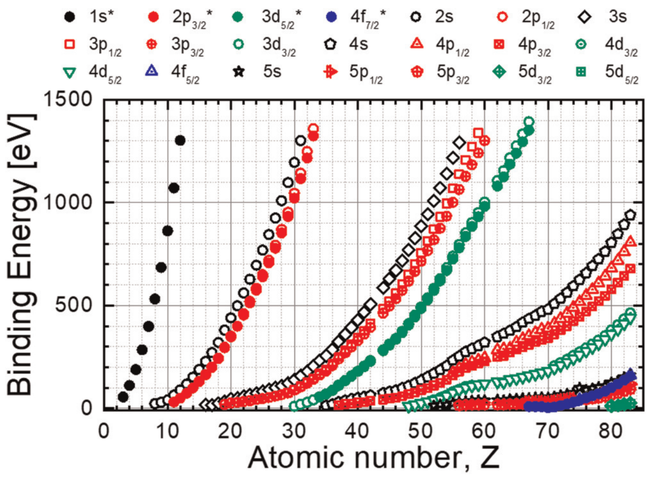

FIG. 5. Variation in core-level binding energies as a function of atomic number Z.

The same concept applies also to the 3d series that begins with the Se $3d_{5/2}$ peak at 55.6 eV (Z = 34) and, in principle, continues through Ho (Z = 67). However, for lanthanides starting from samarium (Z = 62) the 3d core-level spectra become very complex. To avoid further analysis challenges, the 4d level may be a better alternative. The situation improves significantly in that respect once the 4f core levels become available, which is the case from lutetium (Z = 71) with Lu $4f_{7/2}$ at 7.3 eV (probably the lowest BE core level in the entire periodic table). The 4f series with its well-defined sharp peaks is heavily exploited in the core-level spectroscopy of all heavier elements ($71 \leq Z \leq 83$), after which spectra become again more and more complex essentially for all actinides. Thus, plots shown in Fig. 5 reflect a rather fortunate fact: with commonly used excitation sources, the photon energy is high enough to ensure that a useful core-level signal is available for the vast majority of elements (with exception for rare earths).

For elements where the binding energy of their strongest lines is significantly higher than ∼1100–1200 eV, weaker signals from the "next in line" series appearing at much lower BE may present a better alternative to be recorded and analyzed. This is particularly the case if the quantitative elemental analysis of multicomponent samples is performed (see Sec. VI D), in which case it becomes critical to ensure that the probing depth, which decreases with increasing BE, is similar (cf. Sec. II F and Fig. 7). For example, when Mg—Al alloys are analyzed, a better alternative to the Mg 1s peak at 1303 eV is the Mg 2p signal at 49.8 eV, which is very close to the Al 2p core level.

There are numerous resources available, in the form of reference handbooks[45–49] and websites,[50–54] that provide reference XPS spectra for a vast majority of elements. These are extremely helpful not only for novice users, and it is recommended to prioritize them over the automatic peak identification features typically available on modern instruments. The latter can only provide rough ideas about peak origin, so the risk of misinterpretation is high especially if large chemical shifts (see Sec. II C) are involved. In either case, for the entire peak identification process to be meaningful, the spectra need to be acquired on a correctly calibrated instrument (see Sec. V A) and the proper charge referencing must be performed (see Sec. V B).

Examples of the most common peak types are given in Fig. 6. Figure 6(a) displays the high energy resolution spectrum recorded from a sputter-etched MoN thin film surface over the binding energy range 420–385 eV, which is where typically the N 1s signal appears. As the primary core-level peaks of Mo (Mo 3d) appear well outside this energy range, it may come as a surprise to the novice user (it did to the authors at the time) that instead of a single N 1s peak at 397.9 eV no less than three peaks appear in the specified energy range. The additional peaks are due to spin–split Mo 3p levels: $3p_{3/2}$ at 394.4 eV and $3p_{1/2}$ at 411.9 eV. This case exemplifies a prevalent issue namely that the primary signal of one element may overlap with secondary peak(s) of the other element from the same sample. The risk for such problems obviously increases with an increasing number of elements in a sample, which is quite a common trend in today's materials

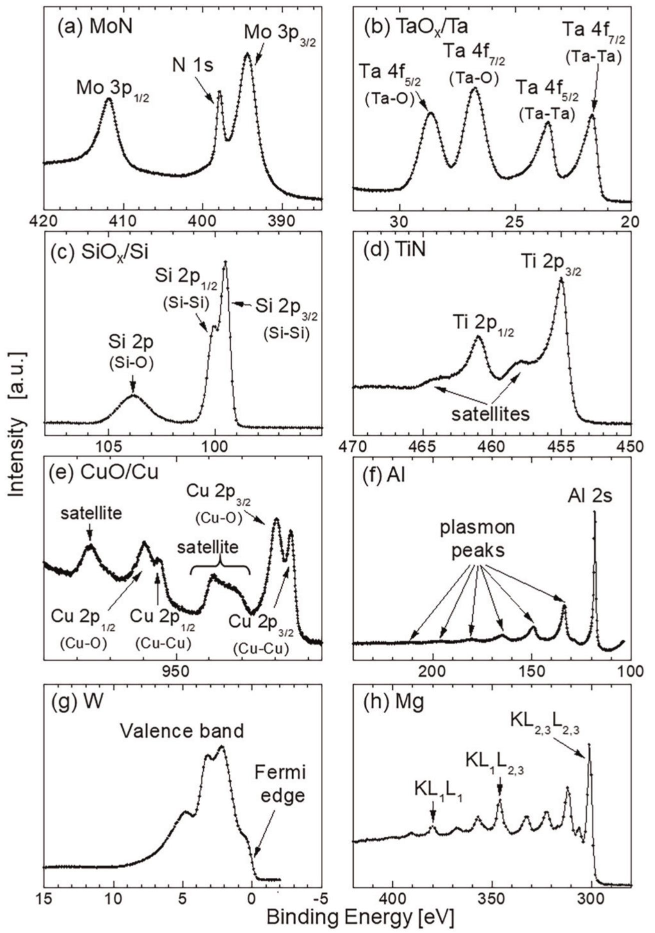

FIG. 6. Examples of features typically accounted in XPS spectra.

science with increasing sample compositional complexity. Often, the dispersion of peaks with overlap in the recorded spectra is not so obvious, especially if the concentrations of elements are very different. It is, therefore, essential for a correct analysis to check the positions of all peaks for each element present in the sample of interest. One very useful condition that helps resolve problems related to peak overlap is the predefined interrelation between spin–split peaks. In the case of Mo 3p peaks in Fig. 6(a) by imposing constraints on the area ratio between $3p_{3/2}$–$3p_{1/2}$ components, one can obtain more precise estimate for the area under N 1s peak and, hence, perform reliable elemental quantification.

Another aspect illustrated in Fig. 6(a) is that the peak shape and width (often measured by *full-width-at-half-maximum*, or FWHM) varies greatly depending on the element. In this case, N 1s peak is symmetric and relatively narrow (FWHM of ~0.9 eV), while both Mo 3p peaks are considerably broader (FWHM of ~2.7 eV) and characterized by significant asymmetry to the high BE side.

There are four main factors that affect the width of core-level peaks in XPS,[55]

(1) the natural width of the core-hole state ΔE_N determined by the uncertainty principle (sometimes referred to as *lifetime broadening*) $\Delta E_N = h/\tau = 4.1 \times 10^{-15}/\tau$ [eV], in which τ is the core-hole life time,[56]
(2) broadening from local atomic arrangements that affect the screening of the core-hole state ΔE_S,
(3) dispersion of the photon source ΔE_P (down to ~0.26 eV for monochromatized Al Kα radiation, see Sec. II A), and
(4) resolving power of the analyzer (see Sec. II A), ΔE_A, which is <0.1 eV under optimized conditions of low pass energy (see Sec. V D) and no charging (see Sec. II G).

Two first factors are obviously sample-specific, while the latter depend on the instrument and describe its energy resolution (see Sec. V D). The resulting peak's FWHM is then given by $\sqrt{\Delta E_N^2 + \Delta E_S^2 + \Delta E_P^2 + \Delta E_A^2}$.

The asymmetry on the high BE side often observed is the case of core-level lines originating from metallic samples [such as Mo 3p peaks shown in Fig. 6(a)] is linked to events that may accompany the photoemission of core electrons. These include excitations of *valence electrons* (i.e., electrons that participate in the bonding formation and give rise to the *valence band*, VB, at the lowest BE range) from the Fermi level to the higher-lying states. In such cases, the extra energy cost is deducted from the kinetic energy of the photoelectron that leaves the sample. In consequence, such electrons appear at higher BE with respect to all electrons excited from the same core level and detected without additional energy loses. Since the probability for such excitations within the valence band decreases with increasing required energy, the effect shows up as an asymmetrical tail. Naturally, the degree of asymmetry increases with increasing *density of states* (DOS) at the Fermi level.[57]

It is very important to realize that peak shapes may strongly depend on the chemical surrounding. For example, core-level peaks of transition metals are often asymmetric for metallic samples and become symmetric for their oxides. This aspect is illustrated in Fig. 6(b) in which the Ta 4f spectrum from a Ta film with a *native oxide* (i.e., oxide that forms naturally as a result of ambient air exposure with no other treatments) is shown. There are four peaks in the spectrum indicative of that Ta atoms are present in two chemical states (cf. Sec. II C), each represented by a pair of spin–split $4f_{7/2}$–$4f_{5/2}$ peaks. Peaks at lower BE, 21.7 and 23.6 eV, are due to metallic Ta, and possess pronounced asymmetrical tails to the high BE side. The corresponding pair of peaks due to Ta atoms bonded to O (Ta-O), at 26.7 and 28.6 eV, is shifted to the high BE with respect to metal peaks as the valence charge density on those atoms is considerably lower due to bonding with the high electronegativity element such as oxygen (cf. Sec. II C). Oxide peaks are symmetric as obviously in this case there is no DOS at the FL that could account for extra energy losses.

Figure 6(c) offers another example of core-level spectra with chemically shifted components recorded from Si film with native oxide. In this case, the Si $2p_{3/2}$ and Si $2p_{1/2}$ peaks corresponding to Si—Si bonding are at 99.5 and 100.1 eV, i.e., only 0.6 eV apart. Thus, *peak fitting* (see Sec. VI C) is necessary to obtain correct BE values. The broad peak centered at 103.8 eV is the Si 2p signal that originates from the surface oxide layer, hence from Si atoms bonded to O. In this case, the spin–split components cannot be resolved, which illustrates that the chemical environment has a profound effect not only on the peak shape, but even on the number of peaks that is generated for the same type of core-level electrons.

In addition to main peaks, satellite features may also appear on the high BE side of primary peaks. This is the case for Ti 2p spectrum recorded from an *in situ* XPS sputter-etched TiN thin film shown in Fig. 6(d), where apart from the $2p_{3/2}$–$2p_{1/2}$ doublet at 455.0 and 461.0 eV, pronounced shoulders shifted by ~3 eV to high BE are observed. It should be emphasized that those satellite features have nothing in common with satellite peaks that appear due to the use of non-monochromatic sources (cf. Sec. II A). Possible explanations for their origin include the so-called *shake-up* events (the transitions in the valence band region that take place on the expense of the kinetic energy of ejected Ti 2p electrons)[58,59] or the variations in the screening probability of the core-hole state by Ti 3d electrons (leading to poorly screened peaks at high BE and well-screened peaks at lower BE).[60–64] Similar shoulders are also observed in other transition metal nitrides,[65] and their intensity strongly depends on the energy and incidence angle of Ar^+ ions used to sputter-etch the surface prior to XPS analyses.[66] They are sometimes confused with oxide peaks, especially if significant amounts of O are present at the surface. However, studies of single-crystal TiN/MgO(001) films grown and analyzed *in situ* confirm the intrinsic origin of such satellite peaks.[67]

While discussing *shake-up* peaks, we should also consider *shake-off* phenomena. Both events are related to the excitations of the valence band electrons that are triggered by the emission of photoelectrons from inner atomic shells and creation of a core-hole state. The difference is that shake-up peaks arise due to transitions to discrete non-occupied states while the term shake-off describes transitions of valence electrons to a continuum of states.[68] In both cases, the extra energy required for the transition is deducted from the kinetic energy of the photoelectron that leaves the sample, hence shake-up and shake-off features appear on the high BE side

© Author(s) 2022

of the primary peaks. The discrete nature of shake-up transitions implies that they are manifested as peaks, while continuous nature of shake-off events means that they contribute to the increase in the inelastic background.

A next level of complexity is illustrated by the Cu 2p spectrum of the Cu film with the top CuO layer shown in Fig. 6(e). In this case, the entire Cu 2p envelope consists of two, partially overlapping, $2p_{3/2}$–$2p_{1/2}$ doublets from Cu–Cu (932.7 and 952.5 eV) and Cu–O (934.8 and 954.8 eV) bonds, as well as, of pronounced shake-up structures (939–946 and 959–966 eV). Worth noticing is also a strong increase in the background (from low to high BE), which is caused by Cu 2p electrons that undergo *inelastic scattering* on their way to the surface.

Energy losses associated with photoionization can be manifested in more spectacular way than just shake-up structures. One example is shown in Fig. 6(f) for the case of sputter-etched Al thin film samples. Apart from the Al 2s core-level peak at 117.9 eV, multiple smaller peaks appear to the high BE side with an amplitude that decreases with increasing energy distance from the main line. Another characteristic feature is the constant energy spacing between certain peaks. Such structures arise due to discrete energy losses experienced by photoelectrons leaving the sample and are called *plasmons*. They are most common for clean metal surfaces, in which case certain probability exists for an ejected electron to excite collective oscillations of conduction band electrons. The frequency of these oscillations can be calculated from the energy splitting between the plasmon peaks. The amplitude of plasmon peaks decreases with increasing energy difference from the main line since the probability for the excitation of higher order modes goes down.

Density of electronic states in the lowest BE region—the valence band range—can also be readily studied by XPS. In contrast to core-level electrons, VB electrons participate in the formation of chemical bonds. Example of the VB spectrum recorded from a sputter-etched W surface is shown in Fig. 6(g). Noteworthy is the presence of abrupt drop in the density of states at the Fermi level (i.e., 0 eV for the well-calibrated instrument), the so-called *Fermi edge*, FE, which is very useful for proper referencing of the BE scale (cf. Sec. V B).

In the last example of Fig. 6(h), we are concerned with the presence of Auger peaks that commonly appear in XPS spectra. When the core hole left after photoionization is filled by the valence electron the energy can be released either in the process of x-ray fluorescence (not detectable by XPS) or by emission of another electron (Auger emission). As the kinetic energy of Auger electrons is independent of the excitation source energy, the position of these peaks on the BE axis depends on the excitation source. Auger peaks are typically broader than XPS peaks, but in some cases, like that of Mg shown in Fig. 6(h), they might be mixed up with photoelectron peaks. Notations like $KL_1L_{2,3}$ means that the first electron (photoelectron) ejected from the atom originated from a K orbital, while the electron that filled the core hole and the released Auger electron came from L_1 and $L_{2,3}$ orbitals, respectively.

Apart from the examples shown in Fig. 6, one should be aware of several other, less common, peak types. One is the *multiplet splitting* (or the *exchange splitting*),[40,69] which may occur if there are unpaired electrons in the valence levels that interact (exchange interaction) with the unpaired electron left in the core level after photoionization. Thus, even "s" peaks (i.e., with $l = 0$) can split (e.g., Mn 3s). While using non-monochromatic sources, the satellite peaks appear in the spectrum (on the low BE side of main peaks) due to the presence of weaker x-ray lines in the exciting radiation (see Sec. II A). Those are relatively easy to identify as the energy shift from the main peak and relative intensity are well defined. Not using a *monochromator* that filters out the undesired radiation may also result in the presence of *ghost peaks* that appear due to the presence of x-ray radiation other than that from the original anode material. Common examples are impurities in the anode material (e.g., Mg in Al anodes), oxidized anode, and Cu Lα radiation from the anode base due to a damaged or old anode. The extra peaks in all those mentioned cases can be easily identified as they are displaced by a characteristic energy interval given by the energy difference between the original and the contaminating radiation.

F. Surface sensitivity

A very important merit of XPS is its surface sensitivity, which has several implications for sample handling (see Sec. IV E), experiment planning (Sec. II C), as well as for data acquisition (Sec. V E) and the interpretation of results (Sec. VI D). The surface sensitivity effect has two reasons. First, within the kinetic energy range characteristic for core-level spectroscopy conducted with the most common x-ray sources such as Mg Kα or Al Kα ($300 \lesssim E_{\mathrm{kin}} \lesssim 1400$ eV), the interaction of photoelectrons with the surrounding matter is predominantly through *inelastic collisions*. Second, within this kinetic energy range, the average distance traversed by an electron between two successive inelastic collisions, the *inelastic mean free path* (IMFP or λ),[70] is not larger than 2–3 nm for essentially all solids with the exception of alkali metals (see Fig. 7 and discussion below).[71] As the penetration depth of x rays is in the μm range, at energies used for XPS, only small fraction of electrons that leave atoms as a result of the photoelectric effect can reach the surface and escape into vacuum, and even smaller portion can make it without any energy losses. The latter set of electrons constitute the primary core-level peaks corresponding to the electronic shell they originate from, while those from the former group that lost energy on the way to the surface contribute to the background on the high binding energy side of core levels they are associated with [cf. Eq. (1), the larger the energy loss, the further away from the main peak they appear]. Calculated IMFP values for elemental solids can be found in Refs. 71 and 72, while Ref. 73 contains values for selected inorganic compounds. Experimentally determined IMFPs (measured by elastic peak electron spectroscopy) are also available for several elemental solids.[74,75] The dependence of IMFP on the electron kinetic energy $\lambda(E_{\mathrm{kin}})$ is similar for most solids and, therefore, often referred to as the "universal curve."[76,77] Within the electron energy range $0 \lesssim E_{\mathrm{kin}} \lesssim 50$ eV, IMFP decreases with increasing E_{kin} to reach a broad minimum at ca. 30–50 eV. For $E_{\mathrm{kin}} \gtrsim 50$ eV, IMFP shows a continuous increase with increasing electron kinetic energy. A direct consequence of that for XPS analyses, important to realize for each practitioner, is that the information acquired in a typical

© Author(s) 2022

measurement that involves several core-level spectra in general does not originate from the same sample volume (cf. the example of Mg—Al alloy discussed in Sec. VI A). This aspect is of minor importance for homogenous samples but becomes crucial in the analyses of samples with compositional gradients, such as multilayered films.

Another important term in the context of XPS surface sensitivity is the electron *effective attenuation length L*. While it is often used interchangeably with inelastic mean free path, it differs from IMFP in that it considers *elastic scattering* events.[12] In addition, while IMFP is a material property that depends only on electron kinetic energy, L is also influenced by the instrumental factors (e.g., whether polarized or non-polarized x rays are used). For the XPS practitioner, the effective attenuation length is of the higher relevance as it is used in all sorts of an overlayer thickness measurement (see Secs. V E, VIII A, and VIII B). Further reading on effective attenuation lengths and their use in XPS can be found in Ref. 78.

The third parameter used in quantitative description of XPS surface sensitivity is *probing depth*, *d*, often defined as the thickness of the top surface layer accounting for 95% of the total recorded signal intensity (equal to $3\lambda\cos\theta$ in the absence of elastic scattering, where θ is the *electron emission angle* with respect to the sample normal). d is typically in the range 6–9 nm, for the case when electrons are collected along the surface normal ($\theta = 0°$). Figure 7 shows calculated probing depths for several elements based on the IMFP values published by Tanuma *et al.*,[71] hence neglecting elastic scattering effects. Dots indicate probing depths for the strongest line of each element assuming that Al Kα x rays are used. The two cases that stick out with exceptionally large d values are two alkali metals—Li and Na. However, as Li 1s and Na 1s core levels are about 1000 eV apart, the probing depths differ greatly and are 16.1 and 6.0 nm, respectively. The fact that probing depth for Cs (not shown) is also exceptionally large indicates that the IMFP is largely determined by valence electron density and not so much the overall electron density. $d(E_{\mathrm{kin}})$ plots for all other elements shown in Fig. 7 indicate that probing depths, in general, do not exceed 10 nm.

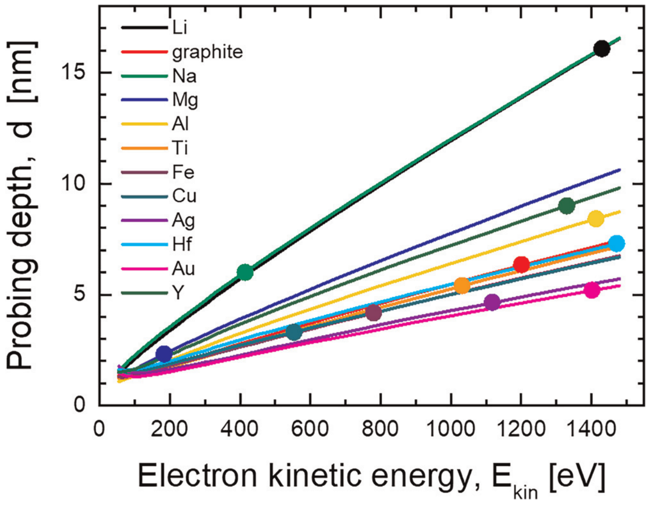

FIG. 7. Probing depth d as a function of electron kinetic energy for selected elementary solids. Values are calculated using IMFPs from Ref. 71; thus, elastic scattering effects are not accounted for. Dots indicate probing depths for the strongest line of each element, assuming that Al Kα x rays are used.

Other terms used to describe the XPS surface sensitivity are *information depth* and *electron escape depth*. The former describes the maximum depth from the surface from which a significant signal is obtained and, thus, can be seen as the more general definition of probing depth. The latter is equal to $\lambda\cos\theta$ (if elastic scattering effects are neglected).[12]

Surface sensitivity can be further enhanced by tilting the sample, in which case the probing depth decreases with the cosine of the electron emission angle (cf. Sec. V E). How far this effect can be exploited depends on the surface roughness as well as on the instrument type.

The surface sensitivity of XPS leads to concerns already on the experiment planning stage (see Sec. III A); how representative is the information acquired from the very surface? This is of serious concern for the analysis of both bulk and thin film samples. One must bear in mind that for a 1 μm thick layer (not untypical for thin films), the XPS probes less than 1% of the sample volume. Furthermore, the large portion of this probed volume is the interface of the film to the outside world meaning that the elemental and chemical composition are not necessarily representative of the entire film, especially after longer storage time in air (see the example in Sec. VIII A), where a surface contamination layer builds up. This is illustrated in Figs. 8(a) and 8(b), where survey and C 1s core-level spectra recorded from B_4C films are shown for samples after (i) minutes and (ii) weeks of air exposure, respectively. In the latter case, the survey spectrum contains a number of new peaks indicating that additional elements are present at the surface. Moreover, the O 1s signal is stronger, while C 1s and B 1s peaks are weaker as the sample signal gets attenuated in the contamination/oxide overlayer. The high-resolution C 1s spectra in Fig. 8(b) completely change the appearance after prolonged air exposure: C—C/C—H, C—O, and O—C=O peaks due to the so-called *adventitious carbon* (AdC), increase strongly while the C—B component originating from the B_4C film decreases. The above example shows that one should strive to analyze samples immediately after deposition, in the best case even without breaking vacuum, as the thickness of surface oxides and adventitious carbon contamination increases with air exposure time and may vary with climate season and laboratory air (conditioning) status. Removal of these contaminants without affecting the underlying film is often not possible (see Sec. III C).

The high surface sensitivity of XPS imposes restrictions on the vacuum quality during analyses, especially if one works with reactive surfaces. In such cases, acquisition of the representative spectra becomes a race against time as surfaces are getting coated with residual gas molecules. For these reasons, XPS needs to be performed under ultrahigh vacuum (UHV) conditions such that the monolayer formation times exceed the time necessary to collect all spectra. For freshly exposed metal surfaces (e.g., Ti after *in situ* Ar^+ sputter etch), it may be necessary to perform analyses under the

© Author(s) 2022

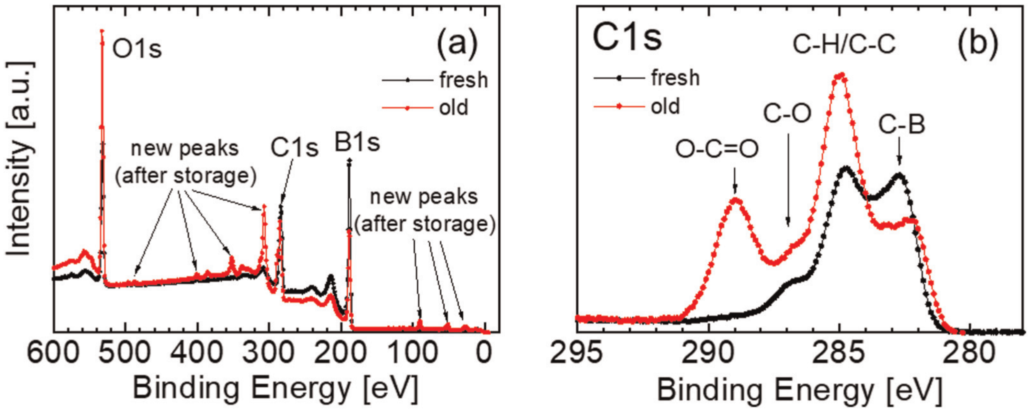

FIG. 8. (a) Survey and (b) C 1s core-level spectra recorded from B_4C films after several minutes (black) and several weeks (red) of air exposure.

base pressure better than the mid 10^{-10} mbar (mid 10^{-8} Pa or mid 10^{-10} Torr) range. To achieve such good vacuum conditions, a *bake-out* procedure is used. This means that the entire instrument is heated up to 120–150 °C for several hours in order for the water molecules (the main residual gas species, also most difficult to pump) to be desorbed and pumped away. Such procedure can be applied on regular basis and certainly after each intervention that requires venting the entire spectrometer.

Finally, all negative consequences of high surface sensitivity discussed above turn into advantages in studies where the very surface is in focus. Examples include exploration of catalytic activity and exposure to harsh environments as well as corrosion and wear studies. Hence, one should always consider whether XPS is the adequate technique to use for the purpose.

G. Surface charging

It is imperative that during the XPS measurement there is a continuous charge loss to vacuum because of photoemission. The charge neutrality condition requires that the loss of negative charge from the surface region (the consequence of the photoelectric effect) is compensated at a sufficient rate by electrons from the sample bulk, the substrate, or the surrounding environment. If that is not the case, the so-called *surface charging* takes place,[79] meaning that the surface charges positively, which effectively lowers the kinetic energy of emitted photoelectrons due to Coulomb interaction and, in consequence, results in a noticeable shift of spectral peaks toward higher BE values during analysis. Charging might also occur for specimens with relatively good conductivity if they do not make proper electric contact to the spectrometer as a result of, for example, bad mounting and/or the presence of thicker oxides on the surfaces in contact (test with an Ohm meter). For those reasons, the sample charging state is not known *a priori*, which implies charge referencing for remedy, i.e., the calibration of the binding energy axis against the signal of well-defined BE (cf. Sec. V B).

Additional complications come from *differential charging*, which means that different parts of the sample are not at the same electrical potential. This can be the case for inhomogeneous samples, especially if various phases have different conductivity. Differential charging might lead to peak splitting, i.e., the signal from the same element present in the same chemical environment, but in two different parts of the sample (characterized by different local conductivity) appears at different BE positions, corresponding to the potential difference between those sample regions.[80–82]

To enable analyses of non-conducting samples, dedicated low-energy electron or electron/ion guns have been developed (often called *flood guns*, see Sec. V C). While they compensate for the charge loss due to photoemission, they do not guarantee that the surface is electrically neutral,[83] which has consequences for charge referencing (see Sec. V B).

III. EXPERIMENT PLANNING

A. Is XPS the right technique to use?

This is absolutely the first question that should be posed before any XPS analyses; is this the right technique to use for the scope of the study? The answer depends on factors such as (1) what information is required, (2) whether the sample is suitable for XPS analyses (UHV compatibility, stability under exposure to x rays, size), (3) which part of the sample needs to be characterized (e.g., surface vs bulk), and (4) whether there are alternative better techniques available.

The primary reason for performing XPS is to obtain information about surface chemistry (chemical bonding) that is needed to determine the type and the relative amounts of bonding states within the first 5–10 nm of the surface. This information is extracted from the core-level spectra of all elements present in this layer by comparing peak positions with the reference values.[84–87] In some cases, spectra need to be peak fitted in order to separate overlapping peaks—this is, for example, the case when chemical shifts are of the same order as peak widths or if various core-level overlap (see Sec. VI C). In essence, the number, binding energy, and relative intensity of spectral features in the core-level spectrum of an element contain information about the type and concentration of its

© Author(s) 2022

bonding states. It must be emphasized that the presence of a given bonding type in the sample implies that the corresponding peaks need to be present in the core-level spectra of *all* elements that participate in the bonding. Thus, for a complete and self-consistent picture of surface chemistry, it is necessary to record and analyze core-level signals from all major elements present at that surface. Annoyingly, many XPS-containing papers neglect or omit this important part of analysis.

If the information about sample elemental composition is the prime requirement, XPS is certainly not the first choice. First, the *detection limit* of XPS is rarely better than 0.1–1 at. %, and in some cases like, e.g., light elements present in a heavy element matrix, detection limits above 10 at. % are not uncommon.[88] Second, XPS provides information from the surface region. Often surface composition deviates significantly from that in the bulk, due to the presence of contaminants like oxide artifacts. Removing the latter requires careful ion etching, at the risk of adversely affecting the surface composition (see Sec. III C). Third, quantification accuracy of XPS is rather poor (of the order of 5%).[89] Encouragingly, studies have compared the precision of different compositional analysis methods, like XPS vs Auger electron spectroscopy (AES), energy dispersion x-ray spectrometry (EDX or EDS), Rutherford backscattering spectrometry (RBS), elastic recoil detection analysis (ERDA), ion scattering spectroscopy (ISS), secondary neutral mass spectrometry (SNMS), and secondary-ion mass spectrometry (SIMS) for certain materials.[90–93]

B. The workflow

If the answer to the first question in Sec. III A was positive—XPS is indeed required—in the next step, we need to determine how the experiment should be performed to obtain useful and reliable answers. While the details of the most optimal data acquisition and instrument setup are discussed in Sec. V, we focus here on the overall experiment flow (see also Table II for a comprehensive summary of all steps). It is essential to identify already at this stage all variables that may influence the final outcome.

XPS is in many instances performed sequentially either on the same sample subjected to various treatments (e.g., annealing, etching, or nitriding) or on a series of samples (with varying composition, process temperature, etc.). In either case, the goal is to analyze the surface and conclude on the effect of experimental variables. For meaningful results, one has to ensure that the samples in a series are analyzed under similar conditions. First, the time between the treatment and the analysis needs to be the same for all measurements (irrespective of whether several treatments are performed on the same sample or on a sample series). Storing samples in air or in any sort of vacuum leads inevitably to AdC accumulation/oxidation (see Sec. VIII A).[94] None of these can easily be removed (see Sec. III C) as commonly applied noble gas ion etching tends to alter the elemental and chemical composition and structure of the underlying layers resulting in visible changes in core-level peaks.[65,95,96] For investigating the effects of each sort of surface treatments, the ultimate solution is to perform XPS analyses *in situ* and directly following the sample synthesis or processing, often in a step-by-step manner, i.e., with the spectra acquisition as a function of an increasing treatment dose. Otherwise, the effects of such treatments might be very likely masked by the oxidation during air exposure, which has profound impact on the elemental and chemical surface composition. For *ex situ* treatments performed in air (e.g., wear testing, lubricant evaluation, and all sorts of fatigue or corrosion studies), the time between treatment and sample loading into spectrometer should be kept to the absolute minimum and, equally important, should not vary between samples meant to be compared. Moreover, even the storage time in vacuum prior to XPS measurement (this would typically be the pumping time in the load lock chamber) should be maintained the same for all specimens as it is not *a priori* guaranteed that surface products of various *ex situ* treatments are stable in vacuum. Apart from that, the process of AdC accumulation takes place also in high vacuum environment,[97] predominantly due to the back-diffusion of pump oil molecules, so the amount of accumulated AdC increases with time. However, this can be mitigated to some degree by using “dry” pumps such as the scroll- and diaphragm-type backing pumps. While adhering to the guidelines outlined above tend to extend the whole experiment, it is, however, well-invested time as it allows conclusive results.

C. Ar^+ sputter etch: To clean or not to clean?

Unless dealing with samples that are deposited and analyzed *in situ*, XPS practitioners are faced with the dilemma of whether surfaces should be sputter etched with Ar^+ ion beam (using a device called *ion gun*) prior to analyses in order to remove surface oxides and contaminants. This leads to a compromise between recording spectra that are more representative of a surface oxide than the actual sample material and potential influence of sputter damage on the obtained results. There is no easy answer to the question in the title of this section; hence, the purpose of the presentation below is to make XPS users aware of all related issues, which may help in choosing the best practice.

While sputter damage effects caused by irradiation of surfaces with noble gas ions with energies in the range from several hundred to a few thousands’ eV have been known to the surface science community for decades,[98–101] it is disturbing when some refer to this treatment as “surface cleaning.” Such euphemistic expression risks to create an unfounded mind set among colleagues less experienced in XPS, who may consider spectra acquired from such ion-beam-exposed surfaces as being representative of the native (e.g., undisturbed) material. This notion needs to be confronted with the well-established fact that such irradiation induces overlapping collision cascades in the surface layer with the thickness defined by the energy and the incidence angle of an ion beam.[102,103] The ion-beam-induced artifacts include preferential elemental sputter ejection,[65,104,105] induced chemical reactions,[95,106–108] atomic mixing,[109,110] recoil and ion implantation,[111] structural disorder, amorphization,[112,113] surface segregation,[114,115] and surface roughening. The take-home message is that the sample surface should not be expected to be both clean and unaltered, unless synthesis and (immediate) analysis experiments are made *in situ* in UHV chambers.

The critical point is that with typically used ion energies and incidence angles, the thickness of the ion-beam-modified layer is comparable to the XPS probing depth (if working with the most common sources, see Sec. II F).[116,117] Hence, one has to be aware

© Author(s) 2022

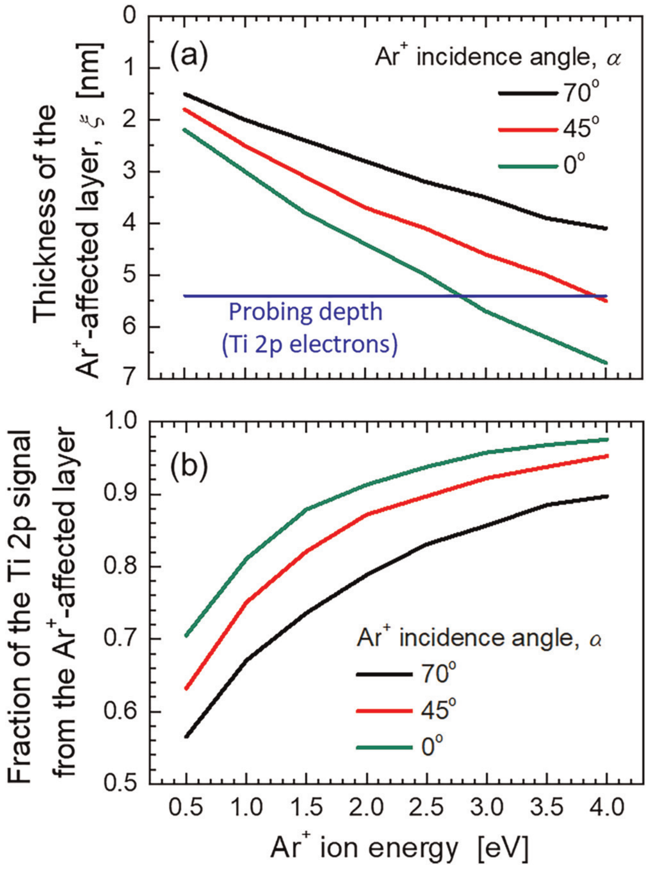

FIG. 9. Relation between the TRIM-simulated thickness of the surface layer modified by the Ar$^+$ ion beam during sputter-etch ξ and the XPS probing depth d for the model case of TiN surface. (a) ξ for the ion energy E_{Ar^+} varying in the range $0.5 \leq E_{Ar^+} \leq 4$ keV and for three values of the ion beam incidence angle $\alpha = 0°$, 45°, and 70° (with respect to the surface normal). The XPS probing depth for Ti 2p electrons emitted along the surface normal (in the absence of the elastic scattering effects) excited with the Al Kα radiation is indicated in blue. (b) The fraction of the Ti 2p signal that originates from the ion-beam-modified layer β for three values of the Ar$^+$ ion beam incidence angle, $\alpha = 0°$, 45°, and 70°.

that after such surface treatment, a significant fraction of the recorded signal originates from the layer that is not fully representative of the original material. This is illustrated in Fig. 9(a), for the case of a TiN surface irradiated by Ar$^+$ ions with the energy E_{Ar^+} varying in the range $0.5 \leq E_{Ar^+} \leq 4$ keV and for three values of the incidence angle $\alpha = 0°$, 45°, and 70° (with respect to the surface normal). For the ideal case of perfectly flat surfaces, the thickness of the surface layer modified by the incident Ar$^+$ ion beam ξ can be estimated from Monte-Carlo type Transport of Ions in Matter (TRIM)[118] simulations and equals the average primary Ti and N recoil projected range accounting for straggle.[119] For the shallow incidence angle ($\alpha = 70°$), ξ varies from 1.5 nm with $E_{Ar^+} = 0.5$ keV to 4.1 nm with $E_{Ar^+} = 4$ keV. The corresponding range for the Ar$^+$ beam incident along surface normal ($\alpha = 0°$) is 2.2–6.7 nm, while $1.8\text{ nm} \leq \xi \leq 5.5\text{ nm}$ for a common setting of 45°. These numbers can then be compared to the XPS probing depth d indicated in the figure for Ti 2p electrons. Here, it is assumed that the Al Kα radiation is used and the analyzed electrons are emitted along the surface normal in the absence of the elastic scattering effects (cf. Sec. II F). The inelastic mean free path data for Ti are taken from Ref. 71. Clearly, even for the case of shallow incidence angle and low ion energy, a significant fraction of the volume probed by XPS is affected by Ar ion beam: the collision cascade zone extends to 1.5 nm, which is only slightly shorter than the inelastic mean free path of Ti 2p electrons that amounts to 1.8 nm (corresponding to the probing depth of 5.4 nm). ξ increases with increasing E_{Ar^+} and decreasing incidence angle α, and for the 4 keV/45° setting it reaches 5.5 nm, which is the same as the probing depth. For $\alpha = 0°$ (ion beam incident along surface normal), the thickness of the Ar$^+$-modified layer exceeds the probing depth already with $E_{Ar^+} = 3$ keV.

In fact, the situation is even worse than depicted in Fig. 9(a) due to that the signal intensity decays exponentially with depth x, i.e.,

$$I(x) \sim \exp(-x/L(E_{kin})\cos\theta), \tag{8}$$

where $L(E_{\text{kin}})$ stands for the electron effective attenuation length (or electron inelastic mean free path λ if elastic scattering effects can be neglected, see Sec. II F). By integrating Eq. (8) between $x = 0$ and $x = \xi$, for electrons emitted along the surface normal, the fraction of the signal that originates from the ion-beam-modified layer β can be expressed as

$$\beta = 1 - \exp(-\xi/L(E_{\text{kin}})). \tag{9}$$

Figure 9(b) shows the $\beta(E_{Ar^+})$ plots for three values of the Ar$^+$ incidence angle, $\alpha = 0°$, 45°, and 70° and inelastic mean free path of Ti 2p electrons (excited with Al Kα radiation $E_{\text{kin}} \approx 1030$ eV) in Ti, $\lambda = 1.8$ nm,[71] (as no corresponding data for TiN are available). Even for the mildest practical set of etching conditions (shallow incidence angle of 70° and low ion energy of 500 eV), $\beta = 0.57$, meaning that even in the best case scenario a majority of the Ti 2p signal from TiN originates from the volume that was subject to overlapping collision cascades.[96] That fraction is highest at 90%–98% for the highest Ar$^+$ energy of 4 keV, which may be attractive for the purpose of high etching rate, but definitely not advisable. If one wishes to record spectra at larger depths, which requires higher etching rates, the possible solution is a two-step sequence consisting of high energy etch followed by, e.g., 0.5 keV etching step applied for the time long enough to remove the artifacts from the high-energy sputtering.

Thin films deposited by PVD methods are often grown with the assistance of ion bombardment, which provides adatom mobility and, in this way, helps to reduce growth temperature.[120] The ion energies involved are, however, an order of magnitude lower than those used during sputter etch performed prior to XPS analyses, hence, one cannot expect that the material structure after the latter treatment remains the same. Another difference is that PVD growth of compound films might be conducted under the presence of reactive gases, which are obviously absent during XPS sputter etch. Thus, preferentially resputtered lighter gas atoms are not

© Author(s) 2022

replenished from the gas phase and such layers become understoichiometric with visible effects in core-level spectra.[65,96] These types of changes are even more likely to take place in thin films deposited by other methods, in which case XPS sputter etch implies the first exposure to energetic Ar^+ ion flux.

It is worth mentioning that in XPS analyses of thin films with native oxide layers, the oxygen content assessed after sputter etching is often overestimated with respect to bulk values.[121–123] This has two reasons. First, overlapping collision cascades induced by energetic Ar^+ bombardment lead to forward implantation of O atoms. Second, redeposition of oxygen atoms from the vapor phase created during sputter etching is unavoidable. Both factors make it impossible to completely eliminate the O 1s signal for the case of reactive surfaces, even for samples that have inherently negligibly low bulk O concentrations. For that reason, it is critical to minimize the air exposure time in order to keep the starting amount of O atoms as low as possible.[124,125] This implies high-end UHV ambient conditions for the experiment.

Another factor that needs to be taken into account, while considering sputter etching, is the surface roughness. The ion beam typically hits the surface at an angle of 45° or more (from the surface normal); hence, self-shadowing may occur for films with high roughness resulting in that surface contaminants cannot be removed from some areas. This is, for example, the case for layers deposited by cathodic arc with stuck macroparticles (droplets of cathode material that solidify *en route* to the film surface).[126] If the geometry of the instrumental setup so allows, one may try tilting the sample toward the ion gun, while sputtering to alter the incidence angle and expose larger area to the ion beam. A drawback of this procedure is, though, that the thickness of the ion-beam-modified layer increases (see discussion above).

The issues outlined above make all sorts of compositional and chemical analyses challenging,[127–129] to the meaning not necessarily feasible. Thus, it motivates efforts toward developing non-destructive techniques.[66,130–133] In this respect, Ar ion cluster guns are becoming popular.[134] Their convincingly demonstrated benefits are, however, hitherto limited to organic materials.[135–137] Evidence for significant advantage for inorganic samples is still, however, very limited,[133,138] with only minor improvements reported in some cases.[139,140].

For the many reasons given above, it is recommended to consider prior to experiments whether the required information can be extracted from the spectra recorded from as-received samples. The key factor is the degree of spectral overlap between signal from the surface oxides and that from the underlying volume. If the chemical shifts between these two signals are large with respect to the peak width, the overlap can be minimal, meaning that the signal from the native sample volume can be easily separated and Ar^+-sputter etching becomes redundant. A good example of such a situation is the Ta 4f spectrum acquired from a Ta film with its native oxide shown in Fig. 6(b) and discussed in Sec. II E. The $4f_{7/2}$–$4f_{5/2}$ peaks from the surface oxide appear at ca. 5 eV higher BE than the corresponding signal from the unaffected portion of the film. This is much larger than the peaks FWHM (~0.5 and ~1.1 eV for metal and oxide peaks, respectively) and, what is critical in the case of core levels with spin-splitting, significantly larger than the $4f_{7/2}$–$4f_{5/2}$ energy separation (1.9 eV). Thus, the metallic portion of the Ta 4f spectrum can be reliably fitted (cf. Sec. VI C) and no Ar^+ etch is necessary. Unfortunately, for most sample situations, the spectral overlap between oxidized and pristine part of the spectra is severe. This is the case for the Cu 2p spectrum from the CuO/Cu film shown in Fig. 6(e). Here, the chemical shift between 2p doublets from metal and oxide is only 2.1 eV, i.e., comparable to the peak widths (~1.2 and ~2.5 eV for metal and oxide peaks, respectively), which together with the additional complication in the form of pronounced satellite structures [see also Sec. II E and Fig. 6(d)] introduces a large degree of uncertainty in the peak fitting process and calls for alternative solutions like Ar^+ etching.

In view of what has been presented above, one may consider recording spectra not only from the primary (strongest) core levels, but also from those that appear at lower binding energy (higher kinetic energy). Such electrons have longer mean free paths and, hence, larger fraction of the signal comes from the unaffected layer. For example, in the above case of TiN, one could probe the Ti 3p core levels located at ca. 33 eV binding energy, for which inelastic mean free path is 2.35 nm. The probing depth is then 7.05 nm, i.e., significantly larger than 5.4 nm in the case of Ti 2p electrons.

To summarize, one must be aware that Ar^+ "cleaning" apart from removing undesired surface oxides also physically and chemically damages the underlying layers, which constitute a significant portion of the volume sampled by XPS, in some cases up to 98% [cf. Fig. 9(b)]. Users should seriously consider whether ion etching is a necessary sacrifice or if alternative methods exist. For surfaces treated by ion beam, one needs to find means to evaluate the extent of surface damage (e.g., by comparison to the *in situ* work from the literature or attempt TRIM[118] or Molecular Dynamics simulations) before drawing conclusions from such spectra.

IV. SAMPLES

The nature of the XPS technique imposes several demands on the specimens. We signal here the more critical issues. For extended treatments, the reader is referred to references listed in Table III.

A. Sample selection

Sample candidates that would be appropriate for XPS analysis must be capable of withstanding severe treatments that include exposure to (i) UHV environment (meaning a 12 orders of magnitude pressure change) and (ii) to the intense x-ray flux (implying local heating and passing substantial electron current through the sample more or less evenly distributed). Moreover, these two factors apply simultaneously and for prolonged periods of time, up to several days in extreme cases. For conclusive analyses, it is, therefore, essential that the sample's elemental, chemical, and phase composition does not change during that time. Hence, confirming specimen stability should be the first step in XPS analyses, especially if no previous experience with given sample type exists. A first good indication might be to measure the time necessary to pump the load lock entry chamber containing samples from the atmosphere down to the high vacuum regime required before transfer to the UHV chamber where analyses are conducted. Significantly longer pumping as compared to the pump-down time for an empty chamber indicates that severe sample *outgassing* takes place and even though it not necessarily disqualifies the samples, it is certainly a warning sign. An unusually large increase in the

© Author(s) 2022

background pressure after sample transfer to the UHV chamber or continuous pressure increase is other indications of potential problems. If the XPS instrument is not at the same institute as where sample synthesis is made or the instrument is heavily occupied, the above outgassing test could well be performed in another relevant vacuum chamber. For samples that successfully pass this check point, the stability to x-ray exposure should be tested. At this stage, apart from watching the background pressure, which is a very rough measure of sample stability, it is highly recommended to record repeatedly a series of fast scans over the most prominent core-level regions as a function of time. This allows to detect all sorts of radiation-induced degradation such as bond cleavage or desorption of weakly bonded species.[141–145] Alternatively, survey spectrum (cf. Sec. VI A) can be recorded after the high-resolution scans, which are typically more time consuming, and compared to the initial survey. The complementary evidence in the form of mass spectrum of species that leave the sample might be provided by residual gas analyzer if available. For samples that exhibit signs of degradation without causing critical pressure increase that would prevent XPS analyses, one may consider using reduced x-ray power and/or frequent changes of the analysis area. The applicability of such solutions needs to be determined on individual bases.

While working with several samples that are introduced into UHV simultaneously to be analyzed in a sequential manner (time-efficient solution often applied to analyze a sample series), one has to take into account that the UHV exposure time prior to the measurement varies from sample to sample. In the case of samples with stability issues, this might lead to inconclusive results. Therefore, it is recommended to check for this effect by repeating the measurement of the first sample of the series after all other samples have been analyzed.

For the reasons mentioned above, particular care should be taken for samples that have been exposed to multiple *ex situ* tests such as corrosion or wear testing. Some products of such treatments might be volatile, which not only prevents meaningful analyses, but also might present potential permanent contamination risks for the equipment. Infamous elements to an UHV analysis chamber are Zn, Cd, Mg, Pb, and Sb as well as various residues, e.g., flux from soldering and brazing and lubricants from machining. Correspondingly, if the sample contains none of the above, but recorded XPS spectra indicate their presence, one should raise suspicion to the larger environment. In such case, it may be a good idea to check the instrument logbook for what samples were previously analyzed.

Another important point to make here is that even if the sample itself is UHV- and x-ray-compatible, problems with background pressure might appear due to the use of different sorts of adhesive tapes and ink pen for sample mounting and marking, respectively. Both should definitely be avoided, especially that well tested alternative solutions are available. Best mounting is by mechanical metal (Cu) clamping. Sample marking can be avoided by inscription with a diamond pen on their back side or marking the storage box. Mind the material of that box for its possible emission.

B. Sample handling

The high surface sensitivity of the XPS technique (see Sec. II F) implies severe demands on sample handling. While the person performing analyses is usually well aware of that fact, it is not necessarily the case for all colleagues who were handling those samples prior to XPS analyses. It is, therefore, essential to communicate sample handling requirements to sample owners before it is too late. Actually, a single fingerprint left on the surface has deleterious impact on XPS spectra. Figure 10 illustrates this point with recorded Hf 4f, N 1s, O 1s, and C 1s spectra from HfN thin film samples in the as-received state and after (intentionally!) placing the first author's fingerprint on the analysis area. It yields a massive increase in the amount of hydrocarbon species at the surface, as evident from C 1s spectra [Fig. 10(c)]. This contamination layer attenuates the signal from the actual film elements, cf. Hf 4f and N 1s spectra [Figs. 10(a) and 10(b), respectively]. Noteworthy is that not only intensity, but also the actual shape of the Hf 4f signal (composed of two overlapping 4f doublets due to HfN and HfO_x, cf. Sec. II E) is disturbed: the relative intensity of the peak at 17.4 eV increases after touching the sample. This is because of the change in the background shape: the $4f_{7/2}$ electrons from HfN are inelastically scattered in the hydrocarbon overlayer and contribute to the background increase on the high BE side of the HfN $4f_{7/2}$ peak, thus increasing the apparent intensity of the peak at 17.4 eV. The O 1s spectral envelope also changes shape after leaving the fingerprint on the surface [cf. Fig. 10(d)]: the relative intensity of the higher BE peak at 532.0 eV (due to C—O and O—C═O species of adventitious carbon, see Sec. VI C 3) increases with respect to that of the main peak at 530.4 eV (assigned to HfO_x). In this case, the observed increase is a cumulative effect of two factors: (i) an increase in the number of C—O and O—C═O species as evident by a slight increase in the intensity of corresponding peaks in the C 1s spectrum [see Fig. 10(a)] and (ii) an increase in the background intensity due to the inelastic scattering of O 1s electrons from HfO_x in the AdC layer.

A litmus test for fingerprint messing of samples is the signature of unmotivated high levels of Cl and Na in survey scans coming from sweat salt. For the record, attempts to chemically remove a fingerprint, like by trichloroethylene, will shift the contamination to species from that solvent.

For the reasons mentioned above, the sample area that is intended for XPS analysis should not be touched by any other surface(s) (gloves and/or tweezers included) at any stage starting from the time the specimen was prepared. This means that utmost care should be taken during storage and transportation (did the sample shake in that plastic box?) and mounting on the sample holder. To minimize these risks, sample characterization by other analytical techniques should be performed only after XPS analyses have been completed.

If the sample size needs to be reduced for XPS, special techniques need to be employed. In the case of thin film samples deposited on substrates that cannot be easily cut without the substantial risk of contact with other surfaces (e.g., by scissors), one should consider from the beginning using substrates in the XPS-optimized size.

Prior to insertion into the instrument, the sample surface should be blown with dry N_2 (alternatively with more expensive alternatives such as He or Ar) to remove particles and dust (expected to be there). All handling is done by using tweezers and powder-free gloves (not touching the surface to be analyzed though!). For electrically conducting thin-film samples, it is crucial that the top surface is in good electrical contact to the sample holder so that the sample and spectrometer's Fermi levels are

© Author(s) 2022

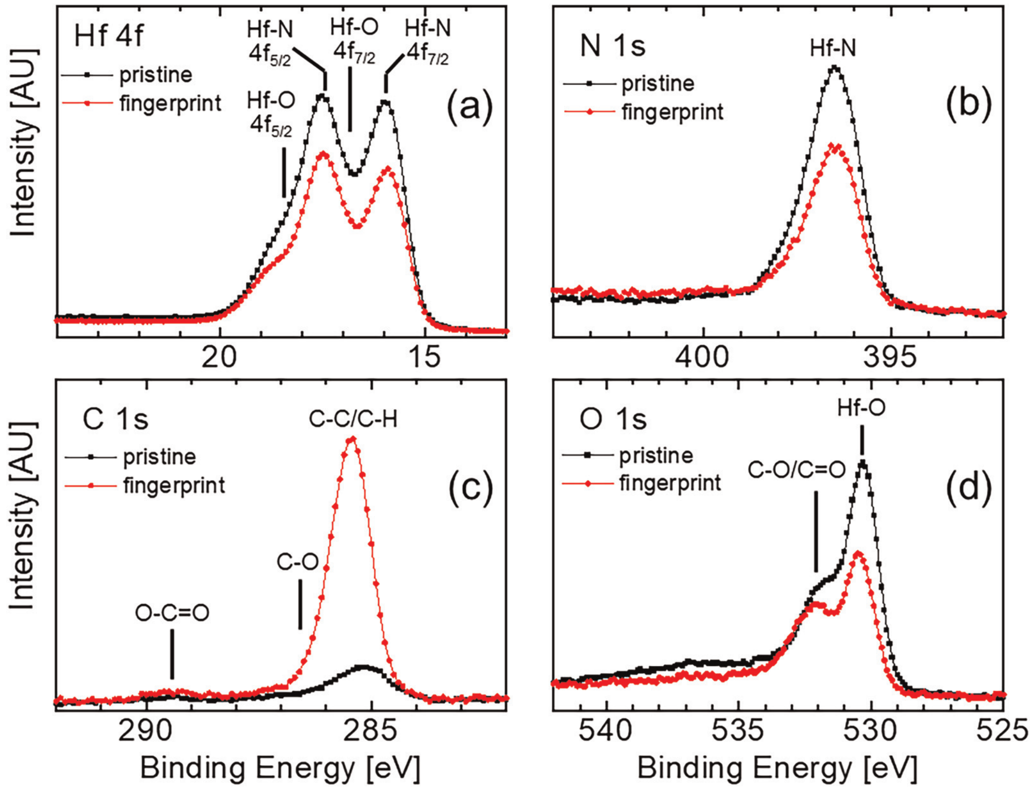

FIG. 10. (a) Hf 4f, (b) N 1s, (c) O 1s, and (d) C 1s spectra recorded from HfN thin film samples in the as-received state (black) and after making a fingerprint on the analysis area (red) are shown.

aligned (cf. Secs. II D, V A, and V B). For that purpose, metal clips are used to one's benefit.

Modern instruments allow for loading several samples on a single sample holder, which is beneficial if the same type of analysis should be performed on all samples. Special care should be taken to check the sample stability in UHV (e.g., products of oxidation, lubrication, fatigue, or corrosion tests performed *ex situ* might be volatile). The exposure time for the last sample in a series will be significantly longer than for the first one, which can lead to spectral misinterpretation in the case of unstable samples. If samples should be sputter-etched before analyses (see Sec. III C), the risk of cross contamination should not be underestimated. With unfortunate mounting (e.g., two samples mounted side-by-side in the direction of the incoming ion beam), material removed from one sample might get redeposited on other samples in the series.

C. The substrate role

Many of the thin film samples come on supporting substrates. There are various reasons that dictate the substrate choice and often XPS studies are not one of them, unless samples are intended specifically for surface analyses. In any case, there are a few aspects of XPS thin film work that are related to the substrate choice. The first, and most critical one, is the substrate conductivity. As discussed in Sec. II G, the charging phenomenon that occurs during XPS analyses of specimens with poor electrical conductivity seriously complicates the spectra interpretation (due to the charge referencing problem, see Sec. V B) and may lead to artifacts that are often not so obvious to recognize (e.g., extra peaks or features due to differential charging that can be mistaken for chemically shifted components). For those reasons, one should, whenever possible, use substrates with good electrical conductivity. So, implicate not the butler (substrate) as you set the stage for film deposition!

Another issue relevant to XPS work is the substrate roughness. This is for two reasons. First, the Ar^+ ion beam used either for removing surface contamination before analyses or for depth profiling experiments is typically directed at an angle that (depending on the instrument configuration) varies between 45° and 70° from the surface normal. Thus, for rough surfaces, some portions of the sample may be shadowed from the ion beam resulting in that the signals from the surface contaminants (typically C 1s and O 1s) persist despite prolonged etching. In the case of depth profiling, rough surfaces result in poor depth resolution, as the etching is uneven. The second reason why surface roughness plays a role is for angle-dependent studies (see examples in Sec. V E), in which case higher root mean square (RMS) values result in little

© Author(s) 2022

difference between spectra recorded at various *take-off* angles (i.e., angles between the electron emission direction and the surface plane). Films grown by PVD techniques (e.g., magnetron sputtering) tend to follow the substrate topography; hence, substrates with low roughness are preferred. For the reasons mentioned above, p-type doped Si(001) substrates with conductivity better than 1 Ω cm and the RMS roughness <0.5 nm are very suitable for XPS work (do not use non-doped ones). MgO or Al_2O_3 substrates are popular for epitaxial film growth; however, due to their insulating nature they can potentially work only for conductive films provided that a great care is taken to ensure proper grounding to the spectrometer.

Another factor that should be considered especially for work on very thin layers (<10 nm), in which case the substrate signal can still be detected in the spectrum, is the position of the strongest substrate peaks with respect to the core levels from the film. If the former peaks appear at lower BE, they will likely give rise to high background level in the energy range, where signals from the film appear. The consequence of that is poor signal-to-noise ratio and risk of very long acquisition times (cf. Sec. V H).

D. Reference samples

The data analysis can benefit if spectra from reference samples, recorded on the same instrument and under the same experimental conditions, are available. The impact of this premise increases with increasing sample complexity, which is a clear trend in modern materials science. High-resolution spectra become more complex due to signal overlap caused by more elements present and/or larger number of bonding configurations. Reference spectra obtained from samples with simpler elemental and chemical composition not only facilitate data analysis process, but also make it more reliable. Peak models obtained by fitting of less complex spectra from reference samples can serve as a valuable input to model overlapping spectral features. This issue is discussed in detail in Sec. VI C 1, where the parameters obtained from fitting of Zr 3d and B 1s spectra acquired from ZrB_2 and ZrO_2 reference samples (such as peak shape, FWHM, and energy splitting) are used to model the corresponding contributions in the complex Zr 3d-B 1s spectrum recorded from the ZrO_2/ZrB_2 sample. By limiting the number of degrees of freedom, the reliability of the fitting model is increased.

It is, thus, highly recommended that relevant references are included in the planned sample sets. Reference samples for the studies that involve *ex situ* testing should accompany the target samples in order to serve as controls.

E. Sample history

One consequence of XPS' high surface sensitivity is that sample history has a significant, if not dominant, effect on the analysis result. Factors worth to consider include sample preparation, storage time, storage environment, containers, sample handling, and possible exposure to x-ray or electron beams during earlier tests.[145,146] Each of them can potentially not only alter the conclusions from case to case, but even make the entire analysis meaningless. It is, thus, very critical that persons responsible for XPS analyses and data interpretation have a complete knowledge about the sample's past. If that person is not the sample owner, then good communication between all parties involved is necessary also to provide essential information such as expected elemental composition. *A priori* knowledge of sample elemental composition is crucial not only for data analysis but also for planning experiments as potential peak overlaps can be avoided by selecting alternative core-level regions. Comforting is that each factor from the list above is easily controllable to minimize (or even eliminate) the impact of the sample history on the final outcome, as discussed below in more detail.

In the ideal situation, the XPS requirements are considered already at the sample preparation stage. First, good planning helps to minimize the storage time by ensuring that XPS analysis is performed on freshly made samples. This also guarantees that no other analytical tools are used in-between, which removes any damage caused by earlier exposures to energetic radiation (electrons, ions, or x rays) and potential surface contamination due to sample handling involved. For films grown by PVD techniques like magnetron sputtering or cathodic arc deposition, the process parameters that may have decisive influence on the outcome of XPS analysis include background pressure, target purity,[147] and venting temperature.[124] Poor vacuum and/or low target purity levels likely result in the incorporation of C and O in the layers and, hence, oxide-free core-level signals cannot be obtained. Too high substrate temperature during ventilating the vacuum chamber may increase the thickness of surface oxides and result in high O levels even after prolonged Ar^+ etching.[124]

A prolonged air exposure has, in general, detrimental effects on the high-resolution core-level spectra (cf. the case of B_4C films discussed in Sec. II F). Except for noble metals or stoichiometric oxides, the native signal is obscured by chemically shifted peaks due to native oxide formation (cf. ZrO_2/ZrB_2 spectrum in Fig. 17 discussed in Sec. VI C) that often grow with exposure time unless the oxide layer passivates the surface. For transition-metal oxides, where vacancies often exist on both the metal and oxygen lattices, exposure to atmospheric moisture can produce off-stoichiometric surface compositions, which may cause unexpected peak shifts and/or broadening. This is accompanied by a continuous accumulation of adventitious carbon, which is essentially a contamination layer consisting of hydrocarbons and carbo-oxide species from the gaseous ambient. The composition of AdC layer was shown to depend on (i) the sample type, (ii) the environment, and (iii) the exposure time.[97] Some examples of C 1s spectra with AdC signature are shown in Fig. 21 and discussed in detail in Sec. VI C. The study was conducted on a series of transition metal nitride thin films exposed to laboratory air for the time periods ranging from 10 min to 7 months and showed a steady increase in the thickness of the C contamination layer. Because in the majority of cases there are no simple means of removing surface contaminants without affecting the original material (see Sec. III C), the rule is simple: perform XPS without delay.

The problems induced by accumulation of surface contaminants are obviously not present for samples that are grown in vacuum by PVD methods and analyzed *in situ*. As few labs have this possibility, various alternative solutions have been developed including vacuum suitcases or Ar-filled bags for sample transfer from the deposition system to XPS instrument, capping layers that

© Author(s) 2022

passivate the surface and are at the same time transparent to electrons,[66] *in situ* sample polishing,[132] *in situ* anneal treatments that trigger self-cleansing phenomena,[131] or cluster ion guns that minimize the sputter damage for some materials systems.[133–137]

V. DATA ACQUISITION

In this section, essential ingredients of successful XPS measurement are discussed. Before attempting any of the tests described below, one should always make sure that the instrument is in the stable state, e.g., that the anode has gone passed the ramp up (or "warm up") period. Practical parameters to keep an eye on are the filament and emission currents and the background pressure of the analysis chamber. It typically takes at least a couple of minutes before conditions stabilize.

A. Calibration of binding energy scale

In order to correctly represent the measured electron current intensity on the energy scale, the XPS spectrometer needs to be properly calibrated. The commonly used procedure[148] relies on measuring the positions of Au $4f_{7/2}$, Ag $3d_{5/2}$, and Cu $2p_{3/2}$ core-level peaks from sputter-etched metal foils[149] and comparing results to recommended values. According to the ISO 15472:2010 document for monochromatic Al Kα sources, these peaks should appear at 83.96, 368.21, and 932.62 eV, respectively.[148] Large BE spread between Au $4f_{7/2}$ and Cu $2p_{3/2}$ core-levels allows to test the dispersion of the BE scale. Any significant deviation from standard values implies that corrections are necessary. The implementation procedure is instrument-specific and performed according to instructions supplied by the vendor. Calibration should be done on a regular basis to minimize the risks of recording data with a poorly calibrated instrument. The frequency of calibration checks depends on the instrument. Good communication with instrument responsible staff is crucial. To be absolutely certain that the spectrometer is calibrated on the particular day when the analyses are performed, one may also consider adding a calibration sample to the sample set and using the factory instrument calibration check.[10]

The spectrometer calibration is very often confused with charge referencing (see Sec. V B). While the former guarantees the proper function of the instrument, it does not ensure that the core-level spectra recorded from any other sample (outside the calibration set) appear at the correct binding energy values. This is because the surface charging (see Sec. II G) cannot be *a priori* excluded. Hence, to distinguish peak shifts caused by charging from those due to chemistry, it is a necessary that an internal reference level is established, the so-called *charge reference*. This is a salient topic treated in Subsection V B.

B. Charge referencing

In principle, the charge referencing *per se* is not a part of data acquisition, but rather the first step in data analysis. However, due to a strong connection to the instrument calibration, we discuss these topics together.

In addition to a direct verification of whether surface charging takes place or not (see Sec. II G), the equally important purpose of the internal reference is to verify that the sample remains in good electrical contact to the spectrometer, i.e., that a common Fermi level is established across the sample/spectrometer interface by means of a transfer of charge (cf. Sec. II D). If that condition is satisfied, the Fermi edge, i.e., the center point of the abrupt drop in the DOS at the FL (cf. Fig. 11) denotes the "0 eV" on the BE scale. This is not necessarily the case even for metallic samples, as the presence of surface/interface oxides or other contamination may prevent good electrical contact either at the substrate/sample holder or at the sample/clamp interface.[150] In such cases, a direct scan over the energy region in the vicinity of 0 eV with fine energy step such as 0.05 eV helps to resolve the situation and uncover potential problems ahead of time. Fortunately, in many cases, native oxide layers are thin enough that the electric field induced by the surface charge buildup is high enough for tunneling to occur, resulting in charge transfer back to the spectrometer.

The availability of a reliable internal charge reference does not present a big challenge for conducting thin films in electrical contact to the spectrometer. Such samples typically exhibit a clear cutoff in the density of states at the Fermi level (called *Fermi cutoff* or the *Fermi edge*, FE), which serves as a natural zero on the BE scale. Figure 11(a) shows a few examples of the FE regions recorded from Au, Ag, and Cu sputter-etched samples used for instrument calibration. Although the recorded signal intensity varies between the three metal specimens, in all cases the abrupt drop at around 0 eV is observed. The cutoff position can be precisely determined from the signal derivative [cf. Fig. 11(b)], which has the form of a distinct peak. In the representative cases shown in Fig. 11(b), peaks are centered at 0 eV, which confirms correct instrument calibration and good electrical contact between the specimen and the spectrometer.

The usefulness of the FE from metal specimens for calibration of the BE scale was recognized already in the early 1970s.[151–155] At that time, FE of Pd or Ni was often used to establish the position of the core-level peaks such as Cu $2p_{3/2}$, Ag $3d_{5/2}$, or Au $4f_{7/2}$ on the BE scale. Both Ni and Pd are suitable for that purpose as they possess FE in the d-band of the conduction electrons, which provides relatively high signal intensity. This is a crucial point as even with modern spectrometers, measurements over FE with fine steps required (typically 0.05 eV or less) are time consuming.

The issue of charge referencing becomes also challenging, if not undoable, in the case of semiconducting or insulating specimens, as the position of the FL cannot be experimentally accessed. Numerous efforts have been undertaken to develop universal charge referencing procedures, including referencing to the C 1s peak of adventitious carbon (AdC),[156–158] noble metal decoration,[159–163] noble gas atom implantation,[164,165] deposition of organic layers,[166–168] "biased" referencing,[169,170] or the use of Auger parameters.[171–174] Each of these methods has limitations and problems and, consequently, the lack of an internal energy reference remains a fundamental problem/limitation in modern XPS.

The method based on adventitious carbon contamination is the most commonly used, predominantly due to its simplicity and the fact that AdC is handedly found on all samples exposed to atmosphere. The position of the C 1s peak of AdC is recorded and the C—C/C—H component of the C 1s spectrum is often set at the arbitrary chosen BE selected from the range 284.6 to 285.2 eV.[158]

© Author(s) 2022

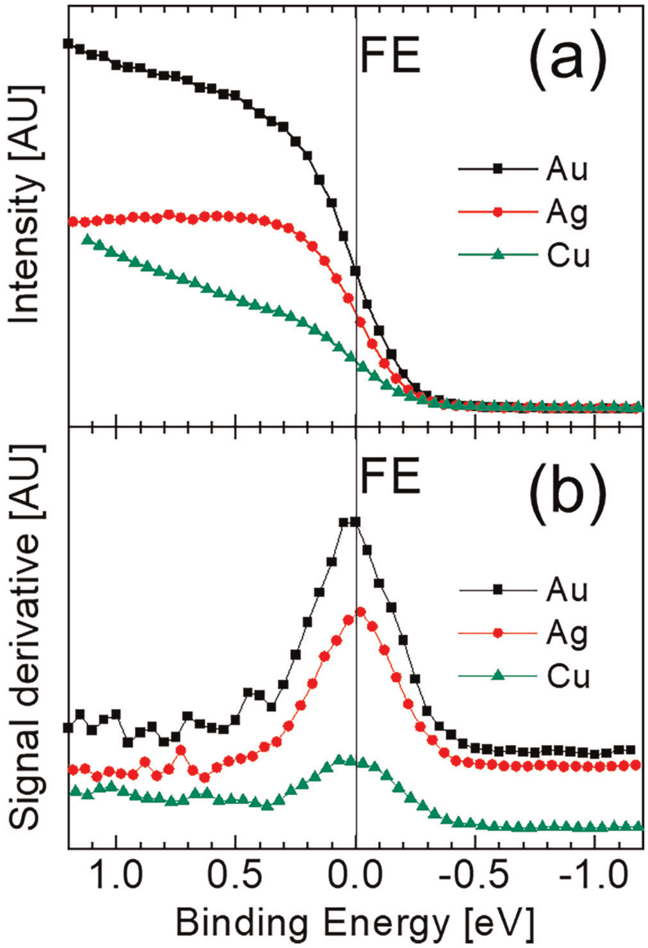

FIG. 11. (a) Fermi edge (FE) regions recorded from Au, Ag, and Cu sputter-etched samples used for instrument calibration. In all cases, the abrupt drop at around 0 eV is observed. The precise position of the FE is determined from the signal derivative (b). The fact that peaks are centered at 0 eV confirms (i) correct instrument calibration and (ii) good electrical contact between the specimens and the spectrometer.

Values outside of this interval are, however, not uncommon in the XPS literature.[97,175] The same rigid BE shift is then applied to all sample signals, hence assuming that the correction is independent of the electron kinetic energy.

It has to be emphasized that despite its broad use, the C 1s method has a 50-year-long history mapped by rather extensive criticism that appeared especially in 1970s and early 1980s.[176] The raised objections concerned the unknown chemical composition of the AdC layer,[177] its unknown origin,[178] and the uncertain or arbitrarily chosen position of the C 1s peak.[179–181] Markedly, with time, critical voices became overrun by the ongoing avalanche of XPS papers that rely on the AdC referencing. Is the majority always right in science?

Recent systematic studies on the use of AdC layers for BE referencing unequivocally confirmed early objections to this technique and identified additional problems.[94,182,183] In these experiments, the accuracy of the C 1s referencing was tested on samples that possess an independent (and reliable!) internal reference, i.e., the FL cutoff. This approach allowed to exclude potential influence of charging phenomena and lead to a number of conclusive results such as (a) the chemical nature of AdC depends on the substrate, the type of environment it has been exposed to, and the exposure time, (b) the BE of the C—C/C—H C 1s peak of AdC depends on the substrate it accumulates on, (c) it may vary by as much as 2.66 eV, which is more than typical chemical shifts, and *much more* than what is specified in the ISO and ASTM documents, and (d) the AdC layers are not in electrical equilibrium with the specimens they accumulate on, which results in vacuum-level (rather than the assumed Fermi level) alignment. As a consequence of that, the sum of the measured BE of the C—C/C—H C 1s peak of AdC and the sample work function ϕ_{SA} (obtained from the same surface by Ultraviolet Photoelectron Spectroscopy, UPS,[184,185] immediately after XPS analyses) is constant at 289.58 ± 0.14 eV.[183] The work function may vary by several eV from sample to sample and is known to be very sensitive to many variables like surface cleanliness,[186] roughness,[187,188] crystalline phase, or crystal orientation.[189] This obviously disqualifies the AdC method from charge referencing. Blind use of this approach can lead to unphysical effects such as density of states above the Fermi level[94] and in some cases contradicts the basic principle of photoelectron spectroscopy that the same chemical state gives peaks at the same binding energy.[190] We want to make our opinion clear that present international standards and many instrument manufacturers operational manuals are not providing all correct guidance in this matter.

So, the essential question (not only for this tutorial) is—how to reference XPS spectra? The following is our recommendation:

- For metallic samples, use the Fermi edge as the most reliable internal reference,
- For samples conductive enough to perform UPS, use the work method, that is, obtain sample work function in the same session as XPS (to be absolutely sure that the same surface is analyzed by both techniques) and set the C 1s peak of AdC at 289.58 − ϕ_{SA} eV.
- For insulating samples, there is currently no reliable referencing method—refrain from stating any binding energy for a fact and focus instead on spectral changes (either within sample series or with respect to the reference).
- All samples: abandon the conventional AdC-C 1s method that sets the C 1s peak at an arbitrary chosen BE—*no method is better than a wrong one.*
- Often it is not necessary to focus on extracting absolute BE values and more information can be obtained by analyzing evolution of spectral features in sample series.[124,191,201]

As a final note on this topic: one can still use the C 1s for referencing if the sample of interest contains known carbon compounds other than AdC. In such case, the problems mentioned above do not apply, as long as one is able to verify that the concentration of AdC at the surface is so low that it does not yield peak contributions in the C 1s spectrum.

© Author(s) 2022

C. Charge neutralizer (flood gun)

The cases where conductivity is confirmed to be sufficiently high are not so common, and with exception for metallic samples, in principle one can never *a priori* exclude the possibility that sample charges up during a XPS measurement. This is unfortunate as the surface potential has a direct effect on BE of core-level peaks, which is the essential information to be extracted and further used for identification of chemical states. Moreover, even during and after the measurement, it is difficult to completely rule out the influence of sample charging on the peak position, unless shifts are significantly larger than ∼2–3 eV, in which case it becomes obvious that they cannot be caused by changes in the chemical state. A good indicator for that one deals with charging (and not a chemical shift) is that all core-level peaks shift to higher BE (not necessarily by the same amount, though).

To neutralize the negative charge loss and to enable spectra acquisition from poorly conducting samples, low-energy electrons[192] or a combination of electrons and ions (supplied by the so-called *flood gun*) is used. It has to be emphasized that flood guns do not guarantee charge neutrality on the surface and more often under- or over-compensation takes place resulting in that peaks appear at either too high or too low BE.[83] Thus, these devices should not be considered a panacea for the charge referencing problem (see Sec. V B), although their usefulness is unquestionable and worthwhile spending time optimizing.

The use of charge neutralizers during XPS analyses requires caution. It is not uncommon that additional spectra features appear due to non-uniform (differential) charging. This possibility needs to be considered during spectra interpretation especially if it is known that samples are non-homogenous (in both lateral and vertical directions).

D. Energy resolution

Energy resolution in XPS should not be confused with the energy step selected for the analysis. The former is the smallest energy difference between two electrons that are still detected as arriving with different energy, while the latter determines the energy spacing between two adjacent data points in the spectrum. The energy resolution is determined by the instrumental factors such as dispersion of the x-ray source and monochromator and the energy resolving power of the analyzer.[193] Only the latter can be easily affected by selecting the pass energy E_{pass} value (see Sec. II A). While the specific values of pass energy that provide the best resolution are instrument-model specific, the general rule is that the energy resolution improves with decreasing E_{pass}. A useful measure of the instrument energy resolution can be obtained by measuring the Fermi edge from sputter-etched calibration samples such as Ag, Au, or Cu foils. Such measurement has the advantage over other methods that are used to quantify energy resolution (e.g., measurements of FWHM of the Ag $3d_{5/2}$ peak from sputter-etched Ag sample) in that it is independent of the natural core-level line width (see also Sec. II E). The idea is illustrated in Fig. 12(a), in which FE of Ag sample is recorded with different pass energies from the 110 μm^2 area centered in the middle of the sputter-etched crater. Clearly, the FE has a shape close to a step function in the case of the lowest $E_{\mathrm{pass}} = 10$ eV and becomes smeared out as the pass energy increases to 40 and 80 eV. We note here that the thermal broadening of the Fermi–Dirac function given by k_BT is ca. 0.025 eV at room temperature, i.e., with no impact on the discussed results. To get a quantitative measure of instrument resolution, one can differentiate the FE spectra and estimate the FWHM of resulting peaks. As can be seen in Fig. 12(b), in this particular example, the energy resolution varies from 0.82 eV with $E_{\mathrm{pass}} = 80$ eV to 0.32 eV with $E_{\mathrm{pass}} = 10$ eV. Noteworthy, the gain in resolution is accompanied by a severe drop in signal intensity (and, hence, the signal-to-noise ratio, cf. Sec. V H) as lower pass energy means that electrons passing through the analyzer have lower speed; hence, the number of electrons per unit time (e.g., electron current) decreases. The former conditions would be appropriate for survey (wide energy range) scans, in which case the focus is to obtain a spectrum with a high signal-to-noise ratio (cf. Sec. V H) to determine what elements are present in the sample. The latter condition would be selected for high-resolution (narrow range) scans that focus on revealing all fine details of core-level spectra on the expense of acquisition time that in extreme cases (core levels

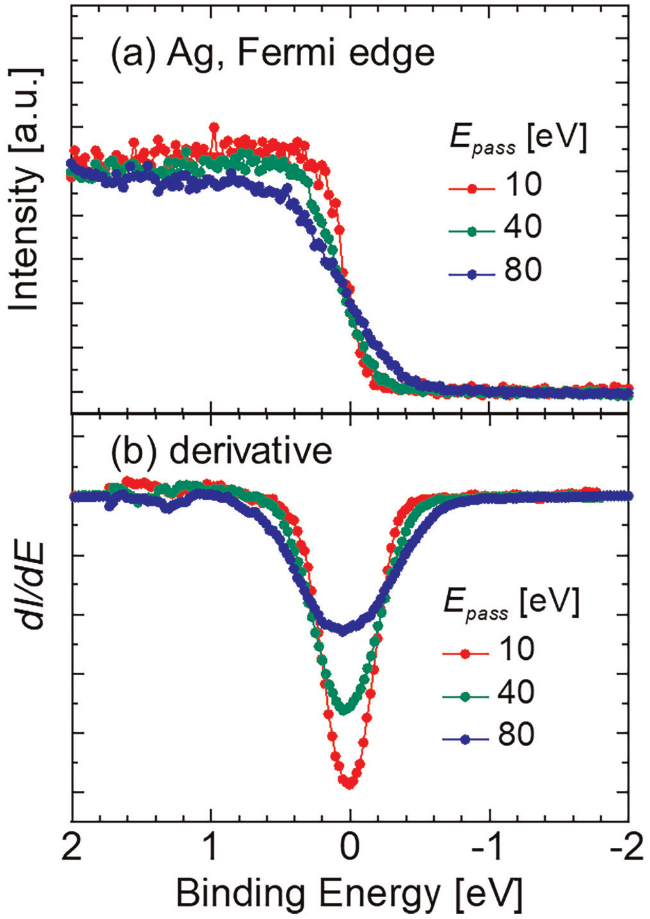

FIG. 12. (a) Fermi edge recorded from sputter-etched Ag sample with different values of pass energy. (b) Derivative of spectra shown in panel (a). The peaks' full-width-at-the-half-maximum is a measure of experimental resolution.

with low cross sections for photoionization and/or low element concentrations) may extend over several hours.

E. Electron emission angle

Another critical parameter to examine is the *electron emission angle* θ (conventionally measured from the surface normal), which directly affects the probing depth that varies as $3\lambda \cos\theta$ (see Sec. II F). In some treatments, a *take-off angle* ϕ is used instead (measured from the surface plane), in which case the probing depth becomes $3\lambda \sin\phi$. Varying the probing depth by varying θ is particularly useful in studies of chemical or elemental variations within the top 10 nm, provided that samples are sufficiently flat (i.e., the surface roughness is negligible in relation to the thickness of individual layers to be studied).[194,195] Some examples include surface oxides, contaminations, and treatment or degradation layers. An example of how large the spectral variation can be is given in Fig. 13, in which Zr 3d and B 1s core-level spectra acquired from air-exposed ZrB_2 thin film are shown. Detailed discussion on this signal-rich spectrum is presented in Sec. VI C. For the purpose, here we note that the sample has a structure (native oxide) ZrB_2 with major peaks identified as (in order from low to high BE) Zr $3d_{5/2}$ (Zr—B) at 179.0 eV, Zr $3d_{3/2}$ (Zr—B) at 181.4 eV, Zr $3d_{5/2}$ (Zr—O) at 183.5 eV, Zr $3d_{3/2}$ (Zr—O) at 185.9 eV, B 1s (B—Zr) at 188.1 eV, and B 1s (B—O) at 192.8 eV. With increasing electron emission angle θ, the effective probing depth decreases, which results in that the intensities of all peaks due to electrons originating from deeper-lying ZrB_2 volume (Zr 3d doublet at lowest BE and B 1s peak at 188.1 eV) decrease with respect to signals from the top oxide layer. At $\theta = 0°$, the former peaks dominate, while their intensities become negligibly small for $\theta \geq 75°$. This is a direct consequence of the fact that by tilting the sample between these two angles the probing depth is reduced approximately four times. The measurement principle illustrated with spectra shown in Fig. 13 is called *angle-resolved XPS* and constitutes basics of a *non-destructive depth profiling.*[196]

If the surfaces and interfaces involved are flat on the atomic scale, one can use tilt angle-dependent XPS for an estimate of the top layer thickness. This is done with the help of the Hill equation[197] as described in the end of Sec. VIII B.

Apart from the surface roughness another critical parameter that has a direct effect on the angle-dependent measurements of the type presented in Fig. 13 is the acceptance angle of the entrance slit of the electron energy analyzer (cf. Sec. II A).

F. Sample stability test

While working with new/unknown materials systems it is always advisable to perform a sample stability test prior to any further analyses. Contrary to common belief that XPS is a non-destructive technique, there is a solid experimental evidence for that the exposure to the x-ray beam may trigger a number of processes such as bond breaking, defect creation, changes in surface composition, desorption of weakly bonded species, amorphous-crystalline phase transition, interdiffusion, segregation, and melting.[141–145] All of these can be revealed by following spectral changes as a function of x-ray exposure time. The risk of beam damage is not as high as with AES, but cannot be *a priori* neglected especially with the use of focused x-ray sources for small spot XPS analyses. Organic materials are typically more prone to beam damage. One should, however, never take for granted that all other material classes exhibit excellent stability. Examples of inorganic materials that are sensitive to photon-induced damage are oxides and salts.

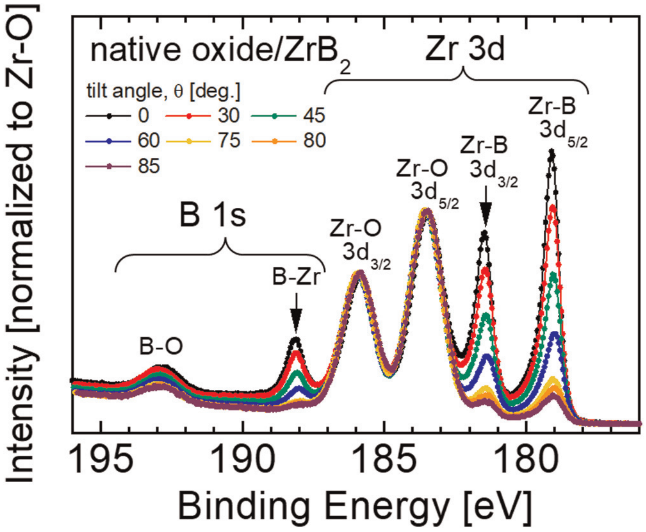

FIG. 13. Zr 3d and B 1s core-level spectra acquired from air-exposed ZrB_2 thin film. Spectra are recorded as a function of the electron emission angle θ that is varied from 0° to 85° (with respect to the surface normal) by tilting the sample. Since the effective probing depth decreases with increasing θ, the intensity of all signals originating from deeper-lying ZrB_2 volume decreases with respect to that from the top native oxide layer.

For particularly fast changes (on the time scale of seconds), one can with advantage use the snapshot function available on some instruments (e.g., Axis Ultra DLD, Kratos Analytical, UK), which allows to record core-level spectra without scanning the photoelectron energy. In such arrangement, the analyzer is set at the energy that corresponds to the center point of the core-level spectrum and the energy width of the recorded region is determined by the value of pass energy (ca. 10% of E_{pass}). This allows for acquisition with the time resolution of the order of one second or less on the expense of energy resolution.

The sample stability should be tested with instrument settings that are planned to be used during the actual data acquisition (the most critical one being x-ray power) and for the time period that is necessary to record complete set of spectra. If beam damage is detected, the possible remedy is to move the analysis area from one spot to another, while not exceeding the critical analysis time at each spot. One needs to be pay attention, though, to the actual x-ray spot size on the surface, which, in general, is not the same as the analyzed area.

G. Measurement sequence and selection of scan parameters

It is a good practice to start analyses with an overview (survey or wide range) scan typically covering as wide energy range as

© Author(s) 2022

feasible, starting from 1200 to 1300 eV (depending on the excitation source energy) and ending on the other side of scale, e.g., −2 to −5 eV. The goal is to acquire as many peaks as possible to get an idea about the type and concentration of elements present in the sample. For that reason, the signal intensity is of primary concern; hence, higher pass energy is preferred (cf. Sec. V D). In addition, survey spectra allow to: (i) determine exact energy regions for high-resolution scans, (ii) identify problems with peak overlap [cf. the case of N 1s and Mo $3p_{3/2}$ in Fig. 6(a)], (iii) get an idea about peak and background levels for core levels of interest, which can be used to determine the number of sweeps required for a certain signal-to-noise ratio (see Sec. V H), and (iv) check the contamination level (thickness of native oxide and adventitious carbon layers).

At this point, one has enough information to decide upon the further strategy, which needs to be chosen appropriately to the research question that needs to be answered. Typical concerns are as follows:

(i) should the sample be sputter-etched? (see Sec. III C)
(ii) should a charge neutralizer be used? (see Secs. II G and V C)
(iii) which core levels should be recorded with high energy resolution?
(iv) how long scanning time is necessary for core levels of interest? (see Sec. V H)
(v) should the core-level spectra be recorded sequentially (i.e., complete all sweeps over one region before moving to the next one) or in parallel (i.e., record the first sweep over all regions before recording the second one)? (see Sec. VI D)

In the next step, high-resolution (narrow-range) scans are conducted over regions of interest. For this, lower pass energy is used to improve energy resolution (see Sec. V D). The energy range is determined from a survey spectrum. Care should be taken not to truncate the spectrum on either side. The background often extends relatively far to the high BE side, thus adding several eVs does not hurt and pays back during spectral analysis. It is even more so, if peak fitting should be conducted, in which case the proper selection of background end points is critical for the final results. Thus, one has to be absolutely certain what constitutes the background level and what belongs to the spectral features. The energy step, ΔE typically in the range 0.05–0.1 eV, depends on the peaks' width and the absolute minimum is ten data points over the peaks' width, i.e., $\Delta E = FWHM/10$. The time per step (i.e., the dwell time) and the number of sweeps are selected based on the required signal quality (described in quantitative terms by the signal-to-noise ratio, see Sec. V H, which scales with the square root of the acquisition time) and the total acquisition time available. The latter is often limited not only by the instrument availability, but also by possible adsorption of background gas molecules on reactive surfaces. In most cases, it is possible to adjust the number of sweeps during data acquisition. If samples are laterally homogenous and not prone to beam damage (see Sec. V F), the analysis area is selected as large as possible to maximize signal intensity. If sputter etch is to be used, one needs to make sure that the selected analysis area is in the center of the sputter-etched crater.

One can in addition to the analysis that is performed at a specific area on the sample surface acquire line scans or even conduct area analysis to map out lateral changes in surface chemistry (see examples in Sec. VIII E). Other types of special measurements include angle-resolved XPS (cf. Fig. 13) and sputter-depth profiling (see Secs. VIII C and VIII D).

H. Signal-to-noise ratio

A very relevant question often asked while setting up the XPS measurement is—how long scanning is necessary? The lower time limit is set by the spectrum quality, which has to be sufficient for reliable conclusions. The upper limit is determined by the instrument availability and/or the analysis cost. Here, a very helpful but rarely consciously considered parameter is the signal-to-noise ratio (S/N), which allows to describe spectrum quality in a more quantitative way. S/N can be expressed as a function of peak and background intensity, P and B, respectively,[198]

$$\frac{S}{N} = \frac{P - B}{\sqrt{N_P^2 + N_B^2}}, \tag{10}$$

in which N_P and N_B are peak and background noise, respectively. Note that all quantities in Eq. (10) are measured in total counts (not counts per unit time, which is the most common way to plot XPS spectra). The fact that the S/N ratio apart from the signal strength also depends on the background intensity implies that typically S/N decreases with increasing BE due to the increase in the *inelastic background* level. Since N_P and N_B are expressed as a square root of the total number of counts, $N_P = \sqrt{P}$ and $N_B = \sqrt{B}$, Eq. (10) can be rewritten as

$$\frac{S}{N} = \frac{P - B}{\sqrt{P + B}}, \tag{11}$$

or in a more practical way as

$$\frac{S}{N} = \frac{P_1 - B_1}{\sqrt{P_1 + B_1}}\sqrt{n}, \tag{12}$$

where P_1 and B_1 are the peak and background intensities after the first sweep and n stands for the number of sweeps. While the two former quantities are determined by the specimen type and as such cannot be modified, the only choice for controlling the signal-to-noise ratio (for a given analysis area, pass energy, and x-ray power) is by selecting a proper number of scans over the energy region of interest. Many modern instruments offer the possibility to modify the number of sweeps during data acquisition, which greatly simplifies the task. After the first series of sweeps over core levels of interest has been completed, one may estimate based on obtained P_1 and B_1 values, how many sweeps are required for each spectrum to reach the satisfactory S/N ratio.

To illustrate practical implications of Eq. (12), we consider C 1s spectra recorded from two metallic thin film samples: Ti and Hf. Films were exposed to atmosphere for several months and as a result of that both contain a similar amount of adventitious carbon (AdC, see Sec. V B) at the surface. Figure 14 shows the survey spectra obtained from both specimens. Already at a first glance one can note essential difference: while the C 1s peak intensity is

© Author(s) 2022

similar in both cases, the background level is not. In the case of AdC/Hf sample, the C 1s peak is superimposed onto high inelastic background due to intense Hf 4f and Hf 4d lines (both with relatively high sensitivity factors, see Sec. VI D). In contrast, for the AdC/Ti specimen, the strongest signal from the substrate (Ti 2p) is at higher BE than the C 1s peak, thus the background level in the energy range 280–300 eV is low, determined by weak Ti 3p and Ti 3s lines (both with low sensitivity factors).

What are the corresponding consequences for data acquisition? Figure 15 shows two sets of narrow-range C 1s spectra from AdC/Ti and AdC/Hf samples recorded with identical instrument settings. The number of sweeps increases from $n = 1$ (at the bottom) to 300 (on the top). Obviously, for both samples, spectra quality improves with increasing number of scans. Despite the same C content at the surface, however, the signal recorded from the AdC/Ti sample appears “less noisy” as the background level is lower than for the AdC/Hf-sample C 1s spectra. This effect is quantified by the corresponding signal-to-noise values indicated in the figure. For the AdC/Ti sample, S/N = 2.7 after the first sweep, while in the case of AdC/Hf film even after five sweeps S/N is only 1.9. Similar spectra quality is obtained for AdC/Ti with $n = 5$ (S/N = 6.1) and AdC/Hf with $n = 30$ (S/N = 5.6). Thus, about six times longer acquisition is required in the latter case! Even after 300 sweeps S/N is relatively low at 15.1 for the C 1s spectrum of the AdC/Hf specimen. In contrast, the corresponding spectrum from AdC/Ti sample shows decent quality after 100 sweeps (S/N = 22) and after an additional 200 scans, the quality can be considered as acceptable (S/N = 36.2). Obtaining similar C 1s spectrum quality from the AdC/Hf sample would require about 1800 scans, which is not feasible. This illustrates problems that may arise during data acquisition and, at the same time, also suggest solutions like proper selection of substrate material. In general, the inelastic background implies that the higher the BE of the core-level signal of interest, the more effort is required to obtain high S/N values.

Other means of improving the signal-to-noise ratio include the use of higher pass energy or higher x-ray power. The negative consequence of the former is a worsened energy resolution (see Secs. II A and V D). As illustrated in Fig. 2 in the range of low E_{pass}, the gain in S/N is relatively large with minute increases in pass energy. Thus, if the energy resolution is not of a primary concern, higher E_{pass} values can be an attractive option to save measurements time. The negative side of using higher x-ray power is, however, a shortened anode lifetime.

To summarize, although the level of acceptable spectral noise may be a question of taste, S/N lower than ∼20 is acceptable only in exceptional cases (e.g., very low element concentrations and/or low photoionization cross sections that would require unfeasible

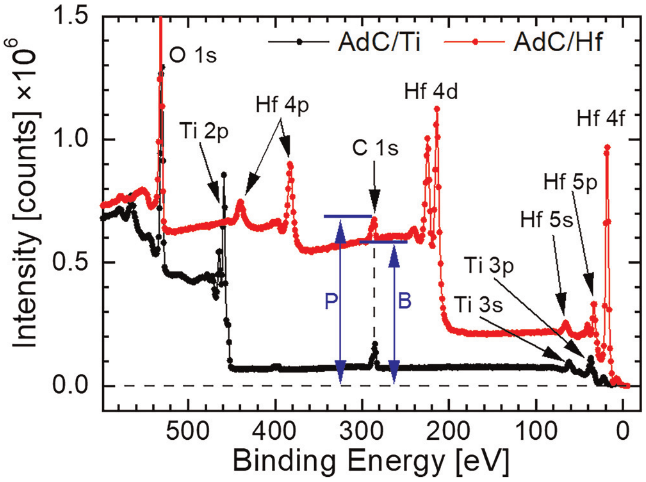

FIG. 14. Survey spectra recorded from Ti and Hf metallic thin film samples that were exposed to atmosphere for several months and, as a result of that, both contain a similar amount of adventitious carbon (AdC). Spectra are plotted with the absolute intensity numbers. *P* and *B* denote the total number of counts that correspond to the C 1s peak and background in spectrum recorded from the AdC/Hf sample, respectively.

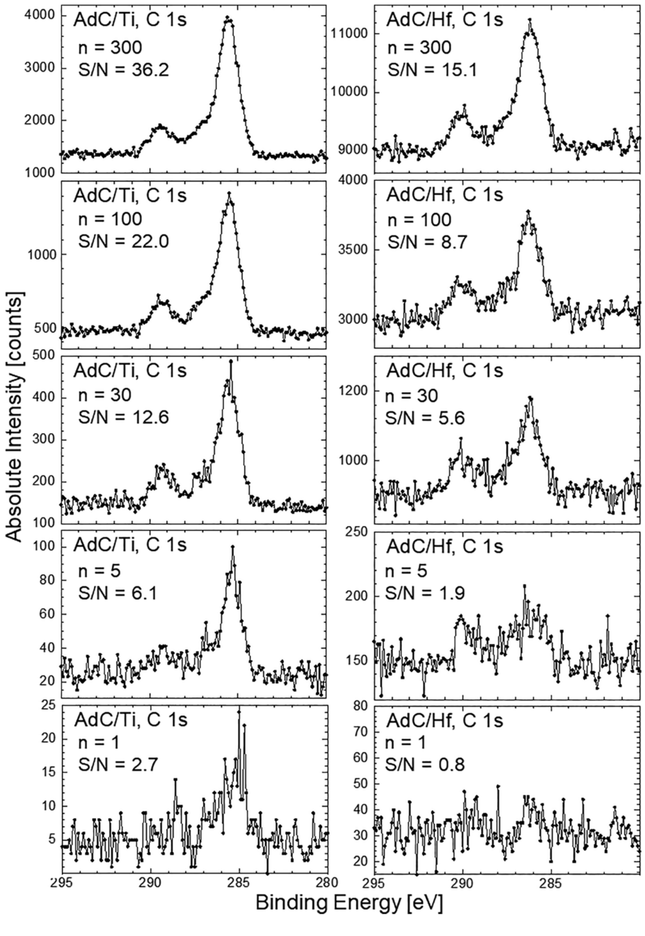

FIG. 15. Two sets of C 1s spectra acquired from (left) Ti and (right) Hf thin film samples covered with adventitious carbon (AdC) that illustrate the effect of signal-to-noise (S/N) ratio on the spectra appearance. All spectra are recorded with identical instrument settings. *n* denotes the number of sweeps. Both *n* and S/N decrease from top to bottom. Difference in spectra quality between AdC/Ti and AdC/Hf samples is due to significantly higher inelastic background in the latter case.

© Author(s) 2022

amount of measurement time). As a rule of thumb, S/N higher than ∼30 is desirable, while to ensure that no spectral detail is lost in the noise $S/N \gtrsim 100$ is necessary. For $S/N \gtrsim 200$, any noise becomes essentially invisible (one example is the Zr 3d spectrum shown in Fig. 13).

The signal-to-noise ratio has also other practical implications. It determines the signal measurement uncertainty (i.e., the experimental error in quantification) and detection limits, both of which are useful to assess. See Ref. 55 for further reading.

VI. SPECTRA ANALYSIS

A. Survey scans

The primary information extracted from wide-range (or survey) scans is the sample elemental composition. This procedure is referred to as *qualitative* elemental analysis and the question to be answered is *what* elements are present in the sample (in contrast to *quantitative* elemental analysis, which answers *how much* of each element is present in the sample, see Sec. VI D). Survey spectra are typically recorded with relatively high pass energy to ensure that the signal-to-noise ratio is high so that also weak signals are detected. The wide energy range ensures that peaks due to all core electron levels that can be excited with the incoming photons are acquired. As the electronic structure is element-specific, it is easy to verify what elements are present in the sample by comparing recorded BE values to XPS handbooks (see Refs. 45–51). The critical point is that the presence of a specific element is confirmed only if *all* its core-level peaks appear in the survey scan. For that reason, XPS is referred to as the *fingerprint* technique. The complete analysis of XPS survey scans requires that all peaks and other spectral features are identified (and labeled in a publication, preferably).

It is highly recommended to perform the analysis of survey scans *before* acquiring narrow range spectra. Not only to identify what core levels need to be recorded, but also what energy intervals should be used and what S/N ratios can be expected (and hence how long time the analysis will take). Doing things in this order saves time.

A thing to keep in mind when looking at the wide energy range scan is that the probing depth increases with decreasing binding energy (increasing electron kinetic energy). This is particularly important for samples with a non-homogenous composition such as multilayered thin films, layers with compositional gradients, or samples after all sorts of surface treatments (e.g., corrosion or wear tests). In such cases, one should carefully consider which core-level signals of a given element should be analyzed in detail—choosing the strongest lines (as is typically done) may not be the best option, as we scrutinize below for the case of Mg—Al alloy.

For the survey scan recorded with Al Kα radiation ($h\nu = 1486.6$ eV) that covers the range 1300-0 eV, the sampling depth confusion about compositional information can be substantial. Within this BE interval, the electron kinetic energy varies from 186.6 to 1486.6 eV [here we neglect spectrometer work function, which is relatively small, cf. Eq. (7)]. As an example, we look at Mg-Al alloy specimens, where one realizes that the 95% of the Mg 1s signal ($E_B = 1303.0$ eV, $E_{\text{kin}} = 183.6$ eV) originates from the first ∼2.3 nm, while the probing depth for the Al 2p electrons ($E_B = 72.9$ eV, $E_{\text{kin}} = 1413.7$ eV) is ∼8.4 nm, i.e., more than a factor of ×3 larger.[71] Hence, to ensure that the probed sample volume is similar for both Al and Mg signals it may be more relevant to record the Mg 2p core level ($E_B = 49.8$ eV, $E_{\text{kin}} = 1436.8$ eV). The effort cost in that case is rewarding, despite a significantly longer measurement time, as the photoionization cross section for the Mg 2p signal is more than 15 times lower than that of Mg 1s.

Survey spectra can also provide quantitative information about sample elemental composition. Due to poor energy resolution such estimates are not as precise as those based on narrow-range scans, yet they are useful if a quick estimate of sample stoichiometry is required.

In some cases, survey spectra also contain information about vertical distribution of elements.[199] Spectra recorded from multilayered samples with the top layer thickness comparable to (or shorter) than the XPS probing depth are a serving example. To illustrate that we show in Fig. 16, a set of survey spectra recorded from TiN/HfN bi-layer samples with varying thickness of the top TiN layer (from 0 to 42.7 nm). As the thickness of the TiN layer increases, all core levels from HfN (Hf 4f, Hf 4d, and Hf 4p) decrease in intensity due to signal attenuation in the TiN overlayer and eventually disappear completely once the TiN thickness exceeds ∼11 nm. Markedly, this is accompanied by a background increase on the high BE side of Hf core-level peaks, best visible in the case of Hf 4d doublet for the TiN thickness in the range 2–8 nm. The reason for the latter is an increase in the number of electrons that are emitted from the HfN film and inelastically scattered in the TiN overlayer [any loss of kinetic energy translates into higher binding energy, cf. Sec. II A and Eq. (1)]. Such electrons can be detected even in spectra recorded from samples with the overlayer thickness exceeding the effective attenuation length several times, i.e., too thick for any electron from the underlying layer to pass without collisions and be detected at the original peak position. This is the case for samples with TiN overlayer thickness of 10.7 and 13.3 nm. Eventually, not even these electrons are detected for yet thicker TiN overlayers (e.g., 42.7 nm) and the TiN/HfN survey spectra become indistinguishable from that acquired from the TiN film. Thus, peculiar background shapes, such as those observed for the samples with the TiN thickness in the range 2–8 nm, should not be neglected during analysis, especially if the element segregation is not *a priori* expected. When in doubt or undecisive for spectra interpretation, it is recommended to consult data from cross-sectional analytical transmission electron microcopy with elemental mapping. The combination of spectroscopy and microscopy is particularly powerful for surface as well as materials science.

B. Narrow-range (high-resolution) spectra

The main attractor of XPS analysis is the possibility of narrow energy range spectra, which are routinely recorded with lower pass energy settings to achieve high energy resolution (see Sec. V D). In order to extract authentic information about the surface chemistry, the process of XPS spectra analysis has to include all major core-level signals. The first thing to determine is how many peaks are expected for a single chemical state. As outlined in Sec. II E, except for "s" levels (even here with some exceptions!) one chemical state is represented by a spin–split doublet with a well-defined energy separation and area ratio. Hence, for a skilled practitioner, it is usually possible to determine upon a first glance how many chemical states of a given element are present. Often, spectra contain

© Author(s) 2022

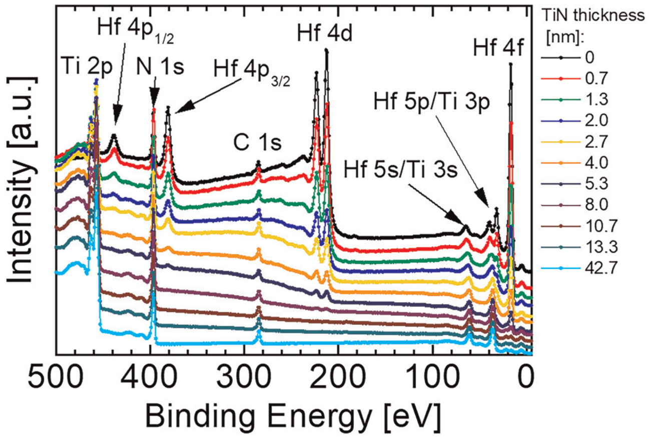

FIG. 16. Set of survey spectra recorded from TiN/HfN bi-layer samples with varying thickness of the top TiN layer (from 0 to 42.7 nm). As the thickness of the top TiN layer increases, all core levels from HfN decrease in intensity due to signal attenuation in the TiN overlayer and eventually disappear completely once the TiN thickness exceeds ∼11 nm. This is accompanied by a background increase on the high BE side of Hf core-level peaks, best visible in the case of Hf 4d doublet for the TiN thickness in the range 2–8 nm, caused by inelastic scattering in the top TiN layer.

multiple overlapping contributions, either due to chemical shifts being smaller than the peak width or the energy separation between spin–split doublets. Sometimes also the overlap with other core-level signals takes place. In such cases, to separate individual contributions, peak fitting is performed.

C. Peak fitting

In the process of *peak fitting* (also sometimes incorrectly referred to as deconvolution),[200] the background function is first selected to model the inelastic electron background and in the next step core-level spectrum is decomposed into two or more component peaks to best match the experimental data. The purpose of peak fitting is to extract information that may not be apparent from simple visual judgement of the recorded spectra. The most common peak shapes include Gaussian, Lorentzian, and the mixtures thereof (Voigt functions), while to model a background linear, Shirley or Tougaard functions are used.[15] In the ultimate case, the self-consistent peak models of all major core levels provide a complete description of surface chemistry. As correctly performed peak fitting requires much time and effort, one should always first consider whether it is indeed necessary to peak fit the spectra. For example, if quantification is the only purpose of XPS analysis and there are no overlapping signals that need to be separated, the peak fitting becomes redundant. Quantification can be equally well done based on peak areas (provided that the S/N ratio is high enough, see Sec. V H); hence, only proper background selection is necessary.

Peak fitting is recommended in the following situations:

- for quantification on samples where core-level spectra overlap and no alternative signals can be recorded [cf. the N 1s spectrum of MoN shown in Fig. 6(a), which overlaps with the Mo $2p_{3/2}$ signal], and
- for quantification of chemically shifted components in the core-level spectrum of the same element.

Often the peak fitting is followed by direct comparison of extracted peak positions to BE values published in XPS databases or in the literature. Based on that comparison, peaks in the fitted spectra are assigned to particular chemical bonds that are then claimed to be present at the surface. While there is nothing fundamentally wrong with this approach, it suffers from the fact that the reported BE values for the same chemical state of a given element may show a spread, which is of the same order as the BE difference between two different chemical states. For example, the NIST database[54] contains 91 entries for TiO_2 with the Ti $2p_{3/2}$ BE varying from 458.0 to 459.6 eV ($\Delta BE = 1.6$ eV!) and O 1s from 529.4 to 531.2 eV ($\Delta BE = 1.8$ eV!). Another often studied material system is Al_2O_3 (60 entries), in which case the Al 2p peak position varies from 71.1 to 76.2 eV ($\Delta BE = 5.1$ eV!), and that of the O 1s peak from 528.3 to 533.1 eV ($\Delta BE = 4.8$ eV!). The compounds mentioned within themselves obviously exhibit polytypism, variation in stoichiometry, lattice defects, and contamination. A relevant question for one's sample is then if a match to reference values should even be expected. Making comparison of obtained spectra to those from pure single-crystal references may nevertheless be valuable. The problem is most severe for oxides due to the insulating character of such samples and the necessity of using charge neutralizers (see Sec. V C). It does, however, occur also for samples with very good conductivity including metals, e.g., ($\Delta BE = 1.0$ eV for Zr $3d_{5/2}$ peak of metallic Zr).[54] Such large spread in reported BE values clearly prevents unambiguous assignment of observed spectral features and, in the worst-case scenario, creates room for "proving" the existence of *a priori* assumed bonding states. Thus, relying exclusively on the comparison to databases implies significant risks of incorrect bonding assignment, an arbitrary spectral interpretation, and, in the end, contradictory and often unreliable results.

For these reasons, in the peak fitting workflow suggested below the strongest emphasis is put on the qualitative and quantitative self-consistency between core-level spectra of all elements present in the sample.[201] The credibility of analysis is further enhanced through the use of properly selected reference samples. Detailed point-by-point description of the workflow follows in Secs. VI C 1–VI C 6 using as examples the real case studies of oxide growth on polycrystalline ZrB_2 and TiN films deposited by dc magnetron sputtering.

1. The role of less-complex (reference) samples

It is recommended to perform peak fitting in an order of increasing complexity, i.e., starting with the spectra that contain less features and are, hence, easier to fit. Typically, this would be data acquired from the properly selected reference samples (see Sec. IV D) that are characterized by simpler chemical and/or elemental composition. The details of such peak model (peak positions, energy separation, area ratios, and more) can then serve as an input for fitting spectra obtained from more complex materials, where peak overlap is likely to take place. The critical point is that spectra from reference samples should be recorded under the same experimental conditions as those from the series of interest. For that consistency reason, using reference spectra from literature is not advised. The best practice is to include reference samples in the planned sample set and to obtain spectra from all surfaces in one data acquisition session, which also eliminates possible influence of day-to-day variation in the instrument performance.

As an example of how useful the reference samples can be, we consider the peak fitting of Zr 3d core-level spectrum recorded from air-exposed ZrB_2 thin film shown in Fig. 17. The spectrum is quite complex and shows (at least) six different peaks of varying intensity, width, and shape. The peaks are tentatively identified as (in order from low to high BE): Zr $3d_{5/2}$ (Zr—B) at 179.0 eV, Zr $3d_{3/2}$ (Zr—B) at 181.4 eV, Zr $3d_{5/2}$ (Zr—O) at 183.5 eV, Zr $3d_{2/2}$ (Zr—O) at 185.9 eV, B 1s (B—Zr) at 188.1 eV, and B 1s (B—O) at 192.8 eV. The detailed fitting of such complex spectrum aiming at extracting relative fractions of Zr—B and Zr—O bonds is, however, complicated because of the severe overlap between all components and, if attempted without any extra input, would likely result in a peak model of low reliability. For that reason, we use as an input detailed peak models developed for Zr 3d spectrum of ZrO_2 sample [cf. Fig. 17(c)] and Zr 3d/B 1s spectrum of native ZrB_2 surface [cf. Fig. 17(b)]. The latter is obtained from the ZrB_2 film passivated with a few nm thick Al capping layer applied right after the growth, i.e., without exposing the film to air.[66] All spectra are fitted with the most popular Shirley backgrounds. The Zr 3d portion of the spectrum from native ZrB_2 surface features a pair of $3d_{5/2}$–$3d_{3/2}$ spin–split peaks with pronounced asymmetry due to significant DOS at the Fermi level giving rise to additional energy losses, which can be well-modeled by a blend of Doniach–Sunjic[202] and Gaussian Lorentzian functions available, for example, in the CasaXPS software. The obtained $3d_{3/2}/3d_{5/2}$ area ratio is 0.66, i.e., essentially the same as theoretically expected 2:3, which justifies the choice of fitting functions. The FWHM values for both peaks are very close at 0.50 and 0.53 eV, while the BE splitting is 2.38 eV. The B 1s peak is fitted with Voigt function (20% Gaussian and 80% Lorentzian). The Zr 3d spectrum of ZrO_2 features symmetric peaks (due to the insulating nature of this material) that are well-represented by Voigt functions (70% Gaussian and 30% Lorentzian) with the $3d_{3/2}/3d_{5/2}$ area ratio of 0.68. The peaks FWHM are 1.14 and 1.15 eV, while the BE splitting is 2.38 eV (i.e., identical to that of Zr 3d peaks in ZrB_2).

In the next step, the peak shapes (for Zr 3d and B 1s peaks), $3d_{3/2}/3d_{5/2}$ area ratios, the $3d_{3/2}$–$3d_{5/2}$ BE splitting, BE splitting between the B 1s and Zr $3d_{5/2}$ peaks (9.02 eV), obtained from fitting the native ZrB_2 and ZrO_2 spectra are used to model the spectrum of oxidized ZrB_2 shown in Fig. 17(a). To make sure that these parameters remain at the required values, we use the constraints available in the CasaXPS software. The highest BE peak due to the B 1s signal of B—O bond is modeled with the same line shape as the B 1s B—Zr peak, that is (20% Gaussian and 80% Lorentzian). As can be judged from the figure the fit quality is very good, the fitted curve (shown in red) closely follows the raw data. The obtained Zr—O/Zr—B ratio is 1.53.

Another example of crucial role of reference samples is the modeling of Ti 2p spectra of TiN films exposed to higher temperatures (referred to as venting temperature, T_v, see Figs. 18–21).[201] In this case, the spectra from TiN film capped with Al passivation layer to prevent oxidation are used.[66] Ti 2p and N 1s spectra obtained from such sample are representative of native TiN and, once fitted, can properly represent the signal from the non-oxidized volume of heat-treated TiN films. As shown in Fig. 18(a), the Ti 2p spectrum requires to be fitted with two pairs of spin–orbit split $2p_{3/2}$–$2p_{1/2}$ components corresponding to the primary and the satellite Ti–N peaks. The first pair (denoted as "TiN" and indicated in blue) appears at 455.0 and 461.0 eV, respectively, while the satellite features ("TiN-sat" shown in green) are shifted by 3.0 eV toward higher BE with respect to the primary peaks. The presence of satellite peaks in the TiN spectra is well documented in the literature although the exact origin is still debated.[58,203,204] Satisfactory fit of

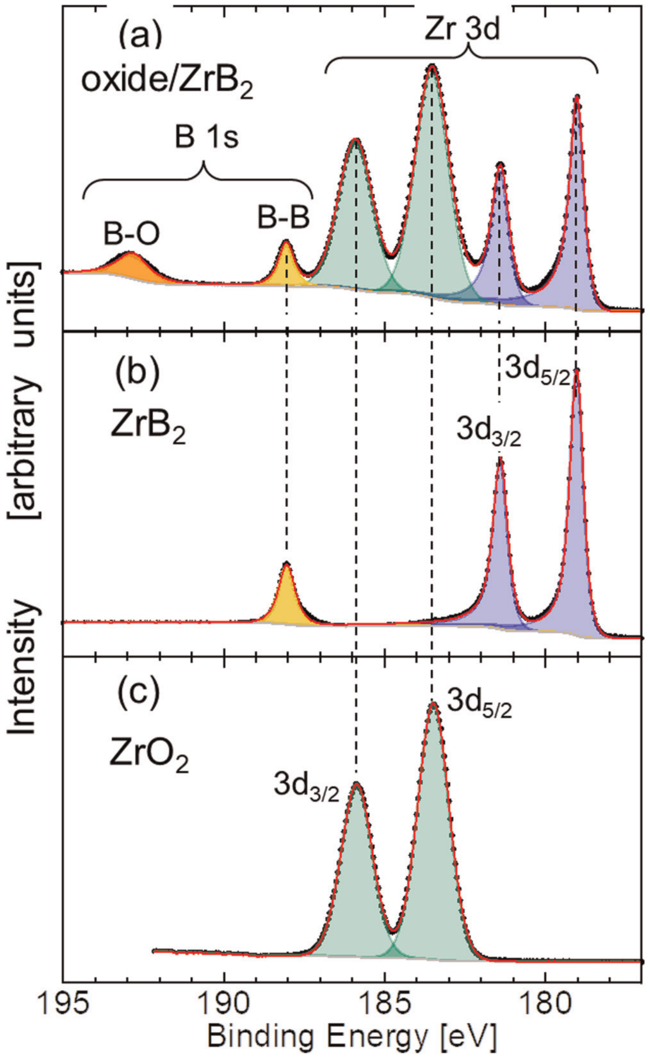

FIG. 17. Illustration of the central role of reference ZrB_2 and ZrO_2 samples for reliable peak fitting of complex core-level spectra of air-exposed ZrB_2 film with native oxide. Zr 3d/B 1s core-level spectra recorded from (a) air-exposed ZrB_2 thin film, (b) the ZrB_2 film passivated with a few nm thick Al capping layer applied right after the ZrB_2 growth, i.e., without air exposure, hence representative of the native ZrB_2 surface, and (c) ZrO_2 film. The details of background and peak functions used for fitting are described in the text.

© Author(s) 2022

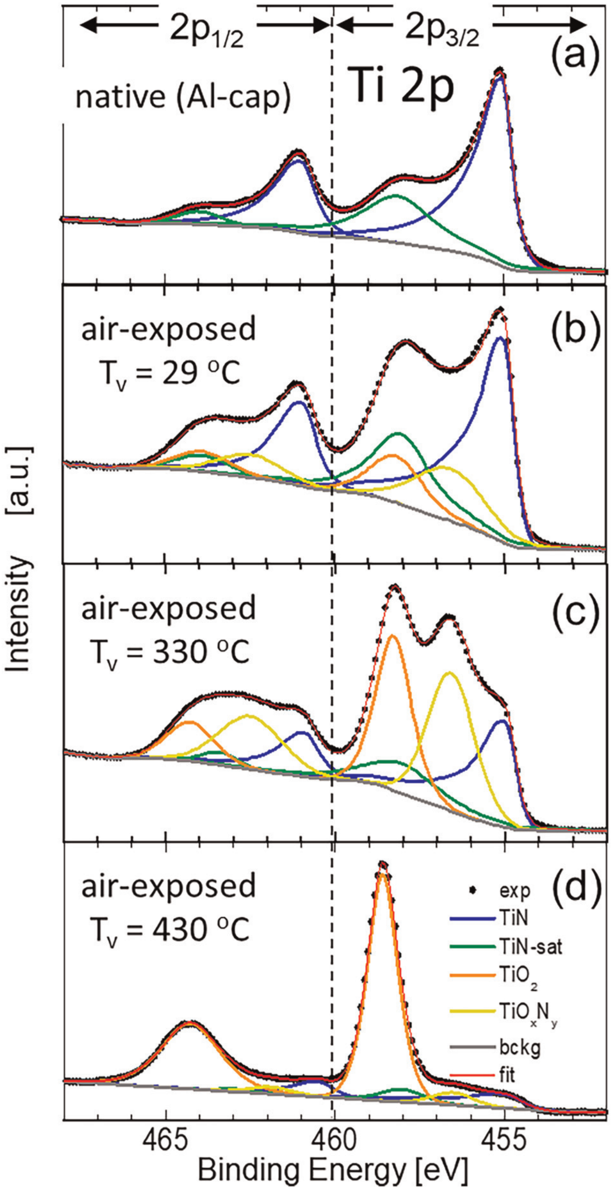

FIG. 18. Set of Ti 2p spectra obtained from TiN films: (a) *in situ* capped with 1.5-nm-thick Al layer to protect the surface from oxidation, [(b)–(d)] uncapped and exposed to atmosphere at different venting temperatures T_v ranging from 29 to 430 °C. [Reproduced with permission from Greczynski and Hultman, Appl. Surf. Sci. **387**, 294 (2016). Copyright 2016 Elsevier.] Some details of fitting models are modified to account for the recent developments in the charge referencing techniques (cf. Refs. 64, 140, and 141) and to make the treatment more pedagogic.

Ti 2p spectrum requires that asymmetric functions are used for the main components, which can be explained by energy loses due to simultaneous excitations of valence electrons, as the density of states near and at the Fermi level is high. TiN-sat peaks are well-represented by Voigt functions with 95% Lorentzian ingredient. The corresponding N 1s spectrum shown in Fig. 19(a) is composed of the TiN peak centered at 397.3 eV and the low-intensity satellite feature on the high BE side of the main peak at 399.4 eV. The extracted N/Ti ratio is 1.02, in very good agreement to the bulk value of 1 ± 0.01 obtained from RBS. In the next steps, the obtained parameters such as (i) the peak shapes, (ii) $2p_{3/2}$–$2p_{1/2}$ BE splitting, (iii) the $2p_{3/2}/2p_{1/2}$ area ratios for pairs of TiN and TiN-sat peaks, (iv) BE splitting between the TiN and TiN-sat peaks, and (v) the relative TiN/TiN-sat peak area ratios serve as input in more complex peak models of oxidized TiN surfaces to model the signal from the unaffected volume (see Ref. 201).

The use of the above constraints is critical for correct modeling of Ti 2p spectra of TiN films exposed to higher temperatures especially since new peaks, which appear as the result of oxidation, overlap completely with TiN signals from the unaffected volume (e.g., the TiO_2 component with TiN satellite). Only by coupling the area and BE splitting of the TiN-satellite peak to the Ti–N peak (which is not overlapping with TiO_2 signals), a proper estimate for the area of new peaks, due to TiO_2 and TiO_xN_y formation, can be obtained. The BE values for the two latter components are determined by examining the spectra obtained after exposure to higher temperatures, in which case these new signals become more pronounced. The BE of the TiO_2 peak is best determined from the spectrum obtained after $T_v = 430$ °C [cf. Fig. 18(d)], while the BE of the TiO_xN_y peak is determined from the sample exposed to 330 °C [cf. Fig. 18(c)].

It is important to note that the Ar^+-etched surfaces should, in general, not be considered as reliable reference samples due to often observed detrimental effects of the ion irradiation on the core-level spectra in the form of new peaks or peak broadening (see Sec. III C).[96] For transition metal (TM) compounds, these effects seem to become more pronounced with increasing TM mass as the preferential resputtering of lighter component (N, C, O, or B) is enhanced. TM carbides seem to be an exception as Ar^+ effects are relatively small.[96]

2. Include all major core levels in peak modeling

The peak fitting should not be limited to the core-level spectrum of one selected element unless there is only that element present. The latter is rarely the case as unintentional oxygen and carbon contamination in the analyzed surface region is difficult to avoid, not only during sample transfer to the XPS instrument, but also during the film growth with commercial purity targets and gases under high vacuum conditions.[147] One should, thus, strive to present a comprehensive model of the surface chemistry by peak fitting all major core-level signals. Such approach, based on larger volume of experimental evidence, results in much more reliable analysis provided that the peak fitting satisfies criteria of *qualitative* and *quantitative self-consistency*, formulated below. This is exemplified by the case study of TiN oxidation (cf. Figs. 18–21), where apart from Ti 2p and N 1s spectra, also O 1s and C 1s spectra are considered.

3. The criterion of qualitative self-consistency across all core-level spectra

The presented peak models for all core-level spectra should show qualitative self-consistency. That is, the presence of peak *A1* in the fitted spectrum of element *A* assigned to A_mB_n formation requires that the corresponding *B1* peak is present in the core-level

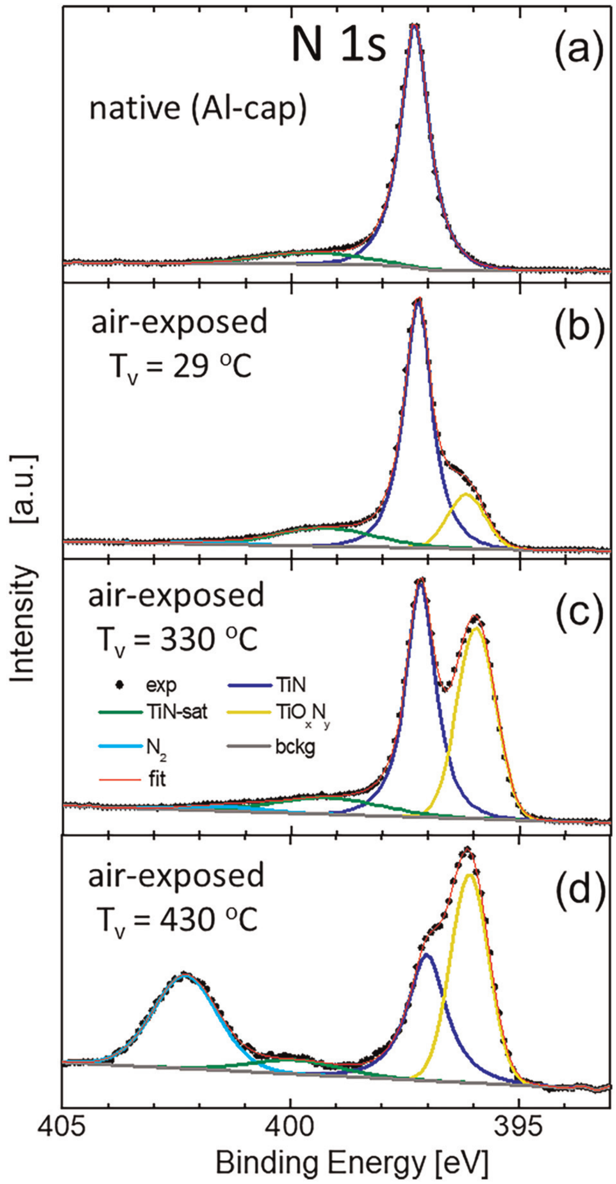

FIG. 19. Set of N 1s spectra obtained from TiN films: (a) *in situ* capped with 1.5-nm-thick Al layer to protect the surface from oxidation, [(b)–(d)] uncapped and exposed to atmosphere at different venting temperatures T_v ranging from 29 to 430 °C. [Reproduced with permission from Greczynski and Hultman, Appl. Surf. Sci. **387**, 294 (2016). Copyright 2016 Elsevier.] Some details of fitting models are modified to account for the recent developments in the charge referencing techniques (cf. Refs. 64, 140, and 141) and to make the treatment more pedagogic.

spectrum of element *B*. Moreover, binding energy values assigned to *A1* and *B1* peaks need to fall in the range typical for A_mB_n bonding. To further increase accuracy, one can even compare the *A1*–*B1* energy interval to the literature values, which cancels out potential errors introduced by improper charge referencing (see Sec. V B). In the case study of TiN oxidation, all peaks in the Ti 2p spectra have their counterparts in the corresponding N 1s and O 1s spectra. For example, the Ti–N component is present in N 1s peak models, the Ti–O$_2$ component in O 1s models, while the TiO$_x$N$_y$ peaks are added to both N 1s and O 1s spectra. The same applies to all core levels including even C 1s, which apart from C—C peaks (with two different carbon hybridizations—sp^2 and sp^3)[205] contains also C—O and O—C═O components. The two latter bonds give rise to the corresponding peak in O 1s spectra.

A fine example of how the criterion of self-consistency plays a critical role is the interpretation of the new peak that appears at 456.6 eV in the Ti 2p spectrum of TiN exposed to air at 330 °C [see Fig. 18(c)]. If the entire analysis was restricted to only Ti 2p spectra, one could easily misinterpret this feature as being due to Ti$_2$O$_3$ formation, which typically results in peaks in this energy range. However, the corresponding N 1s spectrum reveals a strong increase in the intensity of the peak at 396.0 eV assigned to TiO$_x$N$_y$, while no new distinct features are observed in the O 1s spectrum. Thus, the combined evidence from Ti 2p, N 1s, and O 1s spectra evolution allows to exclude Ti$_2$O$_3$ formation.

4. The criterion of quantitative self-consistency across all core-level spectra

The reliability of the peak model can be further enhanced by imposing the condition of quantitative self-consistency on all component peaks of fitted core levels. That is, if peaks *A1* in the spectrum of element *A* and B1 in the core-level spectrum of element *B* are assigned to the A_mB_n compound, the elemental concentrations extracted from *A1* and *B1* peak areas should reflect the compound stoichiometry *m/n*. For example, in the TiN oxidation case, the elemental ratio estimated from the O 1s component assigned to TiO$_2$ and the corresponding peak in Ti 2p spectra is close to 2:1, for all venting temperatures tested.[124]

5. The criterion of self-consistency across multiple data sets

For multiple data sets (e.g., obtained from series of samples or from one sample exposed to various treatment), the peak fitting needs to be consistent across the entire volume of experimental evidence. Peaks assigned to the particular bonding state should maintain the same BE position and shape in all spectra. In the peak models shown in Figs. 18–21, the peak shapes and positions, 2p$_{3/2}$–2p$_{1/2}$ BE splitting and the 2p$_{3/2}$/2p$_{1/2}$ area ratios, and BE difference and area ratios between the primary and satellite peaks (for both Ti 2p and N 1s spectra) are fixed for all specimens in the series up to $T_v = 330$ °C. Parameters to be optimized include the relative area variations between different chemical components present at the surface. In this way, a consistent picture of surface chemistry is obtained. We emphasize that the BE of all component peaks does not vary by more than ±0.2 eV (i.e., it remains within the experimental error) between all samples in the set, which is a good indication that the identification of chemical bonding has been correctly performed.

© Author(s) 2022

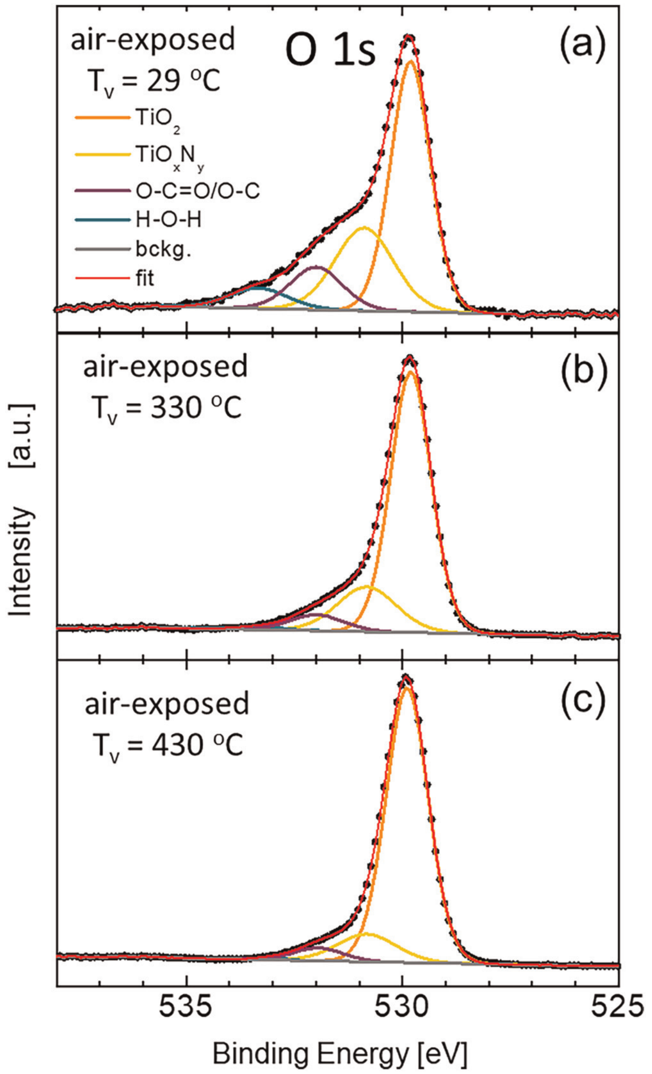

FIG. 20. Set of O 1s spectra obtained from TiN films: [(a)–(c)] uncapped and exposed to atmosphere at different venting temperatures T_v ranging from 29 to 430 °C. [Reproduced with permission from Greczynski and Hultman, Appl. Surf. Sci. **387**, 294 (2016). Copyright 2016 Elsevier.] Some details of fitting models are modified to account for the recent developments in the charge referencing techniques (cf. Refs. 64, 140, and 141) and to make the treatment more pedagogic.

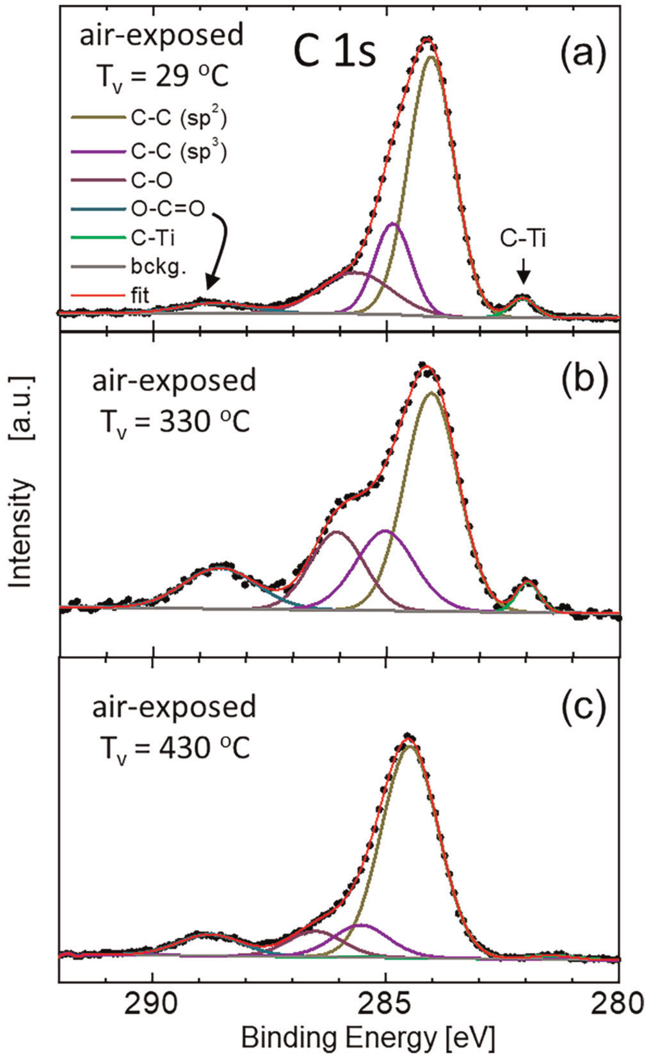

FIG. 21. Set of C 1s spectra obtained from TiN films: [(a)–(c)] uncapped and exposed to atmosphere at different venting temperatures T_v ranging from 29 to 430 °C. [Reproduced with permission from Greczynski and Hultman, Appl. Surf. Sci. **387**, 294 (2016). Copyright 2016 Elsevier.] Some details of fitting models are modified to account for the recent developments in the charge referencing techniques (cf. Refs. 64, 140, and 141) and to make the treatment more pedagogic.

6. The role of underlying physics and chemistry

Peak fitting should account for the underlying physics and chemistry.[206,207] This is done in practice by using constraints, such as fixing the BE splitting and peak-area ratios between spin–split components (see Sec. II E). The FWHM of component peaks in the same spectrum should also be kept under control (e.g., by restricting its variation range in the fitting software) to avoid large variations that are not justified from a physical point of view.

A demonstration for how the use of constraints can facilitate peak fitting is the Mo 3p spectrum recorded from the sputter-etched MoN thin film surface shown in Fig. 6(a). In this case, the stronger metal peak Mo $3p_{3/2}$ overlaps with the N 1s signal, which complicates a reliable estimation of the N concentration. The latter becomes very sensitive to the area under the Mo $3p_{3/2}$ peak. One may, however, exploit the fact that the weaker metal peak, Mo $3p_{1/2}$, does not overlap with any other signals; hence, a well-founded judgement of its area can be made. Then, by constraining the area ratio between the spin–split $3p_{3/2}$ and $3p_{1/2}$ components to 2:1 (to reflect the level occupancy, see Sec. II E), the precise estimate for the area under N 1s peak is obtained resulting in reliable elemental quantification.

© Author(s) 2022

Overfitting should be avoided.[208] The minimization of the fitting parameter cannot be a decisive criterion. The artificial increase in the number of component peaks certainly helps to improve fit quality; however, the result could be fortuitous. Again, there should be an intelligible physical interpretation for each component peak.

D. Quantitative elemental analysis

XPS offers a possibility for the evaluation of the specimen elemental composition. It has to be emphasized though that the sample stoichiometry, as any other information obtained from XPS, is characteristic of the surface region. This should be kept in mind while comparing XPS-derived compositions to the results obtained by other techniques such as RBS, ERDA, or EDX, which have probing depths tens or hundred times larger than that of XPS.[91,92] For the same reason, one should refrain from connecting elemental compositions obtained by XPS to results of other bulk-probing analytical techniques such as x-ray diffraction (crystalline phase composition).

There are numerous reasons for the above reservations. First, the specimen composition within the first 5–10 nm probed by XPS (see Sec. II F) is often different from that in the "bulk." This is because most surfaces are readily oxidized, while exposed to the atmosphere even for a short period of time (for very reactive surfaces, this process takes place also under UHV conditions). In addition to that, a thin layer of the so-called adventitious carbon (AdC) contamination (cf. Sec. V B) builds up with time on all surfaces irrespective of whether samples are stored outside or inside the vacuum system (the chemical composition of AdC layer depends on the storage environment[97] and even the sample material itself).[97] Both the oxide and the AdC layers can be removed by sputter etching with Ar^+ ions (see Sec. III C). We learned above, however, that this treatment introduces several artifacts such as preferential sputtering of lighter atoms,[209,210] which obviously affects the extracted compositions. These serious limitations need to be realized before attempting elemental quantification based on XPS spectra.

Another limitation of XPS quantitative analysis is the detection limit, which in most cases is not better than 0.1–1 at. %. Thus, XPS is certainly not a technique to study materials purity.

The quantification in XPS is based on the areas under the major core-level lines of all elements present in the sample. In the case of signal overlap, it is necessary to first peak-fit the spectrum to get precise estimate of peak areas (see Sec. VI C). For a homogenous sample containing n elements, the molar concentration x_i of element i is expressed as[211]

$$x_i = \frac{A_i/s_i}{\sum_{j=1}^{n} (A_j/s_j)}, \tag{13}$$

where A_i stands for the area under the corresponding core-level peak and s_i is the relative sensitivity factor (RSF). RSFs account for the fact that the number of electrons detected from a given core level of an atom depends on a range of factors that include the excitation source, the photoionization cross section, electron inelastic mean free path, the angle between the incoming x rays and the line connecting the sample with the entrance slit of the analyzer, and the *transmission function* of the spectrometer (i.e., the function describing how efficient electrons with different kinetic energy are transmitted through the instrument).[212,213] RSF varies in a wide range, and the difference between the lowest (Be 1s) and the highest (U $4f_{7/2}$) value can be as large as 150×. The best results are obtained if the RSFs are specifically determined on the same instrument as used for quantification and under the same experimental conditions. If that is not feasible, standard sets of RSFs are also available;[45,46,214] however, a negative impact on the quantification accuracy is to be expected.

The quantification based on Eq. (13) is limited to samples that are homogeneous within the XPS probing depth. In all other cases, knowledge about the depth distribution is required,[215,216] which presents the largest obstacle in practical XPS studies and, if neglected, typically becomes the main source of errors. This is because the signal detected in XPS is an integral of contributions coming from different depths with a depth dependence described by an exponential decay [see Eq. (8) in Sec. III C]. Hence, extremely different element depth distribution functions can produce identical signal intensity.[217] Other types of samples that are difficult (or challenging) for quantitative analysis are those with high surface roughness (in which case the angle between the incoming x rays and the analysis direction cannot be considered constant) as well as crystallographically textured materials including single crystals or epitaxial layers, because of electron diffraction effects.[218,219]

The XPS quantification accuracy is typically claimed to be of the order of ±5%, which is not particularly impressive. Significantly better results can be obtained if standard reference materials are used.[16] Apart from the factors mentioned above, a large source of errors is associated with the correct assessment of peak areas. Two aspects that are of particular importance as they can be directly influenced by XPS practitioner are (i) spectra acquisition procedure and (ii) background subtraction. The former should be performed in a way that ensures that the impact of all potential signal instabilities over time necessary to collect all spectra (often many hours), either related to the instrument operation or to the sample itself, is minimized. For that reason, it is recommended to perform the same number of scans over each core-level signal, irrespective of the signal strength (which can be accounted for by adjusting the dwell time per data point) and set up the acquisition sequence in such way that all BE regions of interest are scanned simultaneously rather than sequentially. In this way, the influence of potential signal instabilities is minimized. It is also critical that all spectra to be included in the quantification are recorded with the identical instrument settings such as pass energy, anode power, and analyzer mode, as each of these can impact signal intensity.

The second factor, i.e., the background selection, is a quite extensive topic in XPS data analysis.[220–224] For quantification, the most important thing to realize is that the choice of background function and the end points directly affects peak areas (and hence the extracted concentrations). The simplest background type is a linear. Although convenient, it lacks theoretical grounds and, importantly, makes the peak area dependent on the arbitrary selection of end points. This type of background function can still be appropriate for wide-bandgap materials, in which case the photoelectron energy losses associated with the presence of valence electrons occur several eV away from the no-loss line. It results in that the background intensity on the low and high BE side of the peak becomes very similar; hence, the error due to the arbitrary selection

© Author(s) 2022

of background end points is reduced. The Shirley background,[225] probably the most common, relies on the assumption that the number of inelastically scattered electrons contributing to the background is directly proportional to the total photoelectron flux. Hence, the background intensity at the binding energy E_B is proportional to the total peak area in the energy range extending from the low binding energy side of the spectrum to E_B. It is noteworthy that the Shirley background was developed to model the background shape of the valence band of Au, so it may not be appropriate to use this background for materials with a bandgap, i.e., semiconductors and insulators. Also in this case, the arbitrary choice of the end point affects the area estimate. This drawback is removed in the treatment proposed by Tougaard,[226,227] which relies on the quantitative description of the inelastic scattering phenomena.

A unique aspect of XPS quantification is that apart from finding the elemental composition the technique allows to determine relative concentrations of a given element present in different chemical states (*chemical composition*). A much-improved accuracy can be obtained in this type of analysis, since only one element type is involved, provided that the chemically shifted spectra components are well separated in energy.

VII. RESULTS PRESENTATION

The final part (and the ultimate goal) of the XPS workflow is the results presentation. Whether in the form of publication in a scientific journal, archive contribution, conference presentation, or as an internal report, results need to be communicated in a clear way such that a reader should have no problem to understand what has been done, make his/her own judgement about the quality of the work, and the reliability of presented conclusions.

An essential part of the results presentation is comprehensive information about experimental conditions. This section should contain information that is sufficient to repeat reported experiments in an independent other laboratory. A complete experimental protocol is suggested in Appendix A. The most crucial information for the interpretation includes (i) the excitation source, (ii) electron emission angle, (iii) whether samples were sputter etched or not, and (iv) whether the charge neutralizer was used. In addition to instrumental details, information about the sample history prior to the XPS analyses should be included, as this often has impact for how to interpret the results. When peak fitting is performed, a complete description of the applied procedure should be added and include the type of peak functions, background type, constraints, etc. More exhaustive lists of relevant experimental details can be found in Refs. 228–230.

Raw XPS data *always* need to be shown, preferably plotted with symbols to make them distinctly different from all curves representing fitted peaks. Avoid presenting (only) spectra after background subtraction as that step removes an essential part of the information due to inelastically scattered electrons. Avoid showing XPS data together with results from other analytical techniques in one figure, as it would make it essentially impossible to see any spectral details.

By an international convention, XPS spectra should be plotted with the binding energy decreasing from left to right to facilitate comparison to already published results. The vertical scale typically features the total count number or counts per second. If multiple spectra of the same core level are shown in the same figure, one should strive to plot them in a way that facilitates comparison so that even small differences can be easily spotted. Depending on the spectra type, several options exist. For example, spectra can be normalized (e.g., to the highest intensity feature in each individual spectrum) and stacked on top of each other (see Figs. 18–21). Alternatively, spectra can be normalized to the intensity of a common peak and plotted in an overlay manner to emphasize intensity change of all other peaks (see Fig. 13).

It is essential while presenting a peak fitted spectra that a reader gets the chance to easily judge the fit quality. For that reason, the fitted curve, which is a sum of the background function and all component peaks, should be shown on top of the raw data (see, e.g., Figs. 18–21). The two can be made easily distinguishable if one uses scatter symbols to plot data points and a solid line to show the fit (preferably in a different color). To make peak model more readable, component peaks corresponding to the same chemical state can be indicated with the same color in all core-level spectra (compare with the Ti 2p, N 1s, O 1s, and C 1 spectra in Figs. 18–21).

VIII. APPLICATION EXAMPLES

A. Oxide thickness estimate

Strohmeier[231] proposed a useful approach for a non-destructive estimation of the thickness of thin ($\lesssim$10 nm) continuous overlayers such as native oxides. The method relies on several assumptions featuring (i) x-ray reflection and refraction are negligibly small, (ii) attenuation of the x rays in the layers involved can be neglected, (iii) there is no angular anisotropy of emitted electrons (e.g., due to sample being highly oriented crystalline solid), and (iv) the layers are homogenous, continuous, and flat.[12] Within this treatment, the thickness t of a uniform oxide layer grown on top of a film can be derived from the intensity ratio of oxide and film peaks I_o/I_f measured with the electron emission angle θ,[232]

$$t = L_o \cos\theta \, \ln\left(\frac{N_f L_f}{N_o L_o}\frac{I_o}{I_f} + 1\right), \tag{14}$$

in which L_f and L_o are electron effective attenuation lengths (or inelastic mean free paths in the absence of elastic scattering effects, see Sec. II F) in film and in the oxide layer, N_o and N_f are volume atom densities in the oxide and film, respectively. As the oxide peak is typically shifted from that of the film only by a few eV one may in the first approximation assume that the electron mean free paths in film and the oxide layer are the same, i.e., $L_f = L_o = L$. Equation (14) is then simplified to

$$t = L \cos\theta \, \ln\left(\frac{N_f}{N_o}\frac{I_o}{I_f} + 1\right). \tag{15}$$

While N_f can be accurately known (the phase identification and lattice parameter are obtained by XRD in the case of crystalline materials), for reasonable estimate of N_o one has to identify the oxide type. Often this information can be successfully obtained from XPS by constructing a self-consistent peak model

© Author(s) 2022

(see Secs. VI C 3 and VI C 4), which allows to obtain the elemental composition of the oxide layer and binding energy of oxide peaks.

As an example, we apply Eq. (15) to estimate the thickness of the native oxide layer that forms on the ZrB_2 film upon air exposure. Figure 22 shows a set of Zr 3d/B 1s spectra from samples stored in air for time periods between 20 min and 1 year (see Sec. VI C 1 for a detailed discussion of spectral peaks). The oxide peaks are initially low and grow with an increasing exposure time to dominate the spectra for exposure times exceeding two weeks. By performing a peak fitting as described in Sec. VI C 1 and shown in Fig. 17, one can separate oxide and boride contributions in all spectra to obtain the intensity ratios between Zr—O and Zr—B peaks that are necessary input to estimate the oxide thickness. To keep this treatment on a simple level we assume that the oxide layer has a monoclinic crystal structure due to low temperatures involved, the volume density of Zr atoms is $2.73 \times 10^{22}\,\text{cm}^{-3}$. As the volume density of Zr atoms in hexagonal-structure ZrB_2 is $3.22 \times 10^{22}\,\text{cm}^{-3}$, the $\frac{N_f}{N_o}$ term in Eq. (15) is 1.18. Further neglecting elastic scattering effects (i.e., $L = \lambda$) and considering that the electron mean free path for Zr 3d electrons is the same in both layers: $\lambda_{\text{oxide}} = \lambda_{\text{ZrB}_2} = 2.3$ nm (for Al K_α x rays),[71] and for normal electron emission we can simplify Eq. (15) to

$$t_{\text{oxide}}\ [\text{nm}] = 2.3\ \ln\left(1.18\frac{I_{\text{Zr}-\text{O}}}{I_{\text{Zr}-\text{B}}} + 1\right). \qquad (16)$$

By using the $I_{\text{Zr}-\text{O}}/I_{\text{Zr}-\text{B}}$ ratios extracted from peak-fitted Zr 3d/B 1s spectra, one can, thus, generate the plot of oxide thickness t_{oxide} vs air exposure time, as shown in Fig. 23. In this case, the oxide thickness increases linearly with the logarithm of the exposure time with a rate of 0.57 nm/decade.

The advantage of the method described above is that signals from the same element present in two different chemical states are analyzed, which eliminates the uncertainty related to the determination of photoionization cross sections. In addition, the errors due to instrumental factors like a transmission function of the spectrometer are not of a concern, since electrons excited from metal and oxide core levels have a similar kinetic energy.

B. TiN/HfN bilayers—estimates of electron effective attenuation lengths

In Sec. VI A, we discussed the influence of electron inelastic scattering on the background shape for a set of survey spectra recorded from TiN/HfN bilayers with varying thickness of the top TiN layer (see also Fig. 16). Here, we consider core-level spectra from these samples to illustrate how one can (a) extract information about the electron effective attenuation length L (cf. Sec. II F) in the top layer if the layer thickness is known or (b) estimate the thickness of the top layer if L is known. Before going into details, we note that the method works well for layers that grow in an atomic layer-by-layer manner; hence, higher surface roughness and/or island growth are two factors that prevent reliable estimates. Epitaxial layers exhibiting step-flow growth should preferably be analyzed with the x-ray beam and detection angle projected along the atomic ledges to minimize shadowing effects. Moreover, several assumptions listed in the beginning of Sec. VIII A apply also in this case.[12]

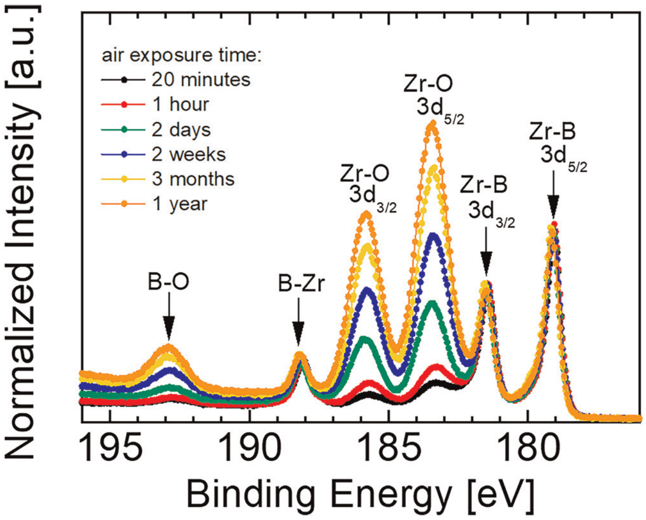

FIG. 22. Set of Zr 3d/B 1s spectra obtained from samples stored in air for a time period ranging from 20 min to 1 year. The oxide peaks are initially low and grow with an increasing air exposure time to dominate the spectra for storage times exceeding two weeks.

Let us consider the sets of Ti 2p and Hf 4f spectra shown in Figs. 24(a) and 24(b), respectively. The TiN thickness t_{TiN}varies from 0 to 42.7 nm. All spectra are acquired from samples in the as-received state, e.g., with native surface oxides resulting from an ~10 min air exposure, necessary for transfer from the growth

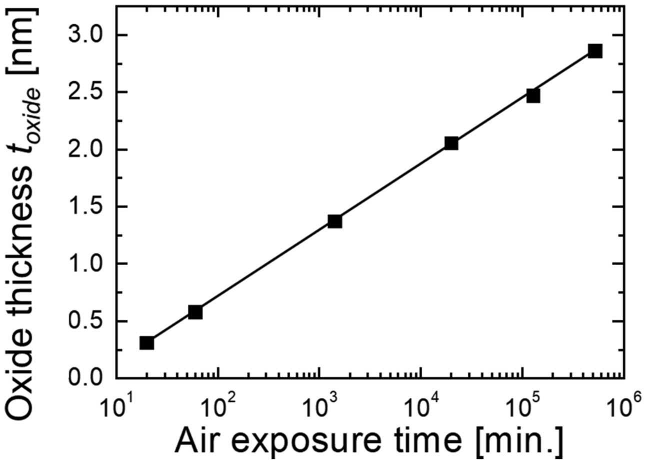

FIG. 23. Thickness of the surface oxide t_{oxide} growing on top of the ZrB_2 film exposed to atmosphere plotted as a function of air exposure time. t_{oxide} estimates are obtained using Eq. (16) and input from peak-fitted Zr 3d/B 1s spectra shown in Fig. 22. In this case, the oxide thickness increases linearly with the logarithm of the exposure time with a rate of 0.57 nm/decade.

© Author(s) 2022

chamber to the load lock entry chamber of XPS instrument. For the lowest TiN thickness $t_{\mathrm{TiN}} = 0.7$ nm, the Ti $2p_{3/2}$ spectrum is composed of two peaks at 457.0 and 458.4 eV, assigned to $\mathrm{TiO_xN_y}$ and $\mathrm{TiO_2}$, respectively (cf. Sec. VI C 1). Hence, in this case, the entire TiN layer is oxidized. The first indication of the TiN contribution at 455.0 eV is detected for the sample with $t_{\mathrm{TiN}} = 1.3$ nm. The latter component grows with increasing TiN thickness up to $t_{\mathrm{TiN}} = 5.3$ nm at which point it saturates, indicating that the overlayer thickness approaches the probing depth (see Sec. II F). Further increase in the TiN thickness does not cause any substantial changes to the Ti 2p spectra. This type of signal evolution provides evidence for layer-over-layer growth of TiN on the HfN substrate as opposite to island growth. In the latter case, the thickness of individual islands may be larger than the native oxide thickness even for the lowest nominal coverage resulting in that the signal component due to the non-oxidized species appears in all spectra irrespective of the amount of deposited material.

The Hf 4f spectra shown in Fig. 24(b) contain information that is complementary to that provided by Ti 2p spectra. For the reference HfN film ($t_{\mathrm{TiN}} = 0$ nm) apart from the spin–split doublet due to HfN with $4f_{7/2}$ and $4f_{5/2}$ peaks at 15.9 and 17.5 eV, respectively, there is evidence for a second pair of peaks at 16.7 and 18.4 eV, assigned to $\mathrm{HfO_x}$. The latter peaks disappear even for the lowest TiN coverage, $t_{\mathrm{TiN}} = 0.7$ nm, indicating that the deposited TiN distributes uniformly over the HfN surface (as opposite to the island growth), in very good agreement with the corresponding Ti 2p spectrum, which shows an oxidized overlayer. Further increase in the TiN thickness leads to gradual decay of the Hf 4f signal intensity with no change in peak positions. The latter effect is caused by inelastic scattering of Hf 4f electrons in the TiN overlayer and can be used to estimate the electron effective attenuation length in TiN. It is trivial to show that for the exponential signal decay of the type described by Eq. (8) (see Sec. III C), the signal intensity I_o from the TiN overlayer of thickness t_{TiN} is given by

$$I_o(t_{\mathrm{TiN}}) = I_o^0[1 - \exp(-t_{\mathrm{TiN}}/L_o(E_{\mathrm{kin}})\cos\theta)], \tag{17}$$

in which I_o^0 is the signal intensity from an infinitely thick TiN layer (or in more practical terms: from the TiN film with thickness significantly exceeding the XPS probing depth), $L_o(E_{\mathrm{kin}})$ is the effective attenuation length in the TiN overlayer for electrons with kinetic energy E_{kin} originating from TiN (such as Ti 2p), and θ is the electron emission angle from the surface normal. In a similar manner, the signal intensity I_f from the HfN film uniformly covered by the TiN layer with a thickness t_{TiN} is given by

$$I_f(t_{\mathrm{TiN}}) = I_f^0\exp(-t_{\mathrm{TiN}}/L_f(E_{\mathrm{kin}})\cos\theta), \tag{18}$$

in which I_f^0 is the signal intensity from an infinitely thick HfN layer and $L_f(E_{\mathrm{kin}})$ is the effective attenuation length in the TiN overlayer for electrons with kinetic energy E_{kin} originating from HfN (such as Hf 4f).

Equations (17) and (18) can be modified to

$$\ln\left(1 - \frac{I_o(t_{\mathrm{TiN}})}{I_o^0}\right) = -t_{\mathrm{TiN}}/L_o(E_{\mathrm{kin}})\cos\theta \tag{19}$$

and

$$\ln\left(\frac{I_f(t_{\mathrm{TiN}})}{I_f^0}\right) = -t_{\mathrm{TiN}}/L_f(E_{\mathrm{kin}})\cos\theta. \tag{20}$$

The left sides of Eqs. (19) and (20) can be then plotted against t_{TiN} to estimate both $L_o(E_{\mathrm{kin}})$ and $L_f(E_{\mathrm{kin}})$ from the slopes. This is shown in Fig. 25 for the case of Ti 2p and Hf 4f electrons with $E_{\mathrm{kin}} = 1030$ and 1470 eV, respectively. In this case, electrons are emitted along the surface normal, hence $\cos\theta = 1$. Data points are reasonably well fitted with lines, which indicates that the TiN growth on the HfN surface proceeds in a continuous layer-over-layer manner. This is certainly not always the case for bilayers and multilayers of a given set of compounds.[12] Depending on the specific growth conditions, anything from local epitaxial growth to an island formation (and coalescence)

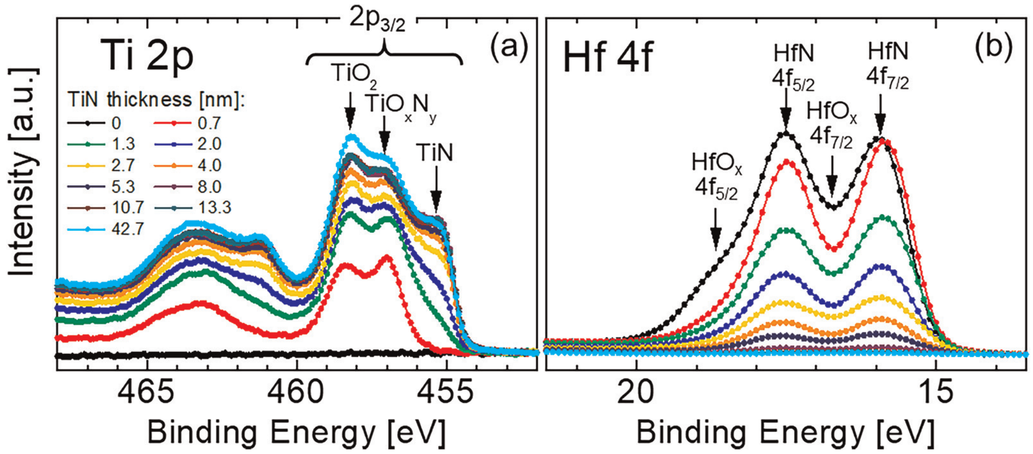

FIG. 24. Two sets of (a) Ti 2p and (b) Hf 4f core-level spectra recorded from TiN/HfN bi-layer samples with varying thickness of the top TiN layer (from 0 to 42.7 nm).

can be observed.[120] This obviously sets limits for the applicability of the method described above for reliable estimates of L. One can, however, turn the problem around and use the plot like the one shown in Fig. 25 as evidence for a specific growth type.

The attenuation lengths for Ti 2p and Hf 4f electrons in TiN, $L_{\text{TiN}}(E_{\text{kin}} = 1030\text{ eV})$ and $L_{\text{TiN}}(E_{\text{kin}} = 1470\text{ eV})$ estimated from the slopes of plots in Fig. 25 are 1.7 and 2.3 nm, respectively. They reflect the classical trend of L increasing with increasing electron energy (the so-called "universal curve," see Sec. II F) and, in fact, are very close to IMFP values calculated for Ti, which are 1.8 and 2.4 nm.[71] The latter indicates that under present experimental conditions elastic scattering effects are negligible (and, hence, $L = \lambda$).[71] The above estimates are also fully consistent with the evolution of Ti 2p spectra discussed above: a saturation of the TiN peak at 455.0 eV is first observed for $t_{\text{TiN}} = 5.3$ nm, which is only slightly larger than the probing depth for Ti 2p electrons, $3 \times t_{\text{TiN}} = 5.1$ nm.

Equations (19) and (20) can be further simplified if $L_o = L_f$, which is, for example, the case for electrons from the same core-level signal present in the surface oxide and in the film (see Sec. VIII A). Under such circumstances, the overlayer thickness t_o is obtained by combining Eqs. (19) and (20) into

$$t_o = L(E_{\text{kin}}) \cos\theta \ln\left(\frac{I_o}{I_f}\frac{I_f^0}{I_o^0} + 1\right), \tag{21}$$

which is equivalent to Eq. (14) (see Sec. VIII A) and sometimes referred to as the Hill equation.[197]

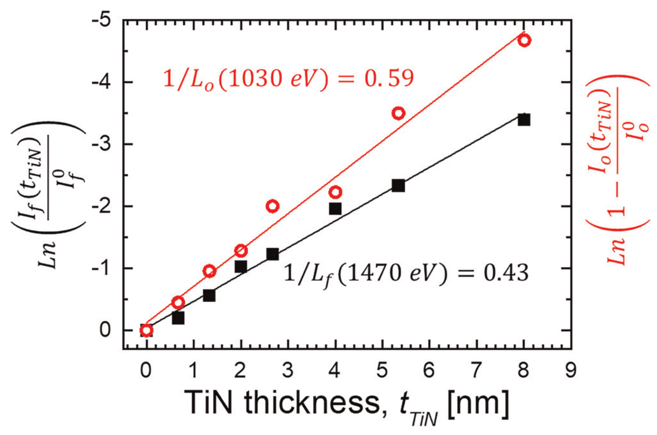

FIG. 25. Plots used to extract the electron effective attenuation length based on Ti 2p and Hf 4f spectra from TiN/HfN bi-layer that are shown in Fig. 24. By plotting the left sides of Eqs. (19) (red) and (20) (black) against the thickness of the top TiN layer t_{TiN}, one can estimate the effective attenuation lengths in the TiN overlayer $L_o(E_{\text{kin}})$ and $L_f(E_{\text{kin}})$ for electrons with kinetic energy E_{kin} originating from TiN (in this example Ti 2p electrons) and HfN (in this example Hf 4f electrons), respectively. Data points are reasonably well fitted with lines, which indicates that the TiN growth on the HfN surface proceeds in a layer-over-layer manner. $L_f > L_o$ since Hf 4f electrons have larger E_{kin} than Ti 2p electrons.

Equation (21) can be, for example, used to determine oxide thickness by recording spectra at several electron emission angles (by tilting the sample—cf. Sec. V E and Fig. 13) and plotting $\ln\left(\frac{I_o}{I_f}\frac{I_f^0}{I_o^0} + 1\right)$ as a function of $1/\cos\theta$. The slope, t_o/L gives the estimate for the oxide thickness.

C. TiAlN oxidation—Example of depth profiles

XPS is particularly useful in studies of surface oxidation. If the oxide thickness exceeds the XPS probing depth, one can still analyze chemical modifications in the surface region by means of sputter depth profiles.[233] During such experiments, the topmost layers are removed in a step-by-step manner and spectra of all major core levels are recorded after each sputtering sequence to reveal changes in the elemental and chemical composition as a function of depth. In all such studies, it is assumed that the detrimental effects of the Ar^+ ion etch (see Sec. III C) are negligible in comparison to those introduced by the treatment to be studied (in the example below—oxidation resulting from high temperature anneal in air).

Figures 26(a)–26(d) show four sets of Ti 2p, Al 2p, N 1s, and O 1s spectra recorded from polycrystalline NaCl-structure $\text{Ti}_{0.75}\text{Al}_{0.25}\text{N}$ thin film sample previously annealed for 1 h at 700 °C in air.[234,235] Layers were grown by a hybrid high-power impulse and dc magnetron sputtering (HiPIMS/DCMS) with metal-ion-synchronized substrate bias.[236] Detailed understanding of high-temperature oxidation processes is of intense scientific and technological interest with applications including wear-resistant coatings on high-speed cutting tools.[237,238]

The Ti 2p spectra acquired for depths $d \lesssim 25$ nm are characterized by low signal intensity indicating that the surface is depleted of Ti. The spectra show broader peaks at lower BE (with $2p_{3/2}$ components in the region 454–457 eV) that are assigned to reduced (lower oxidation state) oxide from the top layers that forms as the result of exposure to the Ar^+ beam. In addition, spectra contain characteristic TiO_2 contribution with the $2p_{3/2}$ component at 459.4 eV originating from the sample region situated deep enough to be unaffected by the Ar^+ ion etch.[239] The Ti 2p signal intensity increases with increasing d, up to $d \sim 100$ nm at which point spectra change abruptly and become identical to that acquired from the reference $\text{Ti}_{0.75}\text{Al}_{0.25}\text{N}$ film, revealing that for $d > 120$ nm, the original film is intact. Complementary information is provided by the Al 2p spectra [see Fig. 26(b)]. For $d \leq 25$ nm, the Al 2p peak is present at 75.5 ± 0.2 eV, which is characteristic of Al_2O_3, while for $d \geq 120$ nm, the peak position changes to 74.1 eV, identical to that of Al in $\text{Ti}_{0.75}\text{Al}_{0.25}\text{N}$ reference sample, consistent with the changes in the Ti 2p spectra. Importantly, the Al peak is not detected for $40 \leq d \leq 80$ nm, revealing an Al-depleted TiO_2 layer just below the top Al_2O_3 layer.[240] The changes in N 1s spectra [cf. Fig. 26(c)] agree with the information extracted from Ti 2p and Al 2p signals. For $d \lesssim 80$ nm, e.g., in the $\text{Al}_2\text{O}_3/\text{TiO}_2$ double-oxide layer, the N 1s signal is literally absent, while for $d \gtrsim 100$ nm, N 1s spectra are dominated by the peak at 397.1 eV, corresponding to N atoms in $\text{Ti}_{0.75}\text{Al}_{0.25}\text{N}$. The small peak at ∼404 eV at depths exceeding 100 nm is a signature of N–N bonding, which can be assigned to interstitial N, which bonds to N in the lattice or to the formation of N_2.[241,242]

© Author(s) 2022

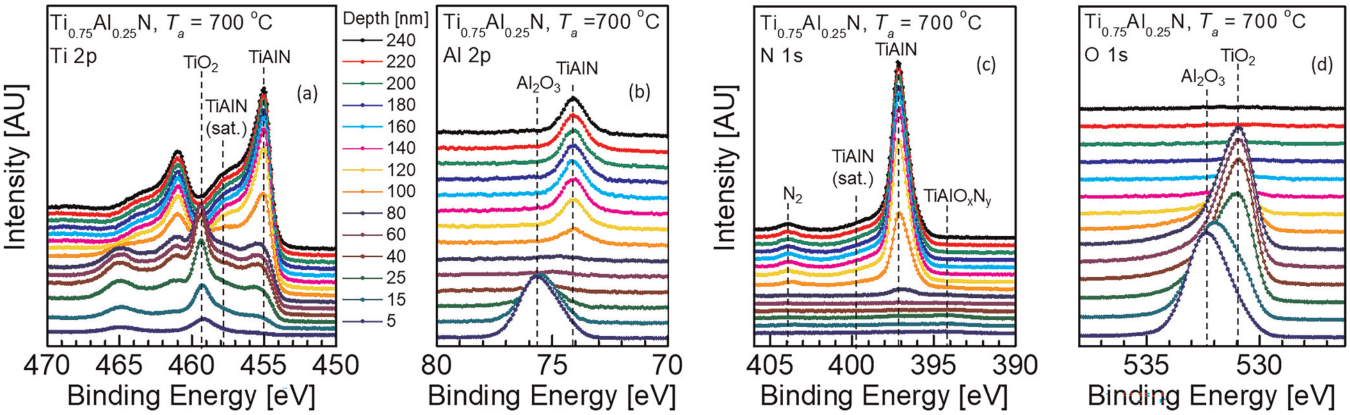

FIG. 26. Four sets of (a) Ti 2p, (b) Al 2p, (c) N 1s, and (d) O 1s spectra recorded during depth profiles through polycrystalline NaCl-structure $Ti_{0.75}Al_{0.25}N$ thin film samples previously annealed for 1 h at 700 °C in air. The bottom-most spectra are recorded closest to the surface. [Reproduced with permission from Greczynski *et al.*, Surf. Coat. Technol. **374**, 923 (2019). Copyright 2019 Elsevier.]

The picture of surface chemistry cannot be complete without O 1s spectra [see Fig. 26(d)]. At the very surface, $d \lesssim 15$ nm, the spectra are dominated by a high-energy component at 532.4 eV corresponding to O in Al_2O_3. The lower BE component at 531.0 eV due to O in TiO_2 becomes more intense with increasing sputter depth, and eventually for $d \geq 25$ nm, it dominates the O 1s spectra. This evolution is fully consistent with changes observed in Ti 2p, Al 2p, and N 1s spectra. The O 1s peak is absent at depths exceeding 140 nm, which provides an effective estimate of the oxidation depth.

Areas under Ti 2p, Al 2p, N 1s, and O 1s spectra recorded as a function of depth can be used to plot elemental distributions as shown in Fig. 27. The metal segregation is a result of Al diffusion to the surface, where it reacts with oxygen to form Al_2O_3, while at larger depths an Al-deficient TiO_2 layer forms after $Ti_{0.75}Al_{0.25}N$ decomposition. The double oxide layer consists of 20 nm Al_2O_3 and 80 nm of TiO_2. More details can be found in Ref. 234.

Important to keep in mind while interpreting depth profiles of the type shown in Fig. 27 is that transitions between all layers appear smoothened out. This is for two reasons. First, an intermixing takes place due to Ar^+ bombardment. This effect can be minimized by using low Ar^+ energy and shallow incidence angle (for 500 eV ions incident at the angle of 20° from the surface the thickness of the intermixed layer is of the order of ∼1 nm).[234] The XPS probing depth, which under conditions of that experiment was in the range of 5–8 nm, is the second (and stronger!) factor responsible for the apparent smoothening of elemental depth profiles.[116] Thus, the actual transitions between all layers are significantly sharper than what is shown in Fig. 27.

The conversion of sputter time into depth units requires calibration of the etch rate that can be performed either by sputtering through a thinner reference sample of the same type or by measuring oxide thickness by other methods like cross-sectional SEM.

D. Depth profiling on $Hf_{0.78}Al_{0.10}Si_{0.12}N$/$Hf_{0.78}Al_{0.14}Si_{0.08}N$ multilayers

This application example illustrates the unique capability of XPS to resolve research questions concerning the nature of nanoscale multilayers that are impossible to answer by other techniques. Figure 28(a) shows a bright field cross-sectional transmission electron microscopy (XTEM) image together with corresponding selected area electron diffraction pattern recorded from a polycrystalline $Hf_{0.78}Al_{0.10}Si_{0.12}N/Hf_{0.78}Al_{0.14}Si_{0.08}N$ multilayer thin film sample with a periodicity of 10 nm.[243] The multilayers were obtained by sequentially switching the incident ion energy between 10 and 40 eV (controlled with the substrate bias potential). The image reveals a clear contrast between the layers, which can be caused by differences in layer elemental and phase composition. XPS was performed to determine whether the chemical bonding varies between layers that have different contrast in XTEM.

The multilayer period of only 10 nm is challenging for XPS. In order to enhance the depth resolution, Zalar rotation was employed.[244,245] The latter means that the sample was rotated during Ar^+ etch, which is beneficial in the case of polycrystalline samples as the material is removed more uniformly. The Ar^+ beam raster size was $3 \times 3\ mm^2$ and the size of the analyzed circle area is 110 μm centered in the middle of the erosion crater.

Figure 28(b) shows the Si 2p spectra recorded in the middle of the layers that give different contrast in XTEM. Both spectra are composed of two peaks revealing that Si is present in two chemical states, namely, Si—Si/Si—Hf (∼99.1 eV) and Si—N (∼101.8 eV).[47] The ratio between the two peaks varies, however, between the layers. The former component dominates when the lower ion energy of 10 eV was used during film growth, while the latter is stronger in spectra recorded from layers grown with 40 eV ion irradiation. The electron microscopy and diffraction results obtained from 10 eV layers (grown separately with larger thickness) indicate that the films

© Author(s) 2022

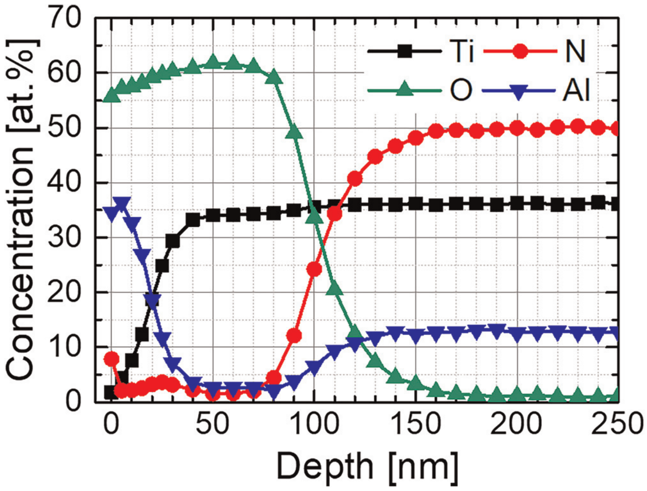

FIG. 27. XPS elemental concentration depth profiles for polycrystalline NaCl-structure $Ti_{0.75}Al_{0.25}N$ thin film samples previously annealed for 1 h at 700 °C in air. [Reproduced with permission from Greczynski *et al.*, Surf. Coat. Technol. **374**, 923 (2019). Copyright 2019 Elsevier.]

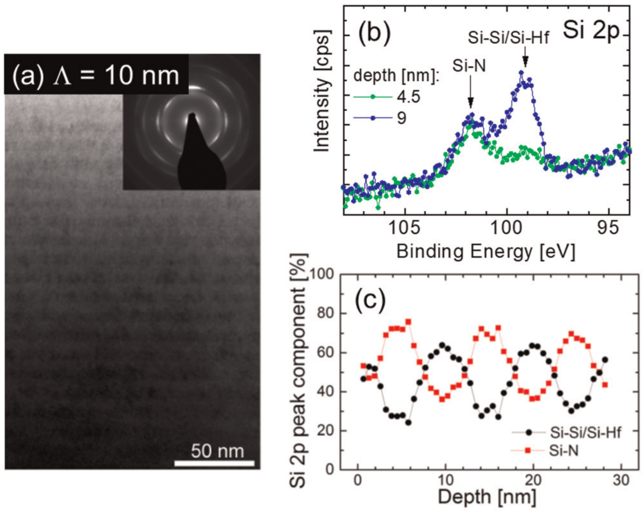

FIG. 28. (a) Bright field cross-sectional transmission electron microscopy (XTEM) image together with the corresponding selected area electron diffraction pattern recorded from a polycrystalline $Hf_{0.78}Al_{0.10}Si_{0.12}N/Hf_{0.78}Al_{0.14}Si_{0.08}N$ multilayer thin film sample with a periodicity of 10 nm, (b) Si 2p spectra recorded in the middle of the layers that give a different contrast in XTEM images. Both spectra are composed of two peaks revealing that Si is present in two chemical states, namely, Si—Si/Si—Hf (~99.1 eV) and Si—N (~101.8 eV). The ratio between the two peaks varies between the layers and (c) the intensities of Si—N and Si—Si/Si—Hf Si 2p peaks plotted as a function of depth during sputter-depth profiling with Zalar rotation. The periodic change in the chemical state of Si atoms matches the multilayer period very well. [Reproduced with permission from Fager *et al.*, J. Vac. Sci. Technol. A **33**, 05E103 (2015). Copyright 2015 AVS.]

are nanocomposites, consisting of $\lesssim$5 nm NaCl-structure HfAlSiN nanograins encapsulated by a disordered tissue phase. Si is incorporated in both the crystalline and the amorphous phases, with the dominance of the latter one; thus, the corresponding Si 2p spectrum possesses two peaks: a Si—N peak due to Si inside of the nanograins and a more-intense Si—Si/Si—Hf peak from Si in the disordered regions. As the ion energy during growth increases to 40 eV, the disordered regions are eliminated and the nanograins extend along the growth direction forming nanocolumns. In consequence, the Si 2p spectrum becomes dominated by the high binding energy component due to Si—N.

In Fig. 28(c), the intensities of both the Si—N and Si—Si/Si—Hf Si 2p peaks are plotted as a function of depth for a multilayered sample. The periodic change in the chemical state of Si atoms matches the multilayer period very well.

E. Spatial imaging of sputter-etched Cr/Ti multilayer sample

A very fascinating (and useful!) feature of modern XPS instruments is the imaging spectroscopy, i.e., a possibility to acquire an image that reflects the lateral distribution of elements, or even the chemical states they are in.[246] This can be realized in several ways, e.g., by using a focused x-ray beam that is scanned over the sample surface, by limiting the area from which the signal is acquired, or by application of an array of detectors with imaging optics.[247,248] Depending on the solution, the ultimate lateral resolution varies from 1 to 7.5 μm.[249,250] As we discuss below, imaging is also very useful to get more insight into the sputter depth profiles of the type discussed in two previous application examples. We consider here an image of the sputtering crater acquired after etching through the Ti(30 nm)/Cr(18 nm) multilayer stack (see Fig. 29). The Ar^+ ion energy was intentionally low at 500 eV to minimize interface mixing and the ion beam was incident at an angle of 70° from the surface normal and rastered over an area of 2×2 mm^2. The experiment was stopped after reaching a depth of 300 nm corresponding to ~6 Ti + Cr interlayer periods. The image shown in Fig. 29 shows the intensity distribution of the Ti 2p signal over the 4×4 mm^2 area. The intensity map is composed of 100 smaller images (each 400×400 μm^2 in size) each of which was acquired by the *spherical mirror analyzer* (SMA) specially designed to obtain spatially resolved images.[251,252] All dark circles correspond to the Cr-rich regions. It is important to realize that while the lateral distance from the left side of the image to the center is 2 mm, the depth difference is only ~230 nm (ca. 4.5 multilayer periods from the left side of the image to the center), corresponding to the slope of the crater edge of only 0.0067°. A broader Cr ring closer to the center indicates that the crater slope decreases further in the vicinity of the analysis spot located at the center of the crater and is $\lesssim$0.0012°. This means that the thickness variation over the 110 μm analysis spot is less than 1.1 nm. To further illustrate this point, a schematic drawing is added in Fig. 30. The corresponding sputter depth profile shown in the same figure reveals that the interface width increases with increasing sputter depth, which is typically the case. At early stages, the 80/20 width is 4.5 nm and is limited by the XPS probing depth.

F. *Ex situ* studies of native target chemistry during reactive dc magnetron sputtering

The essential advantage of XPS is that the sample form is rarely a limiting factor preventing analysis. To illustrate that point, we discuss here the changes in the surface chemistry of Ti target resulting from its use in the magnetron sputtering process conducted in Ar/N_2 atmosphere.[253,254] In the vast majority of cases, the focus is on the analysis of deposited thin film layers; however, the presence of a reactive gas leads not only to the desired compound formation at the substrate, but also to gas chemisorption at the target and subsequent growth of compound layer, by the so-called target poisoning.[255,256]

For these experiments, a $2 \times 4\,\text{cm}^2$ section of the target, positioned in the middle and across the race track, was made detachable to allow for transfer to XPS system.[253] To avoid air exposure, the target was capped immediately after sputtering with a few-nm-thick Al overlayer; hence, information about the chemical state of target elements as a function of N_2 partial pressure p_{N2} is preserved.[66] The total gas pressure was kept constant at 0.4 Pa (3 mTorr), while the N_2 partial pressure p_{N2} was varied from 0 to 200 mPa. Prior to each experiment, the target was conditioned for 5 min in pure Ar behind closed shutters to reset the target history. For each gas mixture studied, the target was operated for 10 min to assure steady-state conditions.

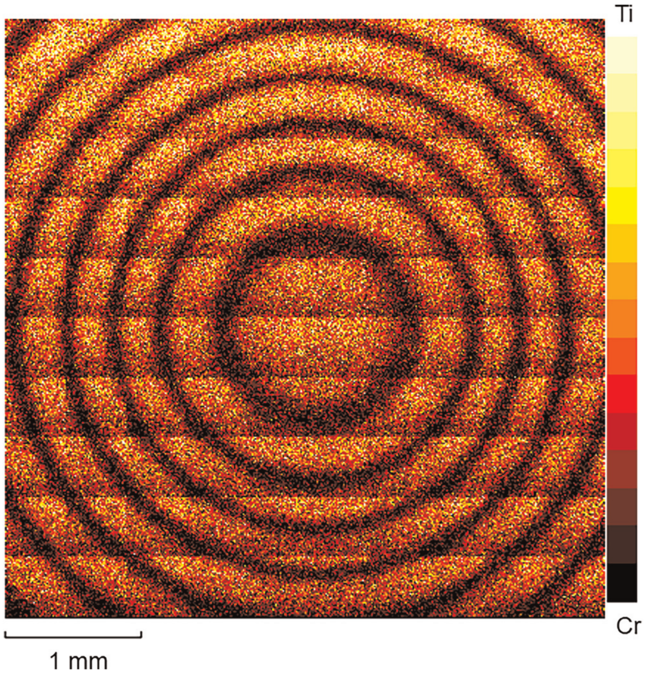

FIG. 29. A stitched XPS image of the sputtering crater acquired after etching through the Ti(30 nm)/Cr(18 nm) multilayer sample. Image shows the intensity distribution of the Ti 2p signal over the $4 \times 4\,\text{mm}^2$ area. All dark circles correspond to the Cr-rich regions. The intensity map is composed of 100 smaller images (each $400 \times 400\,\mu\text{m}^2$ in size). Ar^+ ion energy was intentionally low at 500 eV to minimize the interface mixing, the ion beam was incident at an angle of 70° from the surface normal and rastered over an area of $2 \times 2\,\text{mm}^2$.

A set of Ti 2p spectra recorded from Al-capped Ti targets sputtered in Ar/N_2 mixture with the N_2 partial pressure varying from 0 to 200 mPa is shown in Fig. 31(a). Sputtering in pure Ar gas results in that the Ti 2p signal is characteristic of metallic Ti, with the Ti $2p_{3/2}$ peak at 454.0 eV and the overall shape very similar to the reference Ti 2p spectra from metallic Ti films shown in Fig. 31(b). With increasing N_2 partial pressure to 9 mPa, the Ti $2p_{3/2}$ peak moves to 454.2 eV and broadens on the higher BE side, which indicates the presence of a new contribution. The latter component, assigned to TiN_x, is more pronounced after sputtering at $p_{N2} = 27$ mPa. In this case, the BE of the TiN_x feature, 454.60 eV, is between that of a metal and a stoichiometric nitride (455.0 eV). For $p_{N2} = 45$ mPa, the TiN_x peak shifts to 454.9 eV and, hence, it becomes better resolved from the metallic component at 454.0 eV. With $p_{N2} \geq 92$ mPa, the spectra are dominated by a Ti $2p_{3/2}$ peak at 455.0 eV, characteristic of a stoichiometric TiN, in addition to a minor component at 454.0 eV due to metallic Ti.

The precise fractions of respective Ti and TiN contributions to the Ti 2p spectra from Al-capped targets for cases where stoichiometric TiN layers are formed (targets operated with $p_{N2} \geq 92$ mPa), can be obtained by advanced peak modeling, in which the input from spectra recorded from reference Ti and TiN films shown in Figs. 31(b) and 31(c) is used (for the detailed discussion of the latter case, see also Sec. VI C 1). The parameters obtained from fitting the reference samples include (i) line shapes for pairs of Ti, TiN, and TiN-sat peaks, (ii) $2p_{3/2}$–$2p_{1/2}$ energy splitting, (iii) the $2p_{3/2}/2p_{1/2}$ area ratios, and (iv) the BE difference between TiN and TiN-sat peaks. The fitting parameters include full-width-at-half-maximum, $2p_{3/2}$ peak positions, and intensities. With this restrictive modeling, satisfactory fits of the Ti 2p spectra from Al-capped targets can be obtained as demonstrated in Fig. 31(d) for the case of $p_{N2} = 92$ mPa.

Once the relative Ti and TiN contributions to the Ti 2p spectra are precisely determined, one can use the type of analysis presented in Sec. VIII A to estimate the thickness of the nitride layer covering the Ti target. The volume Ti atom density ratio N_{Ti}/N_{TiN} is 1.46 for hexagonal close-packed Ti and cubic TiN. Assuming $\lambda_{Ti} = \lambda_{TiN} = 1.8$ nm for Ti 2p electrons in Ti excited with Al K_α x rays,[71] the TiN thickness varies from 2.9 nm with $p_{N2} = 92$ mPa to 3.4 nm with $p_{N2} = 200$ mPa. These numbers agree very well with the output from a dynamic Monte-Carlo collisional computer simulation using TRIDYN code,[257,258] which estimates the nitride layer thickness at 3.2 nm.[253]

IX. CONCLUDING ADVISES

- Learn the basics of the XPS technique *before* bringing samples for analysis and attempting spectra acquisition. This saves much time and leads to a more convincing result. It is essential to understand what actually happens in the time period between the “start acquisition” button is pressed, and the final spectrum comes out of the instrument (Sec. II);

© Author(s) 2022

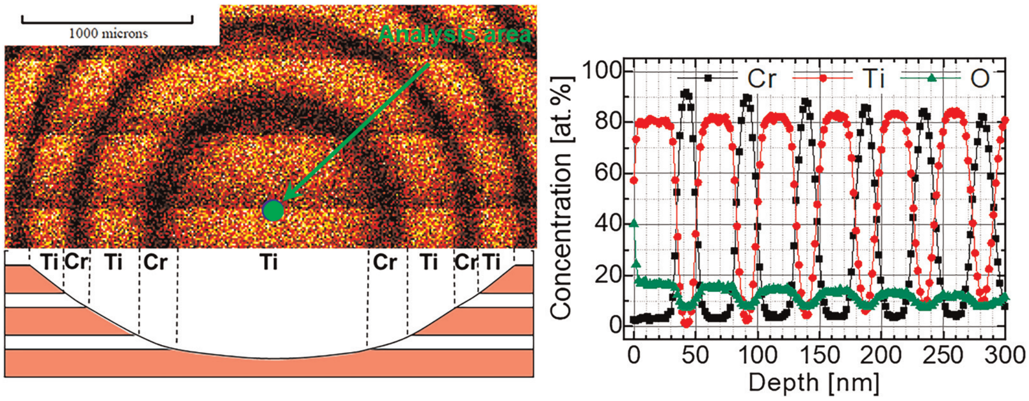

FIG. 30. A closer look at the XPS image shown in Fig. 29. While the lateral distance from the left side of the image to the center is 2 mm, the depth difference is only ∼230 nm, which gives the slope of the crater edge of only 0.0067°. The crater slope further decreases to $\lesssim$0.0012° at the center of the crater as revealed by broadened Cr ring. This means that the thickness variation over the 110 μm analysis spot (indicated as green circle) is less than 1.1 nm. The corresponding sputter depth profile shown to the right reveals that the interface width increases with increasing sputter depth, which is typically the case.

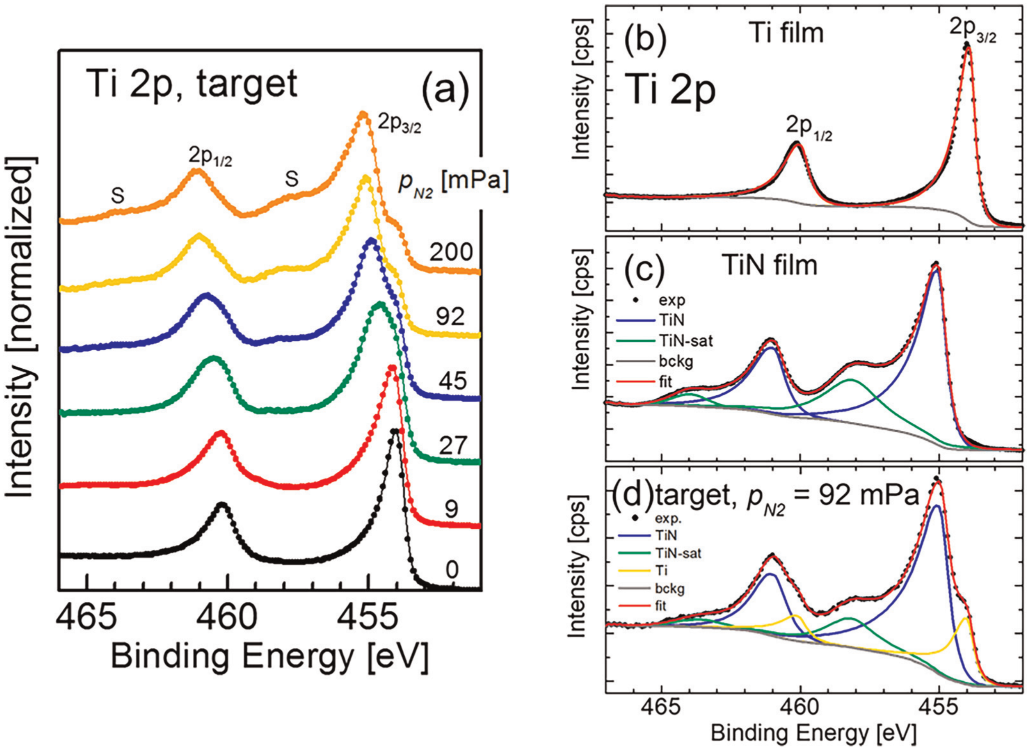

FIG. 31. (a) Set of Ti 2p spectra recorded from Al-capped Ti targets sputtered in Ar/N_2 mixture with the N_2 partial pressure p_{N2} varying from 0 to 200 mPa, (b) reference Ti 2p spectra obtained from Al-capped metallic Ti film, (c) reference Ti 2p spectra obtained from Al-capped metallic TiN film, and (d) Ti 2p spectra from Al-capped target sputtered with $p_{N2} = 92$ mPa. The satisfactory fit in the latter case is obtained using input from peak models created for reference Ti and TiN films. [Reproduced with permission from Greczynski *et al.*, Appl. Phys. Lett. **111**, 021604 (2017). Copyright 2017 AIP Publishing LLC.]

- Perform analyses on fresh samples and minimize the air exposure time. Appreciate that XPS is a surface-sensitive technique (Secs. II F and IV E);
- Evaluate the effects of Ar^+ sputter etching before making conclusions about the bonding structure. Take the time to test different Ar^+ energy and/or incidence angle to see the effects on core-level spectra (Sec. III C);
- Analyze sample series rather than single samples. Consistent trends in data recorded from several samples often lead to more convincing bonding assignments than single spectral features observed for a given sample (Secs. IV A and VI C 5);
- Use reference samples with simpler composition. Core-level spectra are easier to fit and interpret (Sec. IV D);
- Make sure that the instrument has been recently calibrated using ISO standards (Sec. V A);
- Never neglect charge correction. Even well-conducting samples can be mounted in a bad way resulting in a poor electrical contact to the spectrometer and uncontrolled peak shifts (Sec. V B);
- Avoid referencing to the C 1s peak of adventitious carbon (AdC). AdC layers are not a chemically defined compound, do not make proper electrical contact to the sample, and their energy levels are steered by the sample work function. BE of the C 1s peak can vary by as much as 2.6 eV between experiments (Sec. V B);
- Consider signal-to-noise (S/N) ratio before setting up data acquisition. Signals with lower S/N values require longer time per step (rather than more sweeps)—this ensures that possible instrument or sample instabilities that may occur over acquisition time affect all core-level signals in a similar way (Sec. V H);
- Reliable peak fitting requires much time and effort. Think what information is required and if that makes the peak fitting necessary. For example, in the case of non-overlapping signals elemental quantification can be done based on the areas under the spectra envelope; hence, only proper background selection is necessary (Sec. VI C);
- While peak fitting is important to be done correctly, nothing enhances reliability of XPS analyses so much as the self-consistency between core-level spectra of all elements present in the sample (Secs. VI C 3 and VI C 4);
- Perform peak fitting in the order of increasing complexity, i.e., start with reference samples, which are usually easier to fit and use the obtained parameters as an input to model spectra from complex materials (Sec. VI C 1);
- If elemental quantification is a priority, make sure that spectra from different elements are recorded in parallel rather than successively (one after another). This minimizes the impact of instrument and sample instabilities on the outcome (Sec. VI D);
- While plotting the spectra make it easy to distinguish the fitted curve from raw data. Readers should be able to judge the fit quality (Sec. VII);
- Celebrate the richness of chemical information offered by XPS.

ACKNOWLEDGMENTS

The authors most gratefully acknowledge the financial support of the Swedish Research Council VR under Grant No. 2018-03957, the Swedish Energy Agency under Project No. 51201-1, the Knut and Alice Wallenberg Foundation Scholar under Grant Nos. KAW2016.0358 and KAW2019.0290, the Carl Tryggers Stiftelse under Contract Nos. CTS 20:150, CTS 15:219, and CTS 14:431, as well as the Swedish Government Strategic Research Area in Materials Science on Functional Materials at Linköping University (Faculty Grant SFO-Mat-LiU No. 2009-00971). G.G. acknowledges mentorship of Professor Emeritus William R. Salaneck.

AUTHOR DECLARATIONS

Conflict of Interest

The authors have no conflicts to disclose.

DATA AVAILABILITY

The data that support the findings of this study are available from the corresponding author upon reasonable request.

APPENDIX A: RECOMMENDED EXPERIMENTAL PROTOCOL

"XPS was used in this study to analyze [state chemical bonding/elemental composition/lateral and depth distribution of elements or compounds]. The spectrometer was [model and manufacturer]. The base pressure during spectra acquisition was better than [give value with the x rays ON] achieved by [details of the pumping system]. Residual gas analysis revealed that the main background gases in the analysis chamber were […]. The excitation source was [anode type, excitation energy, monochromator (yes/no)] operated at [source power]. The angular range of collected photoelectrons was […] and the electron emission angle was […]. The calibration and linearity of the binding energy scale was confirmed by [method]. With the selected scan parameters, the energy resolution was [value for direct compared to other instruments, e.g., FWHM of the Ag $3d_{5/2}$ or Au $4f_{7/2}$ peak, and how it was determined]. The size of the analyzed sample area was […]. Complementary work function measurements were performed by UPS with [state excitation source and energy, and whether [not?] a monochromator was used]. The samples were prepared by [synthesis method] and stored for [time] in [environment details: pressure, temperature, humidity, etc.] prior to loading into the spectrometer. The transfer procedure within the spectrometer includes exposure to [vacuum level, pumping system] for [time] prior to XPS analyses. The sample surface roughness was […], as determined by […], the possible beam damage effects were evaluated by [details of the test]. [Additional details] (if applicable): the charge neutralizer (what type), sputter etching (ion type, energy, incidence angle, size of the etched area, exposure time), and/or the use of capping layers [state which]. Details of the charge referencing method. The recorded spectra include [core levels/valence band, ….] and the total acquisition time was […]. The spectra were acquired [sequentially or in parallel mode]. The fitting was performed using [name of the software package]. Details of the fitting model are [provide information about background and line functions used, applied constraints, etc.]."

© Author(s) 2022

APPENDIX B: COMMON MISTAKES AND REMEDIES

Table I provides a list of common mistakes and remedies.

TABLE I. A list of common mistakes and remedies.

Stage	Mistake	Consequence/solution	Sections to read
Experiment planning	XPS is not the correct technique to answer research question(s)	It is a good idea to understand before starting measurements what XPS is and what it is not	Secs. II A, II F, III A, and IV A
	Samples are not suited for XPS	UHV compatibility? Possible x-ray damage?	Secs. II A, II F, II G, III A, IV A, IV B, and V F
	Time between surface treatment and XPS analysis not the same for samples being compared	Storage results in continuous buildup of adventitious carbon and oxides, which can affect any products resulting from surface treatments	Secs. II F, III B, and IV E
	The effects of Ar^+ ion etch not considered	Is material sensitive to Ar^+ beam? What Ar^+ energy/incidence angle should be used? How large portion of the signal will come from the Ar^+ beam modified layer?	Secs. II F and III C
Sample considerations	Samples are stored for a long time	Surface covered with thick oxide and carbon layers; *in situ* Ar^+ etching is destructive	Secs. II F, III C, IV E, and V E
	Reference samples missing	More difficult to interpret spectra; interpretation unreliable	Secs. II C, IV D, and VI C 1
	Sample history unknown	Important to keep track of what sample has been exposed to. Good communication with sample owner is crucial. Prepare new samples (all synthesis experiment is repeatable, right?!)	Secs. II F and IV E
Spectra acquisition	Incorrect or lack of charge referencing	It is a common misunderstanding that charge correction is only required for insulating samples. It is *always* required as even perfect conducting samples can be poorly mounted so that not enough electrical contact is established to the spectrometer	Secs. II D, II G, IV B, and V B
	Truncated narrow range spectra	Chose start and end point based on the survey scans	Secs. II E, V G, and VI A
	Poor energy resolution	Incorrect pass energy setting	Secs. II A and V D
	Improper selection of the electron emission angle	Probing depth not optimum for the purpose of the experiment	Secs. II F and V E
	Improper energy step	Aim for at least 10 data points over a single peak	Secs. II E and V G
	Poor spectra quality	Signal-to-noise considerations missing	Sec. V H
	Sample stability during measurement not confirmed	High risk of spectra misinterpretation	Secs. II C, III A, III B, IV A, and V F
Spectra Analysis	Neglecting survey scans	Survey spectra give an excellent overview of sample composition; background shape may be the source of information about the element depth distribution	Secs. II A, III B, V G, and VI A
	Attempting peak fitting while there is no need for it	Determine what information is required	Sec. VI C
	Analysis based only on one type of core-level signal	Much better reliability if all major core levels are analyzed and show self-consistent picture	Secs. II B, II C, and VI C 2

© Author(s) 2022

TABLE I. (*Continued.*)

Stage	Mistake	Consequence/solution	Sections to read
	No consistency between fitted core-level spectra	Bonding involving elements A and B should give peaks in core-level spectra from *both* A and B	Secs. II B, II C, VI C 3, and VI C 4
	No consistency between fitted spectra from sample series	Peaks corresponding to the same chemical state should not shift between spectra recorded from different samples	Secs. II B, II C and VI C 5
	Neglecting C 1s and O 1s spectra	C and O are present on majority of surfaces as a contamination; they cannot be simply skipped in analysis	Secs. II F, III C, IV E, and VI C
	Overfitting (too many component peaks)	Peak model needs to make physical sense	Secs. II B, II C, II E, IV D, and VI C 6
	Component peaks have different line shapes and FWHM without any particular reason	Constraints need to be used during fitting. Peaks cannot be allowed to vary freely. Peak model needs to make physical sense	Secs. II A, II B, II C, and VI C 6
	Neglecting spin-splitting	p, d, and f-type core levels show spin-splitting, proper area ratio, and energy separation needs to be used	Secs. II E and VI C 6
	Misinterpretation of spectral features	Mixing up chemical shifts with other spectral features like spin–split peaks, satellites, shake-up, etc.	Secs. II C and II E
	Unrecognized peak overlap	Overlap of secondary (weaker) signals of element A with primary core-level spectra from element B happens relatively often	Sec. II E
	Peak assignments made by blind reference to databases	Databases show large spread in peak positions. In some cases, the spread is so large that any theory can be proved by arbitrary selection of proper BE value	Secs. II C, II D, II G, V A, V B, and VI C
	Surface charging not recognized	Charging may lead to peak shifts and peak splitting (differential charging) that can be mixed up with chemical shifts	Secs. II D, II G, IV B, and V C
	Directly comparing absolute peak intensities	Absolute peak intensities are strongly dependent on instrumental setup, for that reason it is much easier to compare relative intensity change (either between two states of the same sample or two different samples)	
Results presentation	Experimental details missing	Enough information should be provided to repeat analyses in any other lab	Appendix A
	XPS spectra shown together with results from other methods in one figure	XPS spectra need to be large enough to see all details	Sec. VII
	The raw data not shown	Original data always have to be presented to judge their quality and information they contain	Sec. VII
	Impossible to judge fit quality due to poor visualization	The fitted curve missing or not indicated correctly	Secs. VI C and VII
	The fitted curve follows data closely but is not a sum of background and component peaks	The fitted curve should be a sum of a background function and all component peaks	Sec. VI C

© Author(s) 2022

APPENDIX C: SUGGESTED XPS WORKFLOW

Table II shows the suggested XPS workflow.

TABLE II. Suggested XPS workflow.

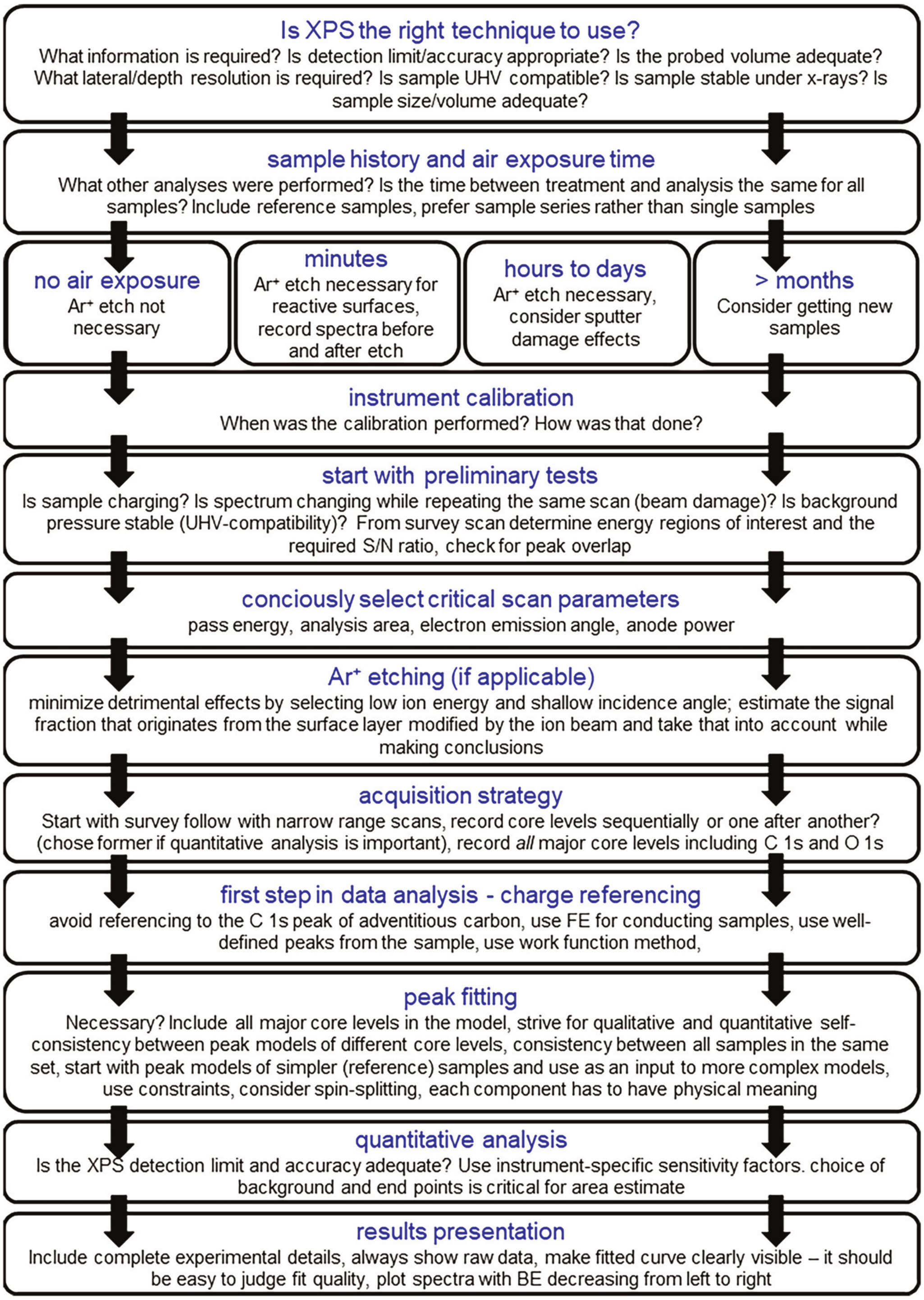

Is XPS the right technique to use?
What information is required? Is detection limit/accuracy appropriate? Is the probed volume adequate? What lateral/depth resolution is required? Is sample UHV compatible? Is sample stable under x-rays? Is sample size/volume adequate?

sample history and air exposure time
What other analyses were performed? Is the time between treatment and analysis the same for all samples? Include reference samples, prefer sample series rather than single samples

no air exposure
Ar^+ etch not necessary

minutes
Ar^+ etch necessary for reactive surfaces, record spectra before and after etch

hours to days
Ar^+ etch necessary, consider sputter damage effects

> months
Consider getting new samples

instrument calibration
When was the calibration performed? How was that done?

start with preliminary tests
Is sample charging? Is spectrum changing while repeating the same scan (beam damage)? Is background pressure stable (UHV-compatibility)? From survey scan determine energy regions of interest and the required S/N ratio, check for peak overlap

conciously select critical scan parameters
pass energy, analysis area, electron emission angle, anode power

Ar^+ etching (if applicable)
minimize detrimental effects by selecting low ion energy and shallow incidence angle; estimate the signal fraction that originates from the surface layer modified by the ion beam and take that into account while making conclusions

acquisition strategy
Start with survey follow with narrow range scans, record core levels sequentially or one after another? (chose former if quantitative analysis is important), record *all* major core levels including C 1s and O 1s

first step in data analysis - charge referencing
avoid referencing to the C 1s peak of adventitious carbon, use FE for conducting samples, use well-defined peaks from the sample, use work function method,

peak fitting
Necessary? Include all major core levels in the model, strive for qualitative and quantitative self-consistency between peak models of different core levels, consistency between all samples in the same set, start with peak models of simpler (reference) samples and use as an input to more complex models, use constraints, consider spin-splitting, each component has to have physical meaning

quantitative analysis
Is the XPS detection limit and accuracy adequate? Use instrument-specific sensitivity factors. choice of background and end points is critical for area estimate

results presentation
Include complete experimental details, always show raw data, make fitted curve clearly visible – it should be easy to judge fit quality, plot spectra with BE decreasing from left to right

© Author(s) 2022

APPENDIX D: GLOSSARY OF BASIC TERMS USED IN XPS

Table III provides a glossary of basic terms used in XPS.

TABLE III. Glossary of basic terms used in XPS.

Term	Abbreviation	Sections	Further reading (reference number)
Acceptance angle	γ	Secs. II A and V E	29
Adventitious carbon	AdC	Secs. II F, III B, IV B, IV E, V B, V H, VI D, and IX, Table I: common mistakes	94, 97, 182, 183, 190
Ag Lα radiation	Ag Lα	Sec. II A	29
Al Kα radiation	Al Kα	Sec. II A	29
Analyzer (see electron energy analyzer)			
Angle-resolved XPS	AR-XPS	Secs. II A and V E	259
Anode		Secs. II A and II E	29
Argon etching		Secs. III C, VIII C, VIII D, and VIII E	65, 96
Asymmetry (of the peak shape)		Secs. II E and VI.C	15, 285
Attenuation length (see effective attenuation length)			
Auger electrons		Sec. II E	260
Auger parameter			261, 262
Background (signal-to-noise)		Sec. V H	55
Background (in fitting)		Sec. VI C	263, 264
Background pressure		Sec. IV A	265
Bake-out		Sec. II F	265
Beam damage		Sec. V F	145
Binding energy	BE or E_B	Secs. II A, II B, II D, and V A	31
Bonding (see chemical bonding)			
Bond strength			266
Bremsstrahlung radiation		Sec. II A	55, 267
Calibration (of binding energy scale)		Secs. II B, II D, and V A	10, 268
Calibration of sputtering rate		Sec. VIII E	
Channel plate detector		Sec. II A	29
Characteristic x-ray radiation		Sec. II A	29
Charging		Secs. II G, IV A, IV C, V B, and V C	161, 168, 177
Charge neutralizer		Secs. II G, IV C, V B, and V C	29, 83
Charge referencing		Secs. II G, IV C, and V B	11, 97
Chemical analysis		Secs. II C, II E, III A, IV D, and VI C	
Chemical bonding		Secs. II C, II E, and III A	269
Chemical composition		Sec. VI D	
Chemical shift		Secs. II B, II C, II E, and V B	31, 34–36, 68, 270–272
Cleaning (see ion sputter etching)			
Cluster ion gun	CIG	Sec. IV E	273
Concentric hemispherical analyzer (see electron energy analyzer)			29
Core electron		Secs. II A and II E	31
Core hole		Secs. II C and II E	40
Core level		Secs. II A and II E	55, 267
Cr Kβ radiation	Cr Kβ		29
Crater (sputter etching)		Sec. VIII E	
Cross section (photoionization)		Secs. II A, V D, V H, and VI D	55, 267
Curve fitting (see peak fitting)			
Damage (see beam damage or sputter damage)			
Deconvolution (see peak fitting)			

© Author(s) 2022

TABLE III. (*Continued.*)

Term	Abbreviation	Sections	Further reading (reference number)
Density of states	DOS	Secs. II E and V B	
Depth profiling (see ion sputter depth profiling)			
Depth resolution (of depth profiles)		Sec. VIII E	274
Detection limit		Secs. III A, V H, and VI D	88
Detector (see channel plate detector)			29
Differential charging		Secs. II G and IV C	80, 81, 82
Diffraction (of photoelectrons)		Sec. VI D	218, 219
Doniach–Sunjic function	D-S	Sec. VI C 1	275
Dual anode		Sec. II A	28, 29
Effective attenuation length	*L*		13, 276, 277
Einstein equation		Sec. II A	55, 267
Elastic electron scattering		Sec. II F	278–280
Electron energy analyzer		Secs. II A and V D	29, 281
Electron emission angle	θ	Secs. II A, III C, V E, VIII A, and VIII B	
Electron escape depth		Sec. II F	12
Electron gun (see charge neutralizer)			
Electron inelastic mean free path	IMFP or λ	Secs. II A, II F, III C, VI D, and VIII A	12
Electronegativity	χ	Secs. II C and II E	269
Electron spectroscopy for chemical analysis	ESCA	Sec. II C	32, 35
Elemental analysis (qualitative, see qualitative analysis)			
Elemental analysis (quantitative, see quantitative analysis)			
Emission angle (see electron emission angle)			
Energy analyzer (see electron energy analyzer			
Energy calibration (see calibration)			
Energy reference levels		Secs. II D, V A and V B	31
Energy resolution		Secs. II A, II E, V D, V H, VI A, and VI B	29
ESCA molecule		Sec. II C	37, 38
Escape depth (see electron escape depth)			
Exchange splitting		Sec. II E	40, 69
Fermi cutoff		Sec. V B	
Fermi edge	FE	Secs. II E and V B	
Fermi level	FL	Secs. II D, II E, and V B	
Film thickness (estimates)	*t*	Secs. VIII A and VIII B	
Final state effects		Secs. II B and II E	40
Fingerprint method		Sec. VI A	55, 267
Fingerprint (influence on the spectra)		Sec. IV B	
fitting (see peak fitting)			
Flood gun (see charge neutralizer)			
Gaussian function	G	Sec. VI C	15, 285
Gaussian–Lorentzian (Voigt) function	G-L	Sec. VI C	15, 285
Ghost peaks		Sec. II E	55, 267
Hemispherical analyzer (see electron energy analyzer)			
High vacuum	HV		265
High energy resolution spectrum		Secs. V D, V G, and VI B	55, 267
Hill equation		Sec. VIII B	197
Imaging XPS		Sec. VIII E	246–248, 282
IMFP (see electron inelastic mean free path)			

© Author(s) 2022

TABLE III. (*Continued.*)

Term	Abbreviation	Sections	Further reading (reference number)
Incidence angle (see ion beam incidence angle)			
Inelastic background		Secs. II A, II E, II F, V H, VI A, and VI D	216, 226
Inelastic mean free path (see electron inelastic mean free path)			
Information depth		Sec. II F	12
Initial state effects		Sec. II E	40
In situ cleaning (see ion sputter etch)			
Instrument calibration (see calibration of binding energy scale)			
Ion beam damage (see sputter damage)			
Ion beam energy	E_{Ar^+}	Sec. III C	
Ion beam incidence angle	α	Sec. III C	
Ion-beam-modified layer thickness	ξ	Sec. III C	
Ion gun		Sec. III C	
Ion sputter etch		Secs. III C, VIII C, and VIII D	
Ion sputter depth profiling		Secs. VIII C and VIII D	233, 283
Ionization cross section (see cross section)			
Kinetic energy (of electrons)	E_{kin}	Sec. II A	
Lateral resolution (in XPS)		Sec. VIII E	247
Lifetime broadening		Sec. II E	56
Linear background		Secs. VI C and VI D	263, 264
Line shape (in fitting)		Sec. VI C	285
Lorentzian function		Sec. VI C	15, 285
Mean free path (see inelastic mean free path)			
Mg Kα radiation		Sec. II A	29
Monochromatic x rays		Secs. II A and II.E	29
Monochromator		Secs. II E and V D	29
Multichannel electron detector (see channel plate detector)			
Multiplet splitting		Sec. II E	40
Narrow-range spectrum		Secs. II E, V D, V G, V H, and VI B	55, 267
Native oxide		Secs. II E, III C, IV E, V B, VIII A, and VIII B	
Native surface		Secs. III C, VI C 1, VIII A, VIII B, and VIII F	
Noise	N	Sec. V H	55
Non-destructive depth profiling		Sec. V E	196
Outgassing		Sec. IV A	265
Overlapping peaks		Sec. VI C	286
Overlayer		Secs. VI A, VIII A, VIII B, and VIII F	
Pass energy	E_{pass}	Secs. II A, V D, V G, V H, VI A, and VI B	55, 267
Peak fitting		Sec. VI C	15, 206, 207, 284–286
Peak overlap (see overlapping peaks)			
Peak-to-background ratio	P/B	Sec. V H	55
Photoelectric effect		Sec. II A	55, 267
Photoionization cross section (see cross section)		Sec. VI D	
Plasmons		Sec. II E	287, 288
Preferential sputtering		Secs. III C, VI C 1, and VI D	209, 210
Probing depth	d	Secs. II A, II F, III C, V E, VI A, VI D, VIII B, VIII C, and VIII E	12
Qualitative analysis		Sec. VI A	55, 267

© Author(s) 2022

TABLE III. (*Continued.*)

Term	Abbreviation	Sections	Further reading (reference number)
Quantification (see quantitative analysis)			
Quantitative analysis		Sec. VI D	16, 17, 289
Radiation damage (see beam damage)			
Referencing (see charge referencing)			
Reference peaks		Secs. II D, V A, and V B	124, 191, 201
Reference samples		Secs. IV D, V B, and VI C 1	124, 191, 201
Reference spectra		Secs. IV D, V B, and VI C 1	124, 191, 201
Relative sensitivity factor	RSF	Sec. VI D	45, 46, 214
Residual gas analyzer	RGA	Sec. IV A	265
Resolution (see energy resolution)			
Sample charging (see charging)			
Sample damage (see beam damage)			
Sample handling		Secs. II F and IV B	9, 290
Sample history		Sec. IV E	
Sample work function	ϕ_{SA}	Secs. II D and V B	184, 185
Sampling depth (see probing depth)			
Satellite peaks (with non-monochromatized x rays)		Secs. II A and II E	55, 267
Screening (of a core hole)		Secs. II C and II E	40
Secondary chemical shifts		Sec. II.C	
Self-consistency (in peak fitting)		Secs. VI C, VI C 3–VI C 5	97, 201
Sensitivity factors (see relative sensitivity factors)			
Shake-off peaks		Sec. II E	68
Shake-up peaks		Sec. II E	68
Shirley background function		Secs. VI C and VI D	263, 264
Signal-to-noise ratio	S/N	Secs. II A, V D, V H, and VI A	198
S/N ratio (see signal-to-noise ratio)			
Spatial imaging (see imaging XPS)			
Spatial resolution (see lateral resolution)			
Specimen (see sample)			
Spectrum		Secs. II A, II C, and II E	55, 267
Spectrometer		Sec. II A	29
Spectrometer work function	ϕ_{SP}	Secs. II D and V B	31
Spectroscopic notation		Sec. II E	55, 267
Spherical mirror analyzer	SMA	Sec. VIII E	251, 252
Spin–orbit (j–j) coupling		Sec. II E	55, 267
Spin–split peaks		Secs. II E, VI C 1, VI C 6, and VIII B	55, 267
Sputter damage		Secs. II A, III C, VIII C, VIII D, and VIII E	95, 96
Sputter depth profiling (see ion sputter depth profiling)			
Sputter etching (see ion sputter etch)			
Substrate		Sec. IV C	
Surface charging (see charging)			
Surface oxide		Secs. IV A, IV E, VIII A, VIII C, and VIII F	
Surface roughness		Secs. II F, III C, IV C, and V E	
Surface sensitivity		Secs. II F, IV B, and IV E	117, 291
Survey spectrum (survey scan)		Secs. V G and VI A	292
Take-off angle	ϕ	Secs. IV C and V E	
Tougaard background function		Secs. VI C and VI D	263, 264
Transmission function (of the instrument)		Sec. VI D	29, 212, 213

© Author(s) 2022

TABLE III. (*Continued.*)

Term	Abbreviation	Sections	Further reading (reference number)
Ultrahigh vacuum	UHV	Sec. II F	265
Ultraviolet photoelectron spectroscopy	UPS	Sec. V B	
Universal curve		Sec. II F	76–78, 117, 293
Vacuum level	VL	Sec. II D	31
Valence band	VB	Sec. II E	294
Valence electrons		Sec. II E	55, 267
Voigt function (see Gaussian–Lorentzian function)			
Wide scan (see survey spectrum)			
Work function (see sample work function)			
Zalar rotation		Secs. VIII D and VIII E	244, 245

REFERENCES

[1] C. J. Powell, "Growth of surface analysis and the development of databases and modeling software for Auger-electron spectroscopy and x-ray photoelectron spectroscopy," Microsc. Today **24**(16), 16–23 (2016).

[2] C. J. Powell, "Improvements in the reliability of x-ray photoelectron spectroscopy for surface analysis," J. Chem. Educ. **81**, 1734 (2004).

[3] Source: Scopus, as of 2021-08-22.

[4] M. R. Linford, V. S. Smentkowski, J. T. Grant, C. R. Brundle, P. M. A. Sherwood, M. C. Biesinger, J. Terry *et al.*, "Proliferation of faulty materials data analysis in the literature," Microsc. Microanal. **26**(1), 1–2 (2020).

[5] G. H. Major, T. G. Avval, B. Moeini, G. Pinto, D. Shah, V. Jain, V. Carver *et al.*, "Assessment of the frequency and nature of erroneous x-ray photoelectron spectroscopy analyses in the scientific literature," J. Vac. Sci. Technol. A **38**(6), 061204 (2020).

[6] M. Baker, "Reproducibility crisis," Nature **533**(353), 452–454 (2016).

[7] D. R. Baer, G. E. McGuire, K. Artyushkova, C. D. Easton, M. H. Engelhard, and A. G. Shard, "Introduction to topical collection: Reproducibility challenges and solutions with a focus on guides to XPS analysis," J. Vac. Sci. Technol. A **39**, 021601 (2021).

[8] D. R. Baer, K. Artyushkova, C. R. Brundle, J. E. Castle, M. H. Engelhard, K. J. Gaskell, J. T. Grant *et al.*, "Practical guides for x-ray photoelectron spectroscopy: First steps in planning, conducting, and reporting XPS measurements," J. Vac. Sci. Technol. A **37**, 031401 (2019).

[9] F. A. Stevie, R. Garcia, J. Shallenberger, J. G. Newman, and C. L. Donley, "Sample handling, preparation and mounting for XPS and other surface analytical techniques," J. Vac. Sci. Technol. A **38**, 063202 (2020).

[10] J. Wolstenholme, "Procedure which allows the performance and calibration of an XPS instrument to be checked rapidly and frequently," J. Vac. Sci. Technol. A **38**, 043206 (2020).

[11] D. R. Baer, K. Artyushkova, H. Cohen, C. D. Easton, M. Engelhard, T. R. Gengenbach, G. Greczynski, P. Mack, D. J. Morgan, and A. Roberts, "XPS guide: Charge neutralization and binding energy referencing for insulating samples," J. Vac. Sci. Technol. A **38**, 031204 (2020).

[12] C. J. Powell, "Practical guide for inelastic mean free paths, effective attenuation lengths, mean escape depths, and information depths in x-ray photoelectron spectroscopy," J. Vac. Sci. Technol. A **38**, 023209 (2020).

[13] S. A. Chambers and Y. Du, "Experimental determination of electron attenuation lengths in complex materials by means of epitaxial film growth: Advantages and challenges," J. Vac. Sci. Technol. A **38**, 043409 (2020).

[14] W. E. S. Unger, J. M. Stockmann, M. Senoner, T. Weimann, S. Bütefisch, C. Passiu, N. D. Spencer, and A. Rossi, "Introduction to lateral resolution and analysis area measurements in XPS," J. Vac. Sci. Technol. A **38**, 053206 (2020).

[15] G. H. Major, N. Fairley, P. M. A. Sherwood, M. R. Linford, J. Terry, V. Fernandez, and K. Artyushkova, "Practical guide for curve fitting in x-ray photoelectron spectroscopy," J. Vac. Sci. Technol. A **38**, 061203 (2020).

[16] A. G. Shard, "Practical guides for x-ray photoelectron spectroscopy: Quantitative XPS," J. Vac. Sci. Technol. A **38**, 041201 (2020).

[17] C. R. Brundle and B. V. Crist, "X-ray photoelectron spectroscopy: A perspective on quantitation accuracy for composition analysis of homogeneous materials," J. Vac. Sci. Technol. A **38**, 041001 (2020).

[18] D. R. Baer, "Guide to making XPS measurements on nanoparticles," J. Vac. Sci. Technol. A **38**, 031201 (2020).

[19] S. A. Chambers, L. Wang, and D. R. Baer, "Introductory guide to the application of XPS to epitaxial films and heterostructures," J. Vac. Sci. Technol. A **38**, 061201 (2020).

[20] P. R. Davies and D. J. Morgan, "Practical guide for x-ray photoelectron spectroscopy: Applications to the study of catalysts," J. Vac. Sci. Technol. A **38**, 033204 (2020).

[21] C. D. Easton, C. Kinnear, S. L. McArthur, and T. R. Gengenbach, "Practical guides for x-ray photoelectron spectroscopy: Analysis of polymers," J. Vac. Sci. Technol. A **38**, 023207 (2020).

[22] H. Hertz, Ann. Phys. **31**, 421–448 (1887).

[23] A. Einstein, "On a heuristic point of view about the creation and conversion of light," Ann. Phys. **17**, 132–148 (1905).

[24] J. J. Yeh and I. Lindau, "Atomic subshell photoionization cross sections and asymmetry parameters: $1 \leq Z \leq 103$," At. Data Nucl. Data Tables **32**, 1–155 (1985).

[25] S. J. B. Reed, *Electron Probe Microanalysis*, 2nd ed. (Cambridge University Press, Cambridge, 1993).

[26] A. W. Potts, in *X-ray Science and Technology*, edited by A. G. Michette and C. J. Buckley (Institute of Physics Publications, Bristol, 1993), p. 48.

[27] K. Siegbahn, D. Hammond, H. Fellner-Feldegg, and E. F. Barnett, "Electron spectroscopy with monochromatized X-rays," Science **176**, 245 (1972).

[28] K. Yates, A. Barrie, and F. J. Street, "A double-anode x-ray source for photoelectron spectroscopy," J. Phys. E: Sci. Instrum. **6**, 130 (1973).

[29] I.W. Drummond, "XPS instrumentation and performance," in *Surface Analysis by Auger and X-Ray Photoelectron Spectroscopy*, edited by D. Briggs and J. T. Grant (IM Publications, Chichester, 2003), pp. 117–144.

[30] H. G. Tompkins, *The Fundamentals of Vacuum Technology*, 2nd ed., AVS Monograph Series M-6 (American Vacuum Society, New York, 1991).

[31] W. F. Egelhoff, Jr., "Core-Level binding-energy shifts at surfaces and in solids," Surf. Sci. Rep. **6**, 253–415 (1987).

© Author(s) 2022

[32] K. Siegbahn and C. Nordling, *ESCA, Atomic, Molecular and Solid State Structure Studied by Means of Electron Spectroscopy* (Almqvist & Wiksells, 1967).

[33] E. Sokolowski, C. Nordling, and K. Siegbahn, "Chemical shift effect in inner electronic levels of Cu due to oxidation," Phys. Rev. **110**, 776 (1958).

[34] S. Hagström, C. Nordling, and K. Siegbahn, "Electron spectroscopic determination of the chemical valence state," Z. Phys. **178**, 439–444 (1964).

[35] S. Hagström, C. Nordling, and K. Siegbahn, "Electron spectroscopy for chemical analyses," Phys. Lett. **9**, 235–236 (1964).

[36] A. Fahlman, K. Hamrin, J. Hedman, R. Nordberg, C. Nordling, and K. Siegbahn, "Electron spectroscopy and chemical binding," Nature **210**, 4–8 (1966).

[37] O. Travnikova, K. J. Børve, M. Patanen, J. Söderström, C. Miron, L. J. Sæthre, N. Mårtensson, and S. Svensson, "The ESCA molecule—Historical remarks and new results," J. Electron Spectrosc. Relat. Phenom. **185**, 191–197 (2012).

[38] U. Gelius, E. Basilier, S. Svensson, T. Bergmark, and K. Siegbahn, "A high resolution ESCA instrument with X-ray monochromator for gases and solids," J. Electron Spectrosc. Relat. Phenom. **2**, 405–434 (1973).

[39] L. Pauling, "The nature of the chemical bond. IV. The energy of single bonds and the relative electronegativity of atoms," J. Am. Chem. Soc. **54**, 3570–3582 (1932).

[40] P. S. Bagus, E. S. Ilton, and C. J. Nelin, "The interpretation of XPS spectra: Insights into materials properties," Surf. Sci. Rep. **68**, 273–304 (2013).

[41] *CRC Handbook of Chemistry and Physics*, 84th ed., edited by D. R. Lide (CRC Press, Boca Raton, FL, 2003); Sec. 9, Molecular Structure and Spectroscopy; Electronegativity.

[42] See "Appendix E polymer C 1s chemical shifts," in *Surface Analysis by Auger and X-Ray Photoelectron Spectroscopy*, edited by D. Briggs and J. T. Grant (IM Publications, Chichester, 2003), pp. 839–842.

[43] See, for example, N. W. Ashcroft and N. D. Mermin, *Solid State Physics* (Saunders College Publishing, 1976).

[44] H. Ishii, K. Sugiyama, E. Ito, and K. Seki, "Energy level alignment and interfacial electronic structures at organic/metal and organic/organic interfaces," Adv. Mater. **11**, 605–625 (1999).

[45] C. D. Wagner, R. Wm, L. E. Davis, J. F. Moulder, and G. E. Muilenberg, *Handbook of X-Ray Photoelectron Spectroscopy* (Perkin-Elmer Corporation, Physical Electronics Division, Eden Prairie, 1979).

[46] N. Ikeo, Y. Iijima, N. Niimura, M. Sigematsu, T. Tazawa, S. Matsumoto, K. Kojima, and Y. Nagasawa, *Handbook of X-Ray Photoelectron Spectroscopy* (JEOL, Tokyo, 1991).

[47] J. F. Moulder, W. F. Stickle, P. E. Sobol, and K. D. Bomben, *Handbook of X-Ray Photoelectron Spectroscopy* (Perkin-Elmer Corporation, Eden Prairie, 1992), p. 261.

[48] B. V. Crist, *Handbook of Monochromatic XPS Spectra: The Elements and Native Oxides* (Wiley, Chichester, 2000), p. 560.

[49] B. V. Crist, *Handbook of Monochromatic XPS Spectra: Semiconductors* (Wiley, Chichester, 2000), p. 568.

[50] See https://https://xpslibrary.com/ for XPS reference spectra (accessed 9 December 2021).

[51] See https://avs.scitation.org/journal/sss for "Surface Science Spectra" (accessed 9 December 2021).

[52] A. J. Barlow, R. T. Jones, A. J. McDonald, and P. J. Pigram, see https://cmsshub.latrobe.edu.au/xpsdatabase for "XPSSurfA: An Open Collaborative XPS Data Repository using the CMSShub Platform" (accessed 9 December 2021).

[53] See http://www.xpsfitting.com/ for examples of peak-fitted XPS spectra (accessed 9 December 2021).

[54] National Institute of Standards and Technology (NIST), X-ray Photoelectron Spectroscopy Database, Version 4.1 compiled by A. V. Naumkin, A. Kraut-Vass, S. W. Gaarenstroom, and C. J. Powell, http://srdata.nist.gov/xps/ (accessed 7 April 2016).

[55] S. Hofmann, *Auger- and X-Ray Photoelectron Spectroscopy in Materials Science*, Springer Series in Surface Science (Springer, 2013), ISSN 0931-5195.

[56] J. C. Fuggle and S. F. Alvarado, "Core-level lifetimes as determined by x-ray photoelectron spectroscopy measurements," Phys. Rev. A **22**, 1615 (1980).

[57] J. C. W. Folmer and D. K. G. De Boer, "XPS core level line shapes in metallic compounds: A probe for the nature of the electrons at the Fermi level," Solid State Commun. **38**, 1135–1138 (1981).

[58] I. Strydom and S. Hofmann, J. Electron Spectrosc. Relat. Phenom. **56**, 85 (1991).

[59] D. Jaeger and J. Patscheider, J. Electron Spectrosc. Relat. Phenom. **185**, 523 (2012).

[60] L. Porte, L. Roux, and J. Hanus, Phys. Rev. B **28**, 3214 (1983).

[61] A. Arranz and C. Palacio, Surf. Sci. **600**, 2510 (2006).

[62] B. W. Veal and A. P. Paulikas, "Final-state screening and chemical shifts in photoelectron spectroscopy," Phys. Rev. B **31**, 5399 (1985).

[63] J. W. Gadzuk and S. Doniach, "A soluble relaxation model for core level spectroscopy on adsorbed atoms," Surf. Sci. **77**, 427–448 (1978).

[64] G. Greczynski, J. Jensen, J. E. Greene, I. Petrov, and L. Hultman, Surf. Sci. Spectra **21**, 35 (2014).

[65] G. Greczynski, D. Primetzhofer, J. Lu, and L. Hultman, "Core-level spectra and binding energies of transition metal nitrides by non-destructive x-ray photoelectron spectroscopy through capping layers," Appl. Surf. Sci. **396**, 347 (2017).

[66] G. Greczynski, I. Petrov, J. E. Greene, and L. Hultman, "Al capping layers for non-destructive x-ray photoelectron spectroscopy analyses of transition-metal nitride thin films," J. Vac. Sci. Technol. A **33**, 05E101 (2015).

[67] R. T. Haasch, T.-Y. Lee, D. Gall, J. E. Greene, and I. Petrov, Surf. Sci. Spectra **7**, 193 (2000).

[68] L. Köver, "Chemical effects in XPS," in *Surface Analysis by Auger and X-Ray Photoelectron Spectroscopy*, edited by D. Briggs and J. T. Grant (IM Publications, Chichester, 2003), pp. 421–464.

[69] V. Kinsinger, I. Sinder, P. Steiner, R. Zimmermann, and S. Hüfner, "Screening and exchange splitting in core level XPS," Solid State Commun. **73**, 527–530 (1990).

[70] ISO 18115-1, *Surface Chemical Analysis—Vocabulary, Part 1—General Terms and Terms Used in Spectroscopy* (International Organization for Standardization, Geneva, 2013).

[71] S. Tanuma, C. J. Powell, and D. R. Penn, "Calculations of electron inelastic mean free paths. IX. Data for 41 elemental solids over the 50 eV to 30 keV range," Surf. Interface Anal. **43**, 689–713 (2011).

[72] H. Shinotsuka, S. Tanuma, C. J. Powell, and D. R. Penn, "Calculations of electron inelastic mean free paths: Data for 41 elemental solids over the 50eV to 200keV range with the relativistic full Penn algorithm," Surf. Interface Anal. **47**, 871 (2015).

[73] H. Shinotsuka, S. Tanuma, C. J. Powell, and D. R. Penn, "Calculations of electron inelastic mean free paths: XII. Data for 42 inorganic compounds over the 50 eV to 200 keV range with the full Penn algorithm," Surf. Interface Anal. **51**, 427 (2019).

[74] S. Tanuma, T. Shiratori, T. Kimura, K. Goto, S. Ichimura, and C. J. Powell, "Experimental determination of electron inelastic mean free paths in 13 elemental solids in the 50 to 5000 eV energy range by elastic-peak electron spectroscopy," Surf. Interface Anal. **37**, 833 (2005).

[75] W. S. M. Werner, C. Tomastik, T. Cabela, G. Richter, and H. Störi, "Elastic electron reflection for determination of the inelastic mean free path of medium energy electrons in 24 elemental solids for energies between 50 and 3400 eV," J. Electron Spectrosc. Relat. Phenom. **113**, 127 (2001).

[76] M. P. Seah and W. A. Dench, "Quantitative electron spectroscopy of surfaces: A standard database for electron inelastic mean free paths in solids," Surf. Interface Anal. **1**, 2–11 (1979).

[77] M. P. Seah, "Simple universal curve for the energy-dependent electron attenuation length for all materials," Surf. Interface Anal. **44**, 1353–1359 (2012).

[78] A. Jablonski and C. J. Powell, "Effective attenuation lengths for different quantitative applications of x-ray photoelectron spectroscopy," J. Phys. Chem. Ref. Data **49**, 033102 (2020).

[79] J. Cazaux, J. Electron Spectrosc. Relat. Phenom. **105**, 155 (1999).

[80] B. J. Tielsch and J. E. Fulghum, "Differential charging in XPS. Part I: Demonstration of lateral charging in a bulk insulator using imaging XPS," Surf. Interface Anal. **24**, 422–427 (1996).

© Author(s) 2022

[81]B. J. Tielsch, J. E. Fulghum, and D. J. Surman, "Differential charging in XPS. Part II: Sample mounting and X-ray flux effects on heterogeneous samples," Surf. Interface Anal. **24**, 459–468 (1996).
[82]B. J. Tielsch and J. E. Fulghum, "Differential charging in XPS. Part III. A comparison of charging in thin polymer overlayers on conducting and non-conducting substrates," Surf. Interface Anal. **25**, 904–912 (1997).
[83]D. R. Baer, M. H. Engelhard, D. J. Gaspar, A. S. Lea, and C. F. Windisch, Jr., "Use and limitations of electron flood gun control of surface potential during XPS: Two non-homogeneous sample types," Surf. Interface Anal. **33**, 781–790 (2002).
[84]NIST, *X-Ray Photoelectron Spectroscopy Database, Version 4.1* (National Institute of Standards and Technology, Gaithersburg, 2012), see http://srdata.nist.gov/xps/ (accessed 2 September 2021).
[85]M. C. Biesinger, *X-Ray Photoelectron Spectroscopy (XPS) Reference Pages* (Surface Science Western, University of Western Ontario, London, Ontario, 2018), see http://www.xpsfitting.com/ (accessed 2 September 2021).
[86]*XPS Simplified: XPS Data Interpretation* (Thermo Fisher Scientific, East Grinstead, 2018), see https://www.thermofisher.com/us/en/home/industrial/spectroscopy-elemental-isotope-analysis/spectroscopy-elemental-isotopeanalysis-learning-center/spectroscopy-elemental-isotope-analysis-resourcelibrary/xps-data-interpretation-webinar.html (accessed 2 September 2021).
[87]B. V. Crist, see https://xpslibrary.com/be-tables/ for a useful set of binding energy tables (accessed 2 September 2021).
[88]A. Shard, "Detection limits in XPS for more than 6000 binary systems using Al and Mg Kα X-rays," Surf. Interface Anal. **46**, 175 (2014).
[89]M. Yoshitake and K. Yoshihara, "Quantitative surface chemical analysis of Au-Cu alloys with XPS," Surf. Interface Anal. **17**, 711–718 (1991).
[90]T. J. M. Ribeiro, F. C. Correia, P. B. Salvador, L. Rebouta, L. C. Alves, E. Alves, N. P. Barradas, A. Mendes, and C. J. Tavares, "Compositional analysis by RBS, XPS and EDX of ZnO:Al,Bi and ZnO:Ga,Bi thin films deposited by d.c.: Magnetron sputtering," Vacuum **161**, 268–275 (2019).
[91]B. Bakhit, D. Primetzhofer, E. Pitthan, M. A. Sortica, E. Ntemou, J. Rosen, L. Hultman, I. Petrov, and G. Greczynski, "Systematic compositional analysis of sputter-deposited boron-containing thin films," J. Vac. Sci. Technol. A **39**, 063408 (2021).
[92]C. J. Powell, D. M. Hercules, and A. W. Czanderna, "Comparisons of SIMS, SNMS, ISS, RBS, AES, and XPS methods for surface compositional analysis," in *Ion Spectroscopies for Surface Analysis* (Springer, Boston, MA, 1991), pp. 417–437.
[93]M. P. Seah, "A review of the analysis of surfaces and thin films by AES and XPS," Vacuum **34**, 463 (1984).
[94]G. Greczynski and L. Hultman, "C 1s peak of adventitious carbon aligns to the vacuum level: Dire consequences for material's bonding assignment by photoelectron spectroscopy," ChemPhysChem **18**, 1507 (2017).
[95]E. Lewin, M. Gorgoi, F. Schäfers, S. Svensson, and U. Jansson, Surf. Coat. Technol. **204**, 455 (2009).
[96]G. Greczynski and L. Hultman, "Towards reliable x-ray photoelectron spectroscopy: Sputter-damage effects in transition metal borides, carbides, nitrides, and oxides," Appl. Surf. Sci. **542**, 148599 (2021).
[97]G. Greczynski and L. Hultman, "X-ray photoelectron spectroscopy: Towards reliable binding energy referencing," Prog. Mater. Sci. **107**, 100591 (2020).
[98]G. Betz, Surf. Sci. **92**, 283 (1980).
[99]M. L. Tarng and G. K. Wehner, J. Appl. Phys. **42**, 2449 (1971).
[100]Y. X. Wang and P. H. Holloway, J. Vac. Sci. Technol. A **2**, 567 (1984).
[101]G. E. Hammer and R. M. Shemenski, J. Vac. Sci. Technol. A **2**, 1132 (1984).
[102]P. Sigmund, J. Vac. Sci. Technol. **17**, 396 (1980).
[103]A. B. Christie, J. Lee, I. Sutherland, and J. M. Walls, Appl. Surf. Sci. **15**, 224 (1983).
[104]G. Greczynski, D. Primetzhofer, and L. Hultman, "Reference binding energies of transition metal carbides by core-level x-ray photoelectron spectroscopy free from Ar+ etching artefacts," Appl. Surf. Sci. **436**, 102 (2018).
[105]R. Shimizu, Nucl. Instrum. Methods Phys. Res., Sect. B **18**, 486 (1987).
[106]H. Y. Wong, C. W. Ong, R. W. M. Kwok, K. W. Wong, S. P. Wong, and W. Y. Cheung, Thin Solid Films **376**, 131 (2000).
[107]R. Reiche, S. Oswald, K. Wetzig, M. Dobler, H. Reuther, and M. Walterfang, Nucl. Instrum. Methods Phys. Res., Sect. B **160**, 397 (2000).
[108]G. Padeletti and G. M. Ingo, Surf. Interface Anal. **34**, 266 (2002).
[109]P. Sigmund and A. Gras-Marti, Nucl. Instrum. Methods **182–183**, 25 (1981).
[110]R. Kelly, I. Bertoti, and A. Miotello, Nucl. Instrum. Methods Phys. Res., Sect. B **80-81**, 1154 (1993).
[111]G. Greczynski, S. Mráz, M. Hans, J. Lu, L. Hultman, and J. M. Schneider, "Control over the phase formation in metastable transition metal nitride thin films by tuning the Al+ subplantation depth," Coatings **9**, 17 (2019).
[112]P. Ziemann, W. Miehle, and A. Plewnia, Nucl. Instrum. Methods Phys. Res., Sect. B **80-81**, 370 (1993).
[113]B.-X. Liu, W. L. Johnson, M. A. Nicolet, and S. S. Lau, Nucl. Instrum. Methods Phys. Res. **209**, 229 (1983).
[114]H. J. Kang, R. H. Roberts, S. He, D. J. O'Connor, and R. J. MacDonald, Surf. Sci. **302**, 363 (1994).
[115]H. J. Kang, C. H. Kim, N. S. Park, D. J. O'Connor, and R. MacDonald, Appl. Surf. Sci. **100-101**, 329 (1996).
[116]S. Tanuma, C. J. Powell, and D. R. Penn, Surf. Interface Anal. **43**, 689 (2011).
[117]C. J. Powell and A. Jablonski, "Surface sensitivity of x-ray photoelectron spectroscopy," Nucl. Instrum. Methods Phys. Res., Sect. A **601**, 54–65 (2009).
[118]J. F. Ziegler, J. P. Biersack, and U. Littmark, *The Stopping and Range of Ions in Solids*, Stopping and Ranges of Ions in Matter Vol. 1 (Pergamon Press, New York, 1984).
[119]E. F. Krimmel and H. Pfleiderer, Radiat. Eff. **19**, 83–85 (1973).
[120]I. Petrov, P. B. Barna, L. Hultman, and J. E. Greene, J. Vac. Sci. Technol. A **21**, 117 (2003).
[121]H. Fager, G. Greczynski, J. Jensen, J. Lu, and L. Hultman, "Growth and properties of amorphous Ti–B–Si–N thin films deposited by hybrid HIPIMS/DC-magnetron co-sputtering from TiB2 and Si targets," Surf. Coat. Technol. **259**, 442 (2014).
[122]R. Shu, E.-M. Paschalidou, S. G. Rao, B. Bakhit, R. Boyd, M. Vinicius Moro, D. Primetzhofer, G. Greczynski, L. Nyholm, A. le Febvrier, and P. Eklund, "Effect of nitrogen content on microstructure and corrosion resistance of sputter-deposited multicomponent (TiNbZrTa)Nx films," Surf. Coat. Technol. **404**, 126485 (2020).
[123]L. Tengdelius, G. Greczynski, M. Chubarov, J. Lu, U. Forsberg, L. Hultman, E. Janzén, and H. Högberg, "Stoichiometric, epitaxial ZrB2 thin films with low oxygen content deposited by magnetron sputtering from a compound target; effects of deposition temperature and sputtering power," J. Cryst. Growth **430**, 55 (2015).
[124]G. Greczynski, S. Mráz, L. Hultman, and J. M. Schneider, "Venting temperature determines surface chemistry of magnetron sputtered TiN films," Appl. Phys. Lett. **108**, 041603 (2016).
[125]N. Hellgren, G. Greczynski, M. A. Sortica, I. Petrov, L. Hultman, and J. Rosen, "X-ray photoelectron spectroscopy analysis of TiB_x ($1.3 \leq x \leq 3.0$) thin films," J. Vac. Sci. Technol. A **39**, 023403 (2021).
[126]L. Landälv, E. Göthelid, J. Jensen, G. Greczynski, J. Lu, M. Ahlgren, L. Hultman, B. Alling, and P. Eklund, "Influence of Si doping on properties of arc deposited (Al,Cr)$2O_3$ coatings," J. Vac. Sci. Technol. A **37**, 061516 (2019).
[127]D. Gall, R. Haasch, N. Finnegan, T.-Y. Lee, C.-S. Shin, E. Sammann, J. E. Greene, and I. Petrov, Surf. Sci. Spectra **7**, 167 (2000).
[128]S. Oswald and R. Reiche, Appl. Surf. Sci. **179**, 307 (2001).
[129]G. Panzner, B. Egert, and H. P. Schmidt, Surf. Sci. **151**, 400 (1985).
[130]R. T. Haasch, T.-Y. Lee, D. Gall, J. E. Greene, and I. Petrov, Surf. Sci. Spectra **7**, 193 (2000).
[131]G. Greczynski and L. Hultman, "*In-situ* observation of self-cleansing phenomena during ultra-high vacuum anneal of transition metal nitride thin films: Prospects for non-destructive photoelectron spectroscopy," Appl. Phys. Lett. **109**, 211602 (2016).
[132]M. A. Baker, S. J. Greaves, E. Wendler, and V. Fox, Thin Solid Films **377–378**, 473 (2000).
[133]E. Lewin, J. Counsell, and J. Patscheider, Appl. Surf. Sci. **442**, 487 (2018).

© Author(s) 2022

[134] I. Yamada, J. Matsuo, N. Toyoda, and A. Kirkpatrick, Mater. Sci. Eng., R **34**, 231 (2001).
[135] T. Miyayama, N. Sanada, M. Suzuki, J. S. Hammond, S.-Q. D. Si, and A. Takahara, J. Vac. Sci. Technol. A **28**, L1 (2010).
[136] A. Theodosiou, B. F. Spencer, J. Counsell, and A. N. Jones, Appl. Surf. Sci. **508**, 144764 (2020).
[137] E. F. Smith, J. Counsell, J. Bailey, J. S. Sharp, M. R. Alexander, A. G. Shard, and D. J. Scurr, Surf. Interface Anal. **49**, 953 (2017).
[138] J. D. P. Counsell, A. J. Roberts, W. Boxford, C. Moffitt, and K. Takahashi, J. Surf. Anal. **20**, 211 (2014).
[139] R. Steinberger, J. Sicking, J. Weise, J. Duchoslav, T. Greunz, D. C. Meyer, and D. Stifter, Appl. Surf. Sci. **403**, 15 (2017).
[140] A. J. Barlow, J. F. Portoles, and P. J. Cumpson, J. Appl. Phys. **116**, 054908 (2014).
[141] M. Engelhard, D. Baer, and S. Lea, "Beam damage of poly (vinyl chloride) [PVC] as observed by x-ray photoelectron spectroscopy at 143 K, 303 K, and 373 K," Surf. Sci. Spectra **10**, 101–116 (2003).
[142] N. M. D. Brown, J. A. Hewitt, and B. J. Meenan, "X-ray-induced beam damage observed during x-ray photoelectron spectroscopy (XPS) studies of palladium electrode ink materials," Surf. Interface Anal. **18**, 187 (1992).
[143] S. Ptasińska, A. Stypczyńska, T. Nixon, N. J. Mason, D. V. Klyachko, and L. Sanche, "X-ray induced damage in DNA monitored by X-ray photoelectron spectroscopy," J. Chem. Phys. **129**, 08B604 (2008).
[144] E. Paparazzo, "XPS studies of damage induced by x-ray irradiation on CeO_2 surfaces," Surf. Sci. **234**, L253–L258 (1990).
[145] D. Baer, D. J. Gaspar, M. H. Engelhard, and A. S. Lea, "Beam effects during AES and XPS analysis," in *Surface Analysis by Auger and X-Ray Photoelectron Spectroscopy*, edited by D. Briggs and J. T. Grant (IM Publications, Chichester, 2003), pp. 211–234.
[146] T. Conard, A. Vanleenhove, and P. van der Heide, "Achieving reproducible data: Examples from surface analysis in semiconductor technology," J. Vac. Sci. Technol. A **38**, 033206 (2020).
[147] G. Greczynski, S. Mráz, L. Hultman, and J. M. Schneider, "Unintentional carbide formation evidenced during high-vacuum magnetron sputtering of transition metal nitride thin films," Appl. Surf. Sci. **385**, 356 (2016).
[148] ISO 15472:2010, *Surface Chemical Analysis—X-Ray Photoelectron Spectrometers—Calibration of Energy Scales* (ISO, Geneva, 2010).
[149] M. P. Seah, "Instrument calibration for AES and XPS," in *Surface Analysis by Auger and X-Ray Photoelectron Spectroscopy*, edited by D. Briggs and J. T. Grant (IM Publications, Chichester, 2003), pp. 167–189.
[150] F. A. Stevie, R. Garcia, J. Shallenberger, J. G. Newman, and C. L. Donley, J. Vac. Sci. Technol. A **38**, 063202 (2020).
[151] G. Schön, J. Electron Spectrosc. **1**, 377 (1973).
[152] K. Asami, J. Nectron Spectrosc. **9**, 469 (1976).
[153] K. Richter and B. Peplinski, J. Electron Spectrosc. **13**, 69 (1978).
[154] R. J. Bird and P. Swift, J. Electron Spectrosc. **21**, 227 (1980).
[155] M. T. Anthony and M. P. Seah, Surf. Interface Anal. **6**, 95 (1984).
[156] T. L. Barr and S. Seal, "Nature of the use of adventitious carbon as a binding energy standard," J. Vac. Sci. Technol. A **13**, 1239–1246 (1995).
[157] ASTM E1523-15, *Standard Guide to Charge Control and Charge Referencing Techniques in X-Ray Photoelectron Spectroscopy* (ASTM International, West Conshohocken, PA, 2015), see www.astm.org.
[158] ISO 19318:2004, *Surface Chemical Analysis—Reporting of Methods Used for Charge Control and Charge Correction*.
[159] D. J. Hnatowich, J. Hudis, M. L. Perlman, and R. C. Ragaini, "Determination of charging effect in photoelectron spectroscopy of nonconducting solids," J. Appl. Phys. **42**, 4883–4886 (1971).
[160] H. Windawi, "Definitive XPS binding energies for heterogeneous materials," J. Electron Spectrosc. Relat. Phenom. **22**, 373–377 (1981).
[161] M. F. Ebel and H. Ebel, "About the charging effect in x-ray photoelectron spectrometry," J. Electron Spectrosc. Relat. Phenom. **3**, 169–180 (1974).
[162] P. Ascarelli and G. Missoni, "Secondary electron emission and the detection of the vacuum level in ESCA," J. Electron Spectrosc. Relat. Phenom. **5**, 417–435 (1974).
[163] R. T. Lewis and M. A. Kelly, "Binding-energy reference in x-ray photoelectron spectroscopy of insulators," J. Electron Spectrosc. Relat. Phenom. **20**, 105–115 (1980).
[164] P. H. Citrin and D. R. Hamann, "Measurement and calculation of polarization and potential-energy effects on core-electron binding energies in solids: X-ray photoemission of rare gases implanted in noble metals," Phys. Rev. B **10**, 4948 (1974).
[165] I. Bertoti, "Characterization of nitride coatings by XPS," Surf. Coat. Technol. **151**, 194–203 (2002).
[166] C. J. Vesely and D. W. Langer, "Electronic core levels of the II B−VI A compounds," Phys. Rev. B **4**, 451 (1971).
[167] D. T. Clark, H. R. Thomas, A. Dilks, and D. Shuttleworth, "A method to reduce the hydrocarbon contamination of samples in x-ray photoelectron spectroscopy," J. Electron Spectrosc. Relat. Phenom. **10**, 455–460 (1977).
[168] D. T. Clark, A. Dilks, and H. R. Thomas, "ESCA applied to polymers. XXI. Investigation of sample-charging phenomena," J. Polym. Sci., Part A: Polym. Chem. **16**, 1461–1474 (1978).
[169] D. A. Stephenson and N. J. Binkowski, "X-ray photoelectron spectroscopy of silica in theory and experiment," J. Non-Cryst. Solids **22**, 399–421 (1976).
[170] M. J. Edgell, D. R. Baer, and J. E. Castle, "Biased referencing experiments for the XPS analysis of non-conducting materials," Appl. Surf. Sci. **26**, 129–149 (1986).
[171] C. D. Wagner, "Chemical shifts of Auger lines, and the Auger parameter," Faraday Discuss. Chem. Soc. **60**, 291–300 (1975).
[172] C. D. Wagner, "Auger parameter in electron spectroscopy for the identification of chemical species," Anal. Chem. **47**, 1201–1203 (1975).
[173] C. D. Wagner, H. A. Six, W. T. Jansen, and J. A. Taylor, "Improving the accuracy of determination of line energies by ESCA: Chemical state plots for silicon-aluminum compounds," Appl. Surf. Sci. **9**, 203 (1981).
[174] C. D. Wagner, L. H. Gale, and R. H. Raymond, "Two-dimensional chemical state plots: A standardized data set for use in identifying chemical states by x-ray photoelectron spectroscopy," Anal. Chem. **51**, 466–482 (1979).
[175] B. V. Crist, *Handbooks of Monochromatic XPS Spectra—The Elements and Native Oxides* (XPS International LLC, Mountain View, CA, 1999), Vol. 1.
[176] P. Swift, "Adventitious carbon—The panacea for energy referencing?," Surf. Interface Anal. **4**, 47–51 (1982).
[177] D. J. Hnatowich, J. Hudis, M. L. Perlman, and R. C. Ragaini, "Determination of charging effect in photoelectron spectroscopy of nonconducting solids," J. Appl. Phys. **42**, 4883–4886 (1971).
[178] G. Johansson, J. Hedman, A. Berndtsson, M. Klasson, and R. Nilsson, J. Electron Spectrosc. Relat. Phenom. **2**, 295–317 (1973).
[179] R. Nordberg, H. Brecht, R. G. Albridge, A. Fahlman, and J. R. Van Wazer, "Binding energy of the '2p' electrons of silicon in various compounds," Inorg. Chem. **9**, 2469–2474 (1970).
[180] S. Kinoshita, T. Ohta, and H. Kuroda, "Comments on the energy calibration in X-ray photoelectron spectroscopy," Bull. Chem. Soc. Jpn. **49**, 1149–1150 (1976).
[181] W. P. Dianis and J. E. Lester, "External standards in x-ray photoelectron spectroscopy. Comparison of gold, carbon, and molybdenum trioxide," Anal. Chem. **45**, 1416–1420 (1973).
[182] G. Greczynski and L. Hultman, "Compromising science by ignorant instrument calibration—Need to revisit half a century of published XPS data," Angew. Chem., Int. Ed. **59**, 5002 (2020).
[183] G. Greczynski and L. Hultman, "Reliable determination of chemical state in x-ray photoelectron spectroscopy based on sample-work-function referencing to adventitious carbon: Resolving the myth of apparent constant binding energy of the C 1s peak," Appl. Surf. Sci. **451**, 99 (2018).
[184] S. Evans, "Work function measurements by X-Pe spectroscopy, and their relevance to the calibration of X-Pe spectra," Chem. Phys. Lett. **23**, 134–138 (1973).
[185] M. G. Helander, M. T. Greiner, Z. B. Wang, and Z. H. Lu, "Pitfalls in measuring work function using photoelectron spectroscopy," Appl. Surf. Sci. **256**, 2602–2605 (2010).
[186] K. Sugiyama, H. Ishii, Y. Ouchi, and K. Seki, J. Appl. Phys. **87**, 295 (2000).
[187] W. Li and D. Y. Li, J. Chem. Phys. **122**, 064708 (2005).

© Author(s) 2022

[188] M. Xue, H. Wu, J. Ou, F. Wang, X. Li, W. Li, and Z. Jiang, J. Appl. Phys. **111**, 123714 (2012).
[189] G. N. Derry, M. E. Kern, and E. H. Worth, J. Vac. Sci. Technol. A **33**, 060801 (2015).
[190] G. Greczynski and L. Hultman, "The same chemical state of carbon gives rise to two peaks in x-ray photoelectron spectroscopy," Sci. Rep. **11**, 11195 (2021).
[191] J. Mendialdua, R. Casanova, and Y. Barbaux, "XPS studies of V_2O5, V_6O_{13}, VO_2 and V_2O_3," J. Electron Spectrosc. Relat. Phenom. **71**, 249 (1995).
[192] D. A. Huchital and R. T. McKeon, Appl. Phys. Lett. **20**, 158 (1977).
[193] S. Mähl, M. Neumann, S. Dieckhoff, V. Schlett, and A. Baalmann, J. Electron Spectrosc. Relat. Phenom. **85**, 197 (1997).
[194] D. F. Mitchell, K. B. Clark, J. A. Bardwell, W. N. Lennard, G. R. Massoumi, and I. V. Mitchell, "Film thickness measurements of SiO_2 by XPS," Surf. Interface Anal. **21**, 44–50 (1994).
[195] H. Iwai, J. S. Hammond, and S. Tanuma, "Recent status of thin film analyses by XPS," J. Surf. Anal. **15**, 264–270 (2009).
[196] M. Pijolat and G. Hollinger, "New depth-profiling method by angular-dependent x-ray photoelectron spectroscopy," Surf. Sci. **105**, 114–128 (1981).
[197] J. M. Hill, D. G. Royce, C. S. Fadley, L. F. Wagner, and F. J. Grunthaner, Chem. Phys. Lett. **44**, 225 (1976).
[198] M. F. Koenig and J. T. Grant, Surf. Interface Anal. **7**, 217 (1985).
[199] S. Tougaard, "Accuracy of the non-destructive surface nanostructure quantification technique based on analysis of the XPS or AES peak shape," Surf. Interface Anal. **26**, 249–269 (1998).
[200] D. R. Baer and A. G. Shard, "Role of consistent terminology in XPS reproducibility," J. Vac. Sci. Technol. A **38**, 031203 (2020).
[201] G. Greczynski and L. Hultman, "Self-consistent modeling of x-ray photoelectron spectra from air-exposed polycrystalline TiN thin films," Appl. Surf. Sci. **387**, 294 (2016); some details of fitting models were modified in the present tutorial taking into account the recent developments in the charge referencing techniques (cf. Refs. 97, 182, and 183), as well as, in order to make the treatment more pedagogically correct.
[202] S. Doniach and M. Sunjic, J. Phys. C: Solid State Phys. **3**, 285–291 (1970).
[203] L. Porte, L. Roux, and J. Hanus, "Vacancy effects in the x-ray photoelectron spectra of TiN_x," Phys. Rev. B **28**, 3214 (1983).
[204] A. Arranz and C. Palacio, "Screening effects in the Ti 2p core level spectra of Ti-based ternary nitrides," Surf. Sci. **600**, 2510 (2006).
[205] P. Merel, M. Tabbal, M. Chaker, S. Moisa, and J. Margot, "Direct evaluation of the sp3 content in diamond-like-carbon films by XPS," Appl. Surf. Sci. **136**, 105–110 (1998).
[206] P. M. A. Sherwood, "The use and misuse of curve fitting in the analysis of core x-ray photoelectron spectroscopic data," Surf. Interface Anal. **51**, 589–610 (2019).
[207] B. Singh, A. Diwan, V. Jain, A. Herrera-Gomez, J. Terry, and M. R. Linford, "Uniqueness plots: A simple graphical tool for identifying poor peak fits in x-ray photoelectron spectroscopy," Appl. Surf. Sci. **387**, 155–162 (2016).
[208] B. Moeini, H. Haack, N. Fairley, V. Fernandez, T. R. Gengenbach, C. D. Easton, and M. R. Linford, "Box plots: A simple graphical tool for visualizing overfitting in peak fitting as demonstrated with x-ray photoelectron spectroscopy data," J. Electron Spectrosc. Relat. Phenom. **250**, 147094 (2021).
[209] S. Berg and I. V. Katardjiev, "Preferential sputtering effects in thin film processing," J. Vac. Sci. Technol. A **17**, 1916–1925 (1999).
[210] R. Shimizu, "Preferential sputtering," Nucl. Instrum. Methods Phys. Res., Sect. B **18**, 486–495 (1986).
[211] W. Palmberg, "Quantitative Auger electron spectroscopy using elemental sensitivity factors," J. Vac. Sci. Technol. **13**, 214 (1975).
[212] M. P. Seah, "Data compilations: Their use to improve measurement certainty in surface analysis by AES and XPS," Surf. Interface Anal. **9**, 85 (1986).
[213] B. Hu, L. Yu, G. Wang, S. Hutton, H. Huang, and Z. Du, "Exploration of transmission efficiency and quantitative measurement of the axis ultra electron spectrometer," Measurement **43**, 1299–1304 (2010).
[214] C. D. Wagner, L. E. Davis, M. V. Zeller, J. A. Taylor, R. H. Raymond, and L. H. Gale, "Empirical atomic sensitivity factors for quantitative analysis by electron spectroscopy for chemical analysis," Surf. Interface Anal. **3**, 211–225 (1981).
[215] S. Tougaard, "Formalism for quantitative surface analysis by electron spectroscopy," J. Vac. Sci. Technol. A **8**, 2197–2203 (1990).
[216] S. Tougaard, "Inelastic background correction and quantitative surface analysis," J. Electron Spectrosc. Relat. Phenom. **52**, 243–271 (1990).
[217] S. Tougaard, "Surface nanostructure determination by x-ray photoemission spectroscopy peak shape analysis," J. Vac. Sci. Technol. A **14**, 1415–1423 (1996).
[218] C. S. Fadley, M. A. Van Hove, Z. Hussain, and A. P. Kaduwela, "Photoelectron diffraction: New dimensions in space, time, and spin," J. Electron Spectrosc. Relat. Phenom. **75**, 273–297 (1995).
[219] J. Osterwalder, "Structural effects in XPS and AES: Diffraction," in *Surface Analysis by Auger and X-Ray Photoelectron Spectroscopy*, edited by D. Briggs and J. T. Grant (IM Publications, Chichester, 2003), pp. 557–586.
[220] J. E. Castle, H. Chapman-Kpodo, A. Proctor, and A. M. Salvi, "Curve-fitting in XPS using extrinsic and intrinsic background structure," J. Electron Spectrosc. Relat. Phenom. **106**, 65–80 (2000).
[221] M. Jo, "Direct, simultaneous determination of XPS background and inelastic differential cross-section using Tougaard's algorithm," Surf. Sci. **320**, 191–200 (1994).
[222] M. P. Seah, "Background subtraction: I. General behaviour of tougaard-style backgrounds in AES and XPS," Surf. Sci. **420**, 285–294 (1999).
[223] J. Végh, "The Shirley background revised," J. Electron Spectrosc. Relat. Phenom. **151**, 159–164 (2006).
[224] See, for example, M. P. Seah, "Quantification in AES and XPS," in *Surface Analysis by Auger and X-Ray Photoelectron Spectroscopy*, edited by D. Briggs and J. T. Grant (IM Publications, Chichester, 2003), pp. 345–376, or S. Tougaard, "Quantification of nano-structures by electron spectroscopy," in *Surface Analysis by Auger and X-Ray Photoelectron Spectroscopy*, edited by D. Briggs and J. T. Grant (IM Publications, Chichester, 2003), pp. 295–344.
[225] D. A. Shirley, "High-resolution x-ray photoemission spectrum of the valence bands of gold," Phys. Rev. B **5**, 4709 (1972).
[226] S. Tougaard, "Quantitative analysis of the inelastic background in surface electron spectroscopy," Surf. Interface Anal. **11**, 453–472 (1988).
[227] S. Tougaard, "Practical algorithm for background subtraction," Surf. Sci. **216**, 343–360 (1989).
[228] ISO 13424:2013, *SCA-XPS—Reporting of Results of Thin-Film Analysis.*
[229] ISO 19830:2015, *SCA-XPS—Minimum Reporting Requirements for Peak Fitting in X-ray Photoelectron Spectroscopy.*
[230] ISO 15470:2017, *SCA-XPS—Description of Selected Instrumental Performance Parameters.*
[231] B. R. Strohmeier, "An ESCA method for determining the oxide thickness on aluminum alloys," Surf. Interface Anal. **15**, 51–56 (1990).
[232] T. A. Carlson, "Basic assumptions and recent developments in quantitative XPS," Surf. Interface Anal. **4**, 125–134 (1982).
[233] S. Hofmann, "Sputter depth profiling: Past, present, and future," Surf. Interface Anal. **46**, 654–662 (2014).
[234] G. Greczynski, L. Hultman, and M. Odén, "X-ray photoelectron spectroscopy studies of $Ti_{1-x}Al_xN$ ($0 \le x \le 0.83$) high-temperature oxidation: The crucial role of Al concentration," Surf. Coat. Technol. **374**, 923 (2019).
[235] G. Greczynski, B. Bakhit, L. Hultman, and M. Odén, "High Si content TiSiN films with superior oxidation resistance," Surf. Coat. Technol. **398**, 126087 (2020).
[236] G. Greczynski, I. Petrov, J. E. Greene, and L. Hultman, "A paradigm shift in thin-film growth by magnetron sputtering: From gas-ion to metal-ion irradiation of the growing film," J. Vac. Sci. Technol. A **37**, 060801 (2019).
[237] O. Knotek, M. Böhmer, and T. Leyendecker, J. Vac. Sci. Technol. A **4**, 2695 (1986).
[238] T. Leyendecker, O. Lemmer, S. Esser, and J. Ebberink, Surf. Coat. Technol. **48**, 175 (1991).
[239] J. D. P. Counsell, A. J. Roberts, W. Boxford, C. Moffitt, and K. Takahashi, J. Surf. Anal. **20**, 211 (2014).
[240] D. McIntyre, J. E. Greene, G. Håkansson, J.-E.- Sundgren, and W.-D. Műnz, J. Appl. Phys. **67**, 1542 (1990).

© Author(s) 2022

[241] F. Esaka, K. Furuya, H. Shimada, M. Imamura, N. Matsubayashi, H. Sato, A. Nishijima, A. Kawana, H. Ichimura, and T. Kikuchi, J. Vac. Sci. Technol. A **15**, 2521 (1997).
[242] I. Milošev, H.-H. Strehblow, and B. Navinšek, Surf. Coat. Technol. **74-75**, 897 (1995).
[243] H. Fager, B. M. Howe, G. Greczynski, J. Jensen, A. B. Mei, J. Lu, L. Hultman, J. E. Greene, and I. Petrov, "Novel hard, tough HfAlSiN multilayers, defined by alternating Si bond structure, deposited using modulated high-flux, low-energy ion irradiation of the growing film," J. Vac. Sci. Technol. A **33**, 05E103 (2015).
[244] A. Zalar, "Improved depth resolution by sample rotating during Auger electron spectroscopy depth profiling," Thin Solid Films **124**, 223 (1985).
[245] A. Zalar and S. Hofmann, "Comparison of rotational depth profiling with AES and XPS," Appl. Surf. Sci. **68**, 361–367 (1993).
[246] U. Vohrer, C. Blomfield, S. Page, and A. Roberts, "Quantitative XPS imaging—New possibilities with the delay-line detector," Appl. Surf. Sci. **252**, 61–65 (2005).
[247] K. Artyushkova and J. E. Fulghum, "XPS imaging," in *Surface Analysis by Auger and X-Ray Photoelectron Spectroscopy*, edited by D. Briggs and J. T. Grant (IM Publications, Chichester, 2003), pp. 677–732.
[248] D. J. Morgan, "Imaging XPS for industrial applications," J. Electron Spectrosc. Relat. Phenom. **231**, 109 (2019).
[249] See https://www.kratos.com/products/axis-supra-xps-surface-analysis-instrument for detailed specification of modern instrument capabilities (accessed 11 January 2022).
[250] See https://www.phi.com/surface-analysis-equipment/quantera-ii.html for detailed specification of modern instrument capabilities (accessed 11 January 2022).
[251] H. Z. Sar-El, Nucl. Instrum. Methods **42**, 71 (1966).
[252] J. Walton and N. Fairley, "Characterisation of the Kratos axis ultra with spherical mirror analyser for XPS imaging," Surf. Interface Anal. **38**, 1230–1235 (2006).
[253] G. Greczynski, S. Mráz, L. Hultman, and J. M. Schneider, "Native target chemistry during reactive dc magnetron sputtering studied by *ex-situ* x-ray photoelectron spectroscopy," Appl. Phys. Lett. **111**, 021604 (2017).
[254] G. Greczynski, S. Mraz, L. Hultman, and J. M. Schneider, "Substantial difference in target surface chemistry between reactive dc and high power impulse magnetron sputtering," J. Phys. D: Appl. Phys. **51**, 05LT01 (2018).
[255] S. Berg, H.-O. Blom, T. Larsson, and C. Nender, J. Vac. Sci. Technol. A **5**, 202 (1987).
[256] J.-E. Sundgren, B.-O. Johansson, and S.-E. Karlsson, Surf. Sci. **128**, 265 (1983).
[257] W. Möller and W. Eckstein, Nucl. Instrum. Methods Phys. Res., Sect. B **2**, 814 (1984).
[258] W. Möller, W. Eckstein, and J. P. Biersack, Comput. Phys. Commun. **51**, 355 (1988).
[259] P. J. Cumpson, "Angle-resolved X-ray photoelectron spectroscopy," in *Surface Analysis by Auger and X-Ray Photoelectron Spectroscopy*, edited by D. Briggs and J. T. Grant (IM Publications, Chichester, 2003), pp. 651–676.
[260] J. T. Grant, "AES: Basic principles, spectral features and qualitative analysis," in *Surface Analysis by Auger and X-Ray Photoelectron Spectroscopy*, edited by D. Briggs and J. T. Grant (IM Publications, Chichester, 2003), pp. 57–88.
[261] G. Moretti, "Auger parameter and Wagner plot in the characterization of chemical states by x-ray photoelectron spectroscopy: A review," J. Electron Spectrosc. Relat. Phenom. **95**, 95–144 (1998).
[262] C. J. Powell, "Recommended auger parameters for 42 elemental solids," J. Electron Spectrosc. Relat. Phenom. **185**, 1–3 (2012).
[263] S. Tougaard, "Practical guide to the use of backgrounds in quantitative XPS," J. Vac. Sci. Technol. A **39**, 011201 (2021).
[264] M. H. Enhelhard, D. R. Baer, A. Herrera-Gomez, and P. M. A. Sherwood, "Introductory guide to backgrounds in XPS spectra and their impact on determining peak intensities," J. Vac. Sci. Technol. A **38**, 063203 (2020).
[265] See any handbook of vacuum technology, e.g., D. Hoffman, B. Singh, and J. H. Thomas III, *Handbook of Vacuum Science and Technology* (Elsevier, 1997).
[266] Y. R. Luo, *Comprehensive Handbook of Chemical Bond Energies* (CRC Press, Boca Raton, FL, 2007).
[267] D. Briggs, "XPS: Basic principles, spectral features and qualitative analysis," in *Surface Analysis by Auger and X-Ray Photoelectron Spectroscopy*, edited by D. Briggs and J. T. Grant (IM Publications, Chichester, 2003), pp. 31–56.
[268] M. P. Seah, "Instrument calibration for AES and XPS," in *Surface Analysis by Auger and X-Ray Photoelectron Spectroscopy*, edited by D. Briggs and J. T. Grant (IM Publications, Chichester, 2003), pp. 167–190.
[269] L. Pauling, *The Nature of the Chemical Bond* (Cornell University Press, Ithaca, NY, 1960), Vol. 260.
[270] U. Gelius, P. F. Heden, J. Hedman, B. J. Lindberg, R. Manne, R. Nordberg, C. Nordling, and K. Siegbahn, "Molecular spectroscopy by means of ESCA. III. Carbon compounds," Phys. Scr. **2**, 70 (1970).
[271] L. I. Johansson, "Electronic and structural properties of transition-metal carbide and nitride surfaces," Surf. Sci. Rep. **21**, 177–250 (1995).
[272] N. Mårtensson, E. Sokolowski, and S. Svensson, "50 years anniversary of the discovery of the core level chemical shifts: The early years of photoelectron spectroscopy," J. Electron Spectrosc. Relat. Phenom. **193**, 27–33 (2014).
[273] I. Yamada, "Historical milestones and future prospects of cluster ion beam technology," Appl. Surf. Sci. **310**, 77–88 (2014).
[274] P. J. Cumpson, "Angle-resolved XPS and AES: Depth-resolution limits and a general comparison of properties of depth-profile reconstruction methods," J. Electron Spectrosc. Relat. Phenom. **73**, 25–52 (1995).
[275] S. Doniach and M. Sunjic, "Many-electron singularity in X-ray photoemission and x-ray line spectra from metals," J. Phys. C: Solid State Phys. **3**, 285 (1970).
[276] W. S. M. Werner, "Electron transport in solids," in *Surface Analysis by Auger and X-Ray Photoelectron Spectroscopy*, edited by D. Briggs and J. T. Grant (IM Publications, Chichester, 2003), pp. 235–258.
[277] S. Tanuma, "Electron attenuation lengths," in *Surface Analysis by Auger and X-Ray Photoelectron Spectroscopy*, edited by D. Briggs and J. T. Grant (IM Publications, Chichester, 2003), pp. 259–294.
[278] A. Jablonski, "Elastic scattering and quantification in AES and XPS," Surf Interface Anal. **14**, 659–685 (1989).
[279] H. Ebel, M. F. Ebel, J. Wernisch, and A. Jablonski, "Quantitative XPS analysis considering elastic scattering," Surf Interface Anal. **6**, 140–143 (1984).
[280] S. Tougaard and A. Jablonski, "Quantitative XPS: Influence of elastic electron scattering in quantification by peak shape analysis," Surf Interface Anal. **25**, 404–408 (1997).
[281] D. Roy and D. Tremblay, "Design of electron spectrometers," Rep. Prog. Phys. **53**, 1621 (1990).
[282] I. W. Drummond, F. J. Street, L. P. Ogden, and D. J. Surman, "Axis: An imaging x-ray photoelectron spectrometer," Scanning **13**, 149 (1991).
[283] T. Wagner, J. Y. Wang, and S. Hofmann, "Sputter depth profiling in AES and XPS," in *Surface Analysis by Auger and X-Ray Photoelectron Spectroscopy*, edited by D. Briggs and J. T. Grant (IM Publications, Chichester, 2003), pp. 619–650.
[284] A. Herrera-Gomez, "Uncertainties in photoemission peak fitting accounting for the covariance with background parameters," J. Vac. Sci. Technol. A **38**, 033211 (2020).
[285] N. Fairley, "XPS lineshapes and curve fitting," in *Surface Analysis by Auger and X-Ray Photoelectron Spectroscopy*, edited by D. Briggs and J. T. Grant (IM Publications, Chichester, 2003), pp. 397–420.
[286] N. Fairley, V. Fernandez, M. Richard-Plouet, C. Guillot-Deudon, J. Walton, E. Smith, D. Flahaut *et al.*, "Systematic and collaborative approach to problem solving using x-ray photoelectron spectroscopy," Appl. Surf. Sci. Adv. **5**, 100112 (2021).
[287] P. Steiner, H. Höchst, and S. Hüfner, "Analysis of the plasmon structure in XPS experiments of simple metals," Phys. Lett. A **61**, 410–412 (1977).
[288] T. Fujikawa, "Theory of intrinsic and extrinsic plasmon excitation in deep core XPS spectra," J. Phys. Soc. Jpn. **55**, 3244–3257 (1986).
[289] M. P. Seah, "Quantification in AES and XPS," in *Surface Analysis by Auger and X-Ray Photoelectron Spectroscopy*, edited by D. Briggs and J. T. Grant (IM Publications, Chichester, 2003), pp. 345–376.

© Author(s) 2022

[290] J. Geller, "Specimen preparation and handling," in *Surface Analysis by Auger and X-Ray Photoelectron Spectroscopy*, edited by D. Briggs and J. T. Grant (IM Publications, Chichester, 2003), pp. 89–116.

[291] C. J. Powell, A. Jablonski, I. S. Tilinin, S. Tanuma, and D. R. Penn, "Surface sensitivity of Auger-electron spectroscopy and x-ray photoelectron spectroscopy," J. Electron Spectrosc. Relat. Phenom. **98**, 1–15 (1999).

[292] D. Shah, D. I. Patel, T. Roychowdhury, G. B. Rayner, N. O'Toole, D. R. Baer, and M. R. Linford, "Tutorial on interpreting x-ray photoelectron spectroscopy survey spectra: Questions and answers on spectra from the atomic layer deposition of Al_2O_3 on silicon," J. Vac. Sci. Technol. B **36**, 062902 (2018).

[293] A. Jablonski, "Photoelectron transport in the surface region of solids: Universal analytical formalism for quantitative applications of electron spectroscopies," J. Phys. D: Appl. Phys. **48**, 075301 (2015).

[294] P. M. A. Sherwood, "Valence bands studied by XPS," in *Surface Analysis by Auger and X-Ray Photoelectron Spectroscopy*, edited by D. Briggs and J. T. Grant (IM Publications, Chichester, 2003), pp. 531–556.

© Author(s) 2022